The Pennsylvania State University

The Graduate School

College of Engineering

MODELING AND EXPERIMENTAL TESTING OF A HYBRID IMPULSIVE-PNEUMATIC DE-ICING SYSTEM

A Thesis in

Aerospace Engineering

by

Carter M. Forry

Submitted in Partial Fulfillment

of the Requirements

for the Degree of

Master of Science

May 2019

The thesis of Carter M. Forry was reviewed and approved* by the following:

Jose L. Palacios

Assistant Professor of Aerospace Engineering

Thesis Advisor

Edward C. Smith

Professor of Aerospace Engineering

Ahmad Haidar

Leonardo Helicopters Structural Dynamics Engineer

Amy Pritchett

Professor of Aerospace Engineering

Department Head of Aerospace Engineering

*Signatures are on file in the Graduate School.

Abstract

This thesis designed and fabricated a scaled hybrid impulsive-pneumatic aircraft de-icing system. This system deformed a 0.01-in thick stainless steel leading edge shell producing transverse shear stresses capable of delaminating accreted ice. The system used pneumatic and impulsive aspects which together reduce the pressure required to delaminate accreted ice. Like a traditional pneumatic de-icing system, pressure is applied which deforms the shell around the leading edge. The impulsive aspect of the system constrains and releases two portions of the deformable shell, adding beneficial inertia effects. The impulsive sections of the deformable shell are constrained using electromagnets that can be precisely controlled using a microcontroller. The electromagnets can release the two portions of the shell in a symmetric or asymmetric fashion. A symmetric inflation releases the constraints on both sides of the airfoil at the same time while an asymmetric inflation releases one constraint and then the other after a controllable period. The hybrid de-icing system was tested at The Pennsylvania State University's Adverse Environment Research Test Systems Icing Tunnel. The de-icing system, which uses static and impulsive aspects, was able to delaminate ice with a leading edge thickness in the range 0.11-in to 0.32-in with as little as 2.5 psi using the dynamic asymmetric

inflation technique. The static inflation technique, which is widely used on small aircraft, alone was unable to delaminate the accreted ice for any leading edge ice thickness.

A finite element analysis model was used to assist in the design of the physical hybrid impulsive-pneumatic de-icing system. Aspects of the physical hybrid de-icing system such as that electromagnet placement and propagation times are determined by the FEA model. The FEA model was inherently dynamic which was a new technique that was not implemented in previous literature. The ice/shell bonding interaction was simulated in Abaqus using cohesive zone methods. The model is mesh dependent due to the cohesive zone method used; therefore, interaction properties from separate experiments are used to characterize the cohesive behavior. A bench top flat plate experiment was conducted to experimentally determine a cohesive surface modulus for the 410 stainless steel. The flat plate device used the same stainless steel as the scaled hybrid system. Freezer ice was bonded to the flat plate and the pressure required to completely delaminate a range of ice thicknesses was recorded. Using the pressure values from the flat plate bench-top experiments, the FEA model's cohesive surface modulus was corrected to yield the same delamination results. With the correct stainless steel cohesive surface modulus, the flat plate and FEA model required pressures differ on average by 23% for symmetric inflation and 20% for asymmetric inflation. Stress-strain laws were shown to be consistent between the FEA model and the flat plate bench-top experiment by comparing the deflection at the center of the plate. At a pressure less than 2 psi, the maximum percent difference between the model and experimental plate deflection was approximately 2%. The FEA model was used to compare

impulsive shell inflation techniques: static, symmetric, and asymmetric. The performance of each technique was quantified by tracking the nodal separation of the ice and shell and the greatest nodal separation yielded the greatest de-icing potential. For the asymmetric inflation case, the FEA model was used to determine the time between shell constraints being released which result in the greatest nodal separation.

The same cohesive behavior used in the flat plate FEA model was then implemented onto a NACA 0024 airfoil section. This FEA model was then used to predict ice delamination for the airfoil de-icing system icing tunnel tests. The FEA model was corrected to account for asymmetric drag during icing tunnel testing. Using the asymmetric drag correction, the percent difference between the FEA model and experimental results was approximately 18% for ice which did not fracture after pressure was applied.

Table of Contents

List of Figures

List of Tables

List of Symbols

AOA	Absolute angle of attack
$\mathbf{C_d}$	Drag Coefficient
$\mathbf{C_l}$	Lift Coefficient
d	Fiber Diameter
D	Droplet Diameter
D	Drag
E	Elasticity Modulus
$\mathbf{F}$	Body Force
G	Fracture Energy
I	Internal Force Vector
K_P	Penalty Stiffness
l_e	Mesh Element Size
LWC	Liquid Water Content
MVD	Median Volume Diameter
M	Mass Matrix
M_{tip}	Mass of Blade Tip

N	Mode III Inter-Laminar Shear Strength
P	Pressure
P	External Force Vector
R	Blade Radius
S	Mode II Inter-Laminar Shear Strength
T	Mode I Inter-Laminar Tensile Strength
T	Temperature
t	Test Duration
$\mathbf{u}$	Displacement Matrix
α	Power Law Coefficient
α	Angle of Attack
β	Mixed-Mode Ratio
δ	Cohesive Layer separation
ν	Viscosity Coefficient
Ω	Rotational Speed
ρ	Density
σ	Normal Traction
τ_{xy}	Shear Traction
θ	Contact Angle
ζ	Structural Damping Coefficient

Acknowledgments

I would like to sincerely thank my long-time adviser and mentor, Dr. Jose Palacios, for his time, guidance and support during my time as both an undergraduate and graduate student. I started working with Dr. Palacios during my sophomore year through the CERI program. As a result of Dr. Palacios' mentorship over the years, I owe a lot my academic success to him. This project experienced some challenges along the way, but Dr. Palacios was always there to offer guidance. I would also like to thank Dr. Haidar, Dr. Pritchett, and Dr. Smith for taking the time to review my thesis.

I am thankful for the assistance and support from my colleagues in the Adverse Environment Research Test Systems Lab and the Penn State Vertical Lift Research Center of Excellence. In addition to my colleagues, I'd like to thank Dr. Joe Szefi for his guidance in the construction of the experimental models. I would also like to thank the Penn State College of Engineering for financial support during my graduate studies through the College of Engineering University Graduate Fellowship. In addition to the College of Engineering, I also thank the Aerospace Department for financial and academic support over the past five years. Finally, I would like to thank my family and friends for their encouragement and unwavering support over

the years.

This material is based upon partial funding provided by the Air Force under the SBIR sub grant 201040 from Invercon LLC. Any opinions, findings, and conclusions or recommendations expressed in this publication are those of the author and do not necessarily reflect the views of the Air Force. The authors would like to thank the Air Force team for the funding. The U.S. Government is authorized to reproduce and distribute reprints notwithstanding any copyright notation thereon. The views and conclusions contained in this document are those of the authors and should not be interpreted as representing the official policies, either expressed or implied, of the U.S. Government.

Chapter 1

Introduction

1.1 Research Motivation

The harmful effects caused by icing environments on aircraft have been a constant problem for nearly a century. The implications of aircraft icing can be costly not only in a monetary sense, but also in the potential loss of life. To mitigate the harmful effects of aircraft icing, many disciplines of engineers and scientists have been conducting research to understand the physical phenomenon of icing [1–22].

Icing conditions can have multifarious adverse effects on an aircraft. The most worrisome effect is when the control of an aircraft is reduced or even completely lost. In certain icing conditions, ice can accrete to control surfaces where protective systems typically are not utilized resulting in a loss of control. In these dire situations the pilot, or an autonomous flight computer, may not be able to safely maneuver the aircraft, which could become catastrophic. A tragic example is American Eagle Flight 4184 where ice formed on aft control surfaces where de-icing systems were not employed [23]. The pilot was unable to regain control of the

aircraft which unfortunately resulted in the death of all 68 on board. Other than loss of aircraft control, the performance can deteriorate from a buildup of ice. Work conducted by Han et al. (Ref [24]) shown below in Figure 1.1 illustrates how the lift coefficient (C_l) and stall angle of attack (AOA) change when ice has accreted versus a clean airfoil.

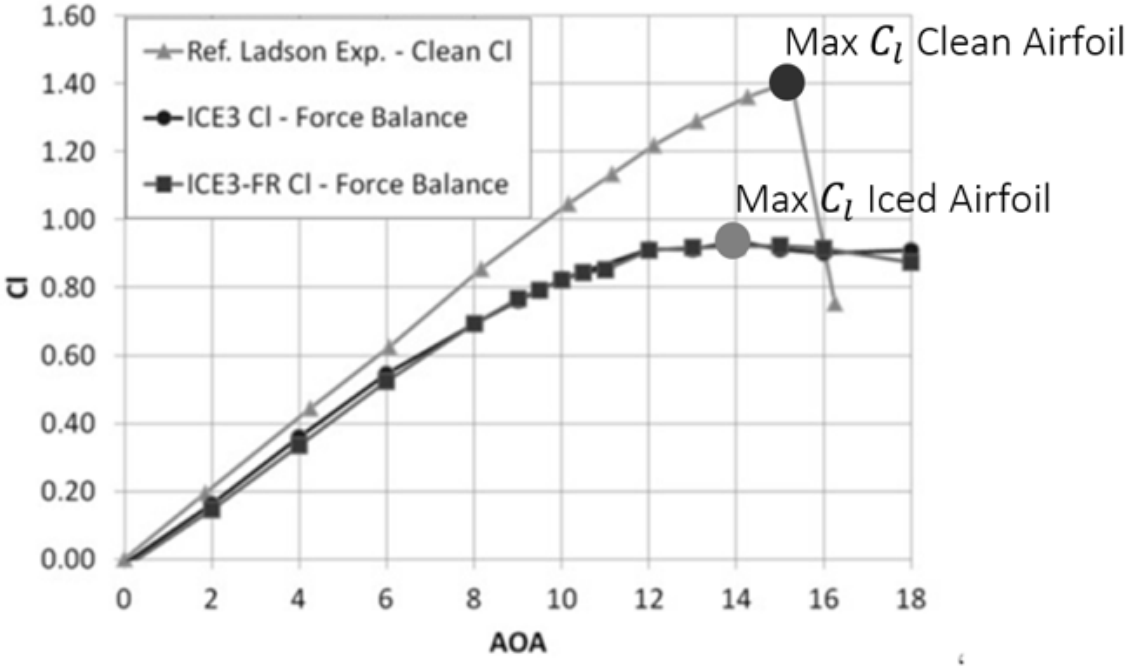

Figure 1.1: Lift Coefficient versus AOA [24]

On an iced airfoil, the lift coefficient is constantly less compared to a clean airfoil, particularly the maximum lift coefficient. The stall angle of attack can also be seen to reduce under icing conditions. Testing conducted by Ref. [25] also aimed to demonstrate how icing adversely affects the performance of an airfoil. Particularly, the way in which the drag coefficient (C_d) of an iced airfoil is dramatically greater than a clean airfoil (Figure 1.2).

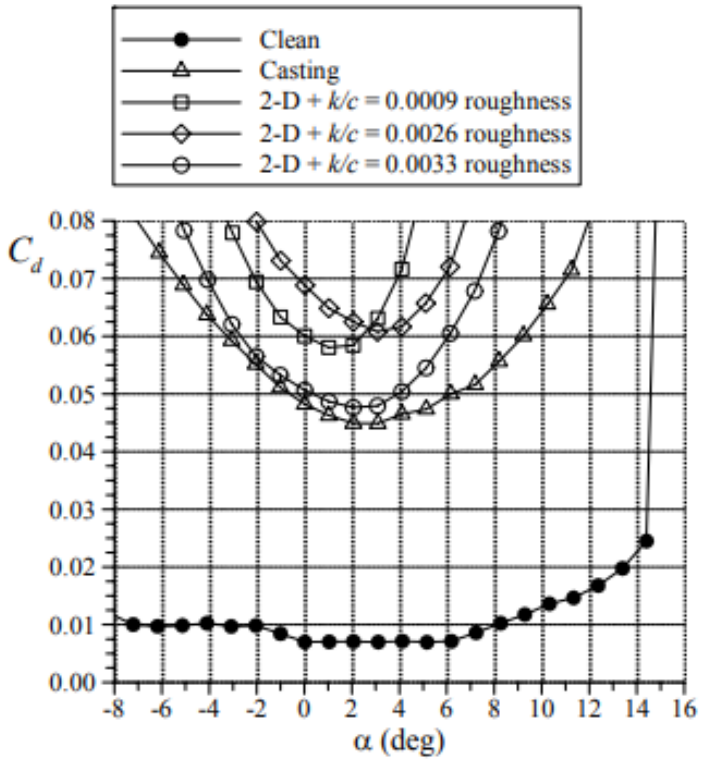

Figure 1.2: Drag versus Angle of Attack for a NACA 23012 [25]

Results shown in Figure 1.2 conclude that when the airfoil is iced, represented by surface roughness, the drag coefficient is at least five times as great compared to the clean airfoil reducing the performance of an aircraft. The general effects that result from aircraft icing, all of which can be hazardous, are summarized in Figure 1.3.

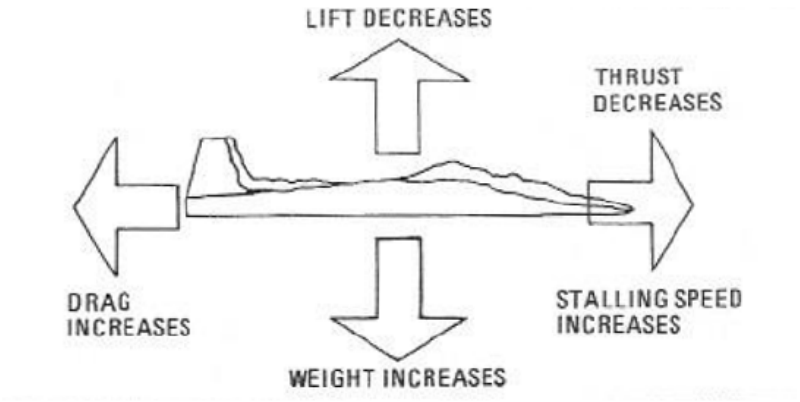

Figure 1.3: General Effects of Icing on an Aircraft [26]

Even for an experienced pilot or a sophisticated autonomous flight computer, the effects of icing could make the aircraft irrecoverable. This is dangerous for both the passengers of the aircraft and for the people on the ground who might reside in the path of an uncontrollable aircraft. Due to the described potential hazards of aircraft icing, the United States Federal Aviation Administration (FAA) has issued federal guidelines regarding aircraft icing in the Code of Federal Regulations (CFR) including the use of de-icing systems [27]. For a commercial aircraft to be certified for flight, it must be able to safely fly in the icing conditions outlined in the CFR Title 14 [27]. No aircraft, commercial airliners, unmanned aircraft system (UAS), or rotorcraft are completely safe from the complications resulting from icing. Due to the potential issues that aircraft icing presents, mitigation mechanisms are usually introduced. Therefore, there is a necessity to understand the capability of these systems to diminish harmful effects of icing.

Due to the described harmful effects, ice protective systems, or de-icing systems, are implemented on aircraft. One such system is a pneumatic de-icing system. Modern pneumatic systems use a metal shell, for durability reasons, and inflate

using a simple static technique. When this shell deforms transverse shear stresses are generated. Inflating in a static technique without the added benefits of centrifugal forces, these metal shell systems require pressures of over 20 psi to delaminate ice using just transverse shear stresses [2, 11]. Currently, both physical pneumatic de-icing systems and FEA modeling efforts have only used static inflation techniques to generate the necessary transverse shear stresses leading to large amounts of required pressure. Only using static inflation techniques negates the beneficial de-icing effects of the ice and shell inertia. Therefore, this research explores impulsive-dynamic effects in both the FEA modeling and physical system design to enhance the de-icing capability.

1.2 Thesis Objectives

The primary objective of this research is to develop a hybrid impulsive-pneumatic aircraft de-icing system with the assistance of an FEA model. Both the physical system and FEA model will implement impulsive-dynamic aspects. A successful system design will reduce the pressure required to delaminate accreted ice compared to a traditional pneumatic de-icing system. This principal objective is achieved by meeting the following goals:

1. Develop a flat plate model in Abaqus FEA which simulates the cohesive bonding properties of ice using the known interaction properties.
2. Fabricate a bench-top flat plate experiment to verify Abaqus stress-strain relationships. Quantify the pressure required for the flat plate to completely delaminate freezer ice of varying thicknesses.

3. Experimentally determine the cohesive surface modulus for the stainless steel leading edge shell material using the bench-top flat plate system for use in the airfoil FEA model.

4. Develop an airfoil Abaqus FEA model, representative of the hybrid impulsive-pneumatic de-icing system, to assist in the design and to predict accreated ice delamination. Such aspects of the FEA model used to assist in the design of physcial system include optimal inflation techniques and release times for the asymmetric inflation case.

5. Fabricate the scaled hybrid impulsive-pneumatic de-icing system based on results from the FEA model to include the location of the electromagnets and propagation times. Quantify the pressure required for the airfoil hybrid de-icing system to completely delaminate accreted ice for varying testing conditions.

1.3 Icing Overview

Aircraft icing can occur when the ambient temperature is less than the freezing temperature of water, 0°C. At these subfreezing temperatures, since water in a cloud is generally pure, the water droplets exist in a super-cooled state since there is no point of initial crystallization [28]. When the suspended super-cooled water droplets in the atmosphere impact an aircraft, the droplets freeze resulting in ice. An object has what is called a collection efficiency, which describes the percentage of droplets that impact the object. The collection efficiency is influenced by both the speed of the aircraft and geometric properties, which can be used in tandem with Liquid Water Content (LWC) and Mean Volumetric Diameter (MVD) to

determine the rate of droplets impacting a surface [29, 30]. The LWC is analogous to the density of water in a cloud, typically measured in g/m^3. The MVD is the median size of the droplets based on the distributed volumes of a sample of droplets. The MVD of an icing cloud tends to be measured in μm.

The freezing of the water droplets to a surface is dictated by heat transfer. There is an energy balance between the latent heat released by the freezing droplet and the convection cooling due to air flowing over the surface [29, 30]. The balance of these energies results in what is known as freezing fraction which is what percentage of the droplet freezes on impact. Four characteristics drive the value of the freezing fraction: ambient temperature, LWC, MVD, and the speed that the surface is moving [31].

There are two distinct types of icing regimes, rime and glazed. The glazed icing condition occurs at warmer temperatures, higher MVD, and higher LWC. Rime icing conditions occur at colder temperatures, lower MVD, and lower LWC [32]. There is no defined transition point between rime and glaze conditions, but rather a mixed regime. Icing conditions that are close to the border of the two conditions can have characteristics of both rime and glazed ice. The differences between rime and glazed ice shapes along with a mixed icing condition are illustrated in Figure 1.4.

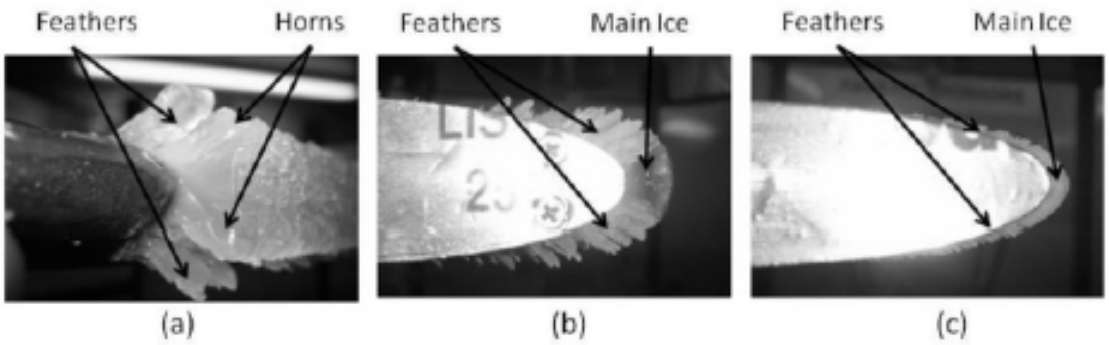

Figure 1.4: Glazed (a), Mixed (b), and Rime (c) [33]

There are obvious visual differences between rime and glazed ice. Rime ice is opaque and white while glazed ice is clear. Rime ice shapes tend to be more streamlined but rough while glazed shapes are smoother but do not follow the shape of the surface [31, 33]. The differences in the shape come from how the water droplets freeze on impact. The differences in how ice freezes under glazed and rime icing conditions is shown in Figure 1.5.

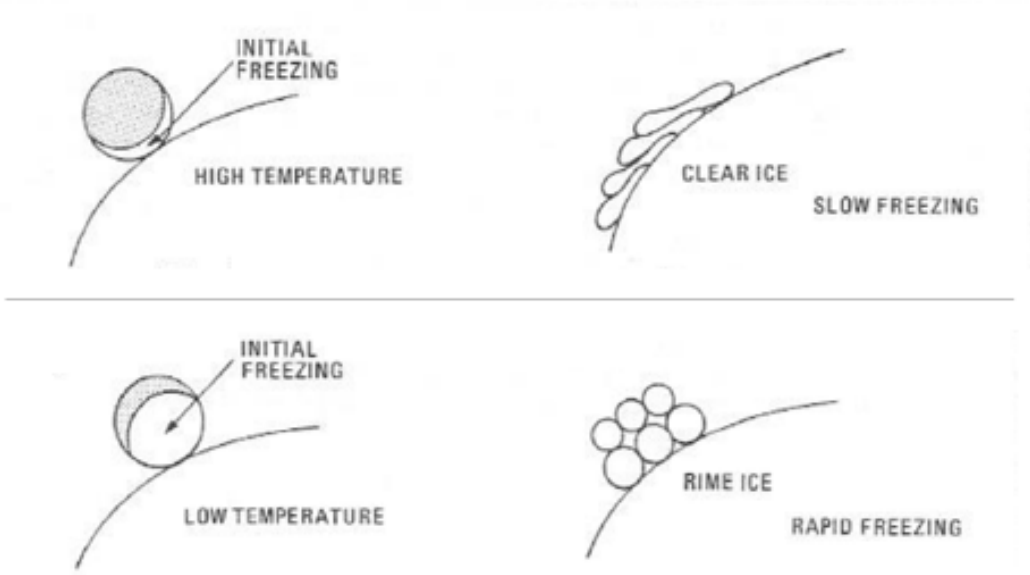

Figure 1.5: Glaze Freezing Process (top), Rime Freezing Process (bottom) [26]

At glazed icing conditions, the top two portions of Figure 1.5, only a small fraction of the droplet initially freezes while the rest of the droplet is free to run back the surface. Under rime icing conditions, the bottom portion of Figure 1.5, a large fraction of the droplet initially freezes; therefore, less of the droplet is free to run back on the object's surface. Since in rime conditions the water freezes rapidly, air is caught in-between particles of ice yielding the rough texture and opaque color. Under glazed conditions, since the water droplets do not freeze as fast, less air is trapped leading to a more transparent color.

1.4 Ice Protective Systems Overview

Ever since aircraft icing became an area of concern, there have been several attempts to develop effective Ice Protective Systems (IPS). The following IPS are relevant in the ongoing attempt to prevent harmful effects of accreted ice. In some instances, several of these IPS will be used in tandem to improve the overall effectiveness. This is done to try and utilize the best aspects of each system and achieve more coverage of the aircraft.

1.4.1 Electrothermal

Electrothermal IPS use heat to melt the ice interface. The heat is created by electrical current flowing through resistive elements. The resistive elements convert electrical potential energy to thermal energy. The resistive elements are typically placed under an outer skin so that they are protected from environmental factors. Therefore, the thermal energy is conducted through an outer skin to the ice-skin

interface. Once this interface has decreased by a sufficient amount, aerodynamic forces carry the ice away in the direction of the airflow [1, 13, 22].

Both anti-icing and de-icing protection methods can be achieved using electrothermal heaters. The anti-icing method uses continuously heated areas on a wing to evaporate the water droplets. The downside to anti-icing is that it requires much more power than a de-icing system; therefore, de-icing is a more energy conservative method [13, 22]. De-icing allows a tolerable thickness of ice to accrete to the outer surface before powering on the resistive elements. De-icing therefore aims to melt the interface and not evaporate the water droplets on impact.

Typically, the anti-icing and de-icing methods are used together. A parting strip, which is a thin heating element that runs along the leading edge, is supplied power continuously (anti-icing). This parting strip does not allow any ice to build up on the leading edge. On the upper and lower surfaces of the wing there are de-icing electrothermal elements. Both the parting strip and the de-icing elements are usually covered by a skin or at least a coating [1, 22] to avoid erosion. A schematic of the described electrothermal system is shown below in Figure 1.6.

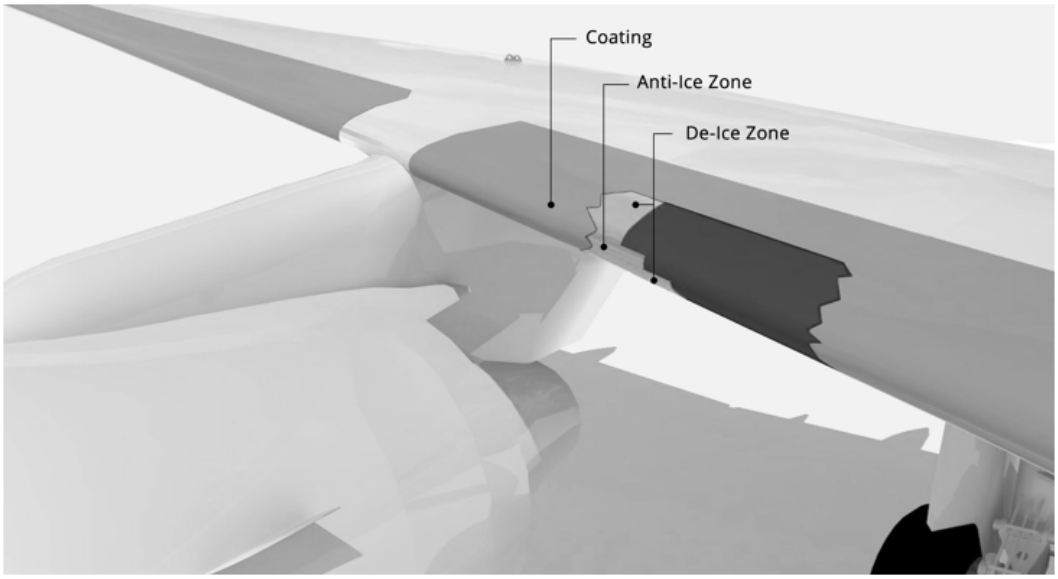

Figure 1.6: Electrothermal Ice Protection System [22]

One drawback of the above electrothermal system is that runback can occur. When the ice interface is melted, liquid water can run aft and refreeze elsewhere on the wing. Specifically, the water could run back and refreeze on control surfaces inhibiting the pilot to maneuver the aircraft.

Despite being relatively effective, electrothermal systems require a significant amount of power. According to Ref. [13], for an anti-icing evaporation system in compliance with AIR1168/4, the parting strip could require up to 31 kW/m^2 and the surrounding heaters require 34 kW/m^2. Some aircraft may not have large reservoirs of excess power to employ a full electrothermal system based on the quoted power required.

Although the concept of electrothermal IPS is relatively simple, there have been recent advancements. One example came in 2004 when Goodrich developed an electrothermal system, the Low Power Electrothermal De-icing System (LPED). The major difference between the LPED system and a conventional electrothermal

system is that the LPED uses a large amount of power over a small time using capacitors. Operating in small time intervals allows the LPED system to operate between 20% to 50% less power than a conventional electrothermal system [14]. To cover 128 in. of wing during a flight test, the LPED system required 1928 W at 28 VDC and -20°C.

Recently, there have been advancements in improving the resistive heating element used in electrothermal systems by using Carbon Nanotubes (CNT) arrays. The CNT arrays are fabricated using a modified chemical vapor deposition process. In this deposition process, the CNT are effectively grown to lengths of 80 µm to 100 µm on silicon wafers 46 mm in width and a length between 25 mm and 150 mm. The CNT arrays are then knocked down and compressed onto the Silicon wafer using guaranteed nonporous Teflon (GNPT) [1]. This process is illustrated below in Figure 1.7.

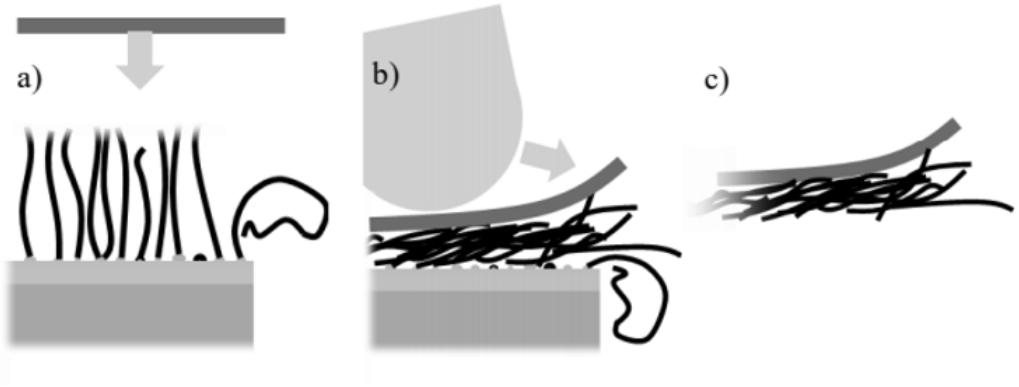

Figure 1.7: CNT Array Construction [1]

In Figure 1.7, (a) shows that the GNPT is brought to the CNT. (b) shows a small radius tool compressing the CNT to the Silicon wafer, and (c) shows the end result. Icing tunnel tests were performed at temperatures ranging from -20.9°C to -3.9°C, airspeed of 55.9 m/s, LWC of 1.1 g/m^3 , and a MVD of 30 μm. The peak

power required was approximately 8 kW/m^2 , but the average power required was approximately 1 kW/m^2 [1]. Therefore, CNT arrays can produce more heat given the same amount of energy compared to traditional heaters. In the early stage of development, CNT arrays have promising results in terms of power required to de-ice. Currently, the production of CNT on a large scale is difficult, and is an ongoing area of research. If an efficient method is developed to manufacture CNT arrays on an industrial scale, they could be a viable option for use in electrothermal de-icing systems.

1.4.2 Pneumatic

Pneumatic de-icing systems mechanically remove accreted ice from a surface versus heat like electrothermal systems. The conventional design has inflatable boots along the wing which are made of a flexible material, usually a neoprene material. When pressure is applied to the boots, they inflate creating transverse shear stresses along the ice-boot interface. Once the transverse shear stresses overcome the adhesion strength of the ice, the ice debonds from the surface and is carried away by the airflow [4, 6]. The process of boot inflation and ice debonding is demonstrated below in Figure 1.8.

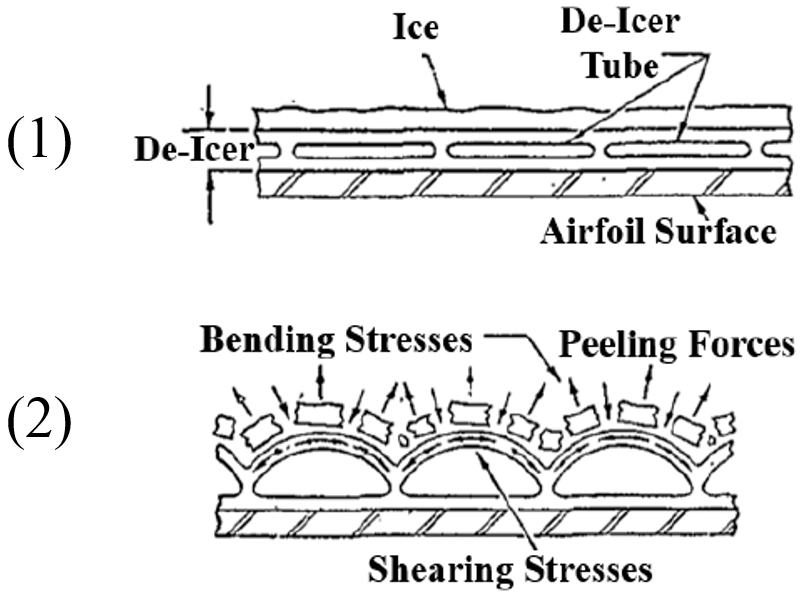

Figure 1.8: Operation of a Pneumatic De-icing System [4]

The top portion of Figure 1.8 (1) illustrates the pneumatic de-icing system deflated with a layer of accreted ice. The bottom portion of Figure 1.8 (2) shows the boots inflating creating transverse shear stresses which debond the ice.

One advantage of this system over electrothermal systems is that since the ice interface is not being melted, there is no runback. Another advantage over electrothermal systems is that generally, pneumatic systems require less power to operate. A common twin-engine business airplane with a pneumatic de-icing system weighs approximately 50 lb and requires 1 HP to operate [15]. One disadvantage of pneumatic de-icing systems is that the system only operates properly over a given range of ice thicknesses. If the ice is too thick, the inflated boots may not be able to create large enough transverse shear stresses to debond the ice. If the ice is too thin, the ice may not completely debond from the surface, and this will form somewhat of a flexible ice layer that additional ice can accrete to allowing more ice

to build up. Due to these issues, a sensor that measures the ice thickness is usually used with a pneumatic de-icing system to attempt to signal the pilot to use the IPS. Another issue is that pneumatic boots are not very durable when made of rubber like materials, so every few years the boots must be relapsed [4].

The first recorded development of a pneumatic de-icing system was in 1930 by B.F. Goodrich in collaboration with Cornell University's icing wind tunnel. This system, named the "Ice-Removing Overshoe," consists of a rubber tube reinforced by elastic stockinet fabric which would expand when subjected to pressure from a pump [10]. A schematic of this early IPS is illustrated below in Figure 1.9.

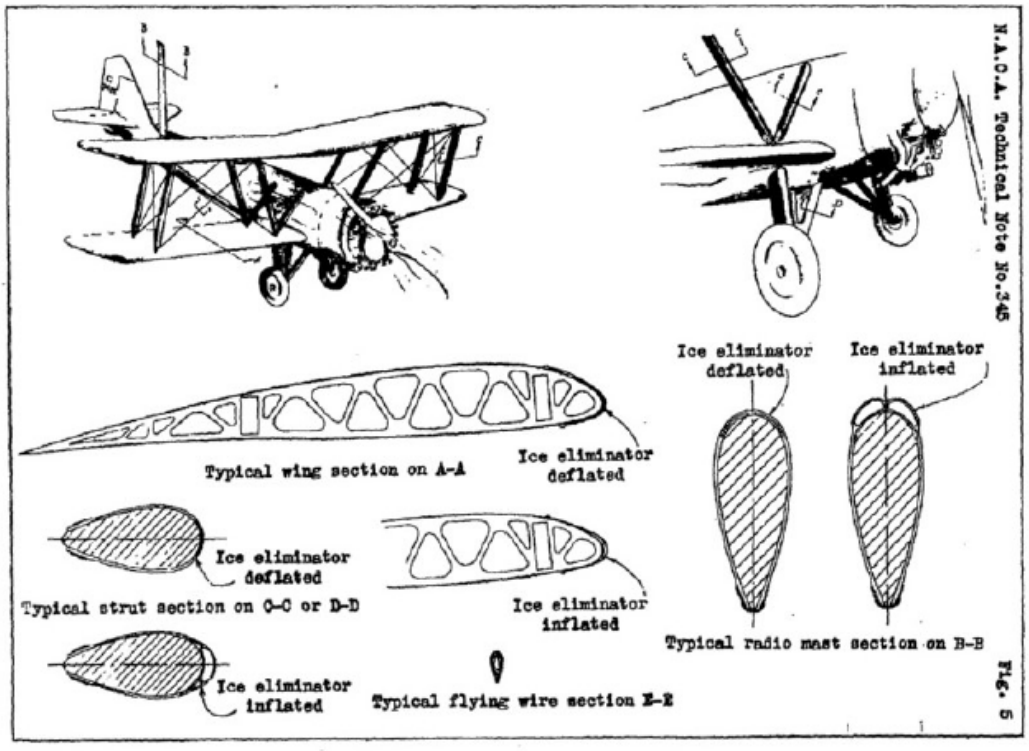

Figure 1.9: First Pneumatic De-icing System designed by B.F. Goodrich [6]

B.F. Goodrich further improved upon their original design in 1984 with the Pneumatic Impulse Ice Protection (PIIP) system. The PIIP system uses rapid

inflation and deflation to "launch" the ice off the wing. The inflation could occur in as little 50 μs. A downside of the PIIP system is it requires very large pressures, approximately 400 to 1500 psig depending on the coverage area of the wing. A schematic of the PIIP system developed by Goodrich is shown below in Figure 1.10.

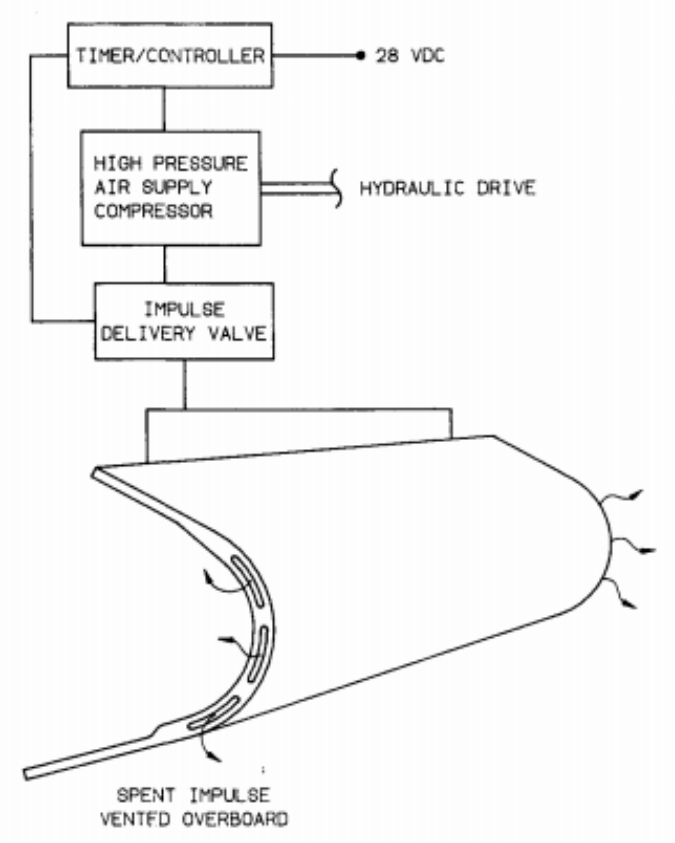

Figure 1.10: PIIP System Schematic [4]

Figure 1.10 shows the flow diagram of how the PIIP system functions. It can be seen that there is a need for a high-pressure air supply compressor which some aircraft may not be able to support due to the additional weight and power requirements. Again, the rubber material used for the boot is subject to erosion from environmental elements.

An area of ongoing development is the pneumatic boot material itself. During

the summer of 2016, the Goodrich Company filed a patent for a dual elastomer fiber boot construction [7]. This new method of manufacturing the elastic boot material uses a dual fiber construction to improve elastic characteristics. A schematic of this dual fiber layout is shown below in Figure 1.11.

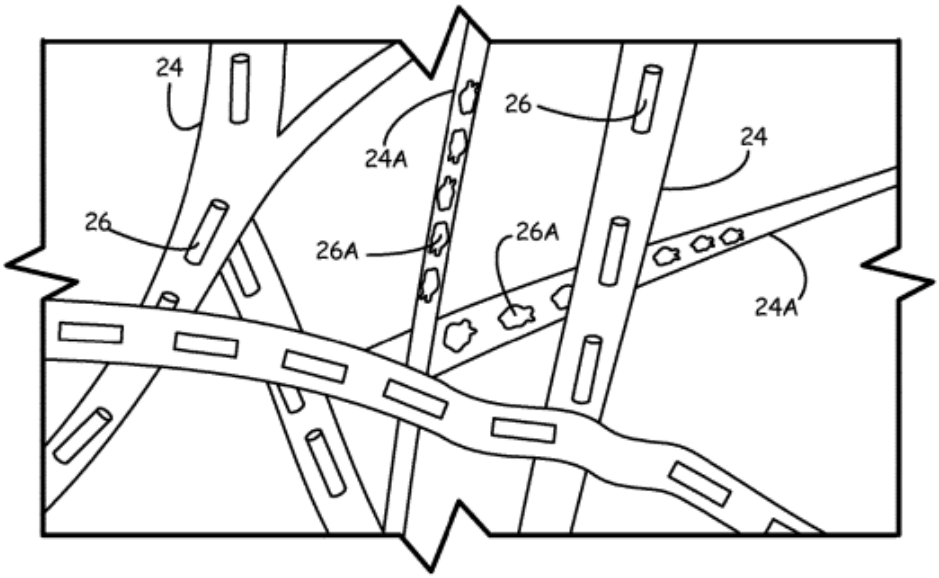

Figure 1.11: Dual Elastomer Fiber Layout for Pneumatic De-Icing [7]

Label "24" signifies an elastomer fiber and the label "26" represents carbon nanotubes. "24A" is a different type of elastomer fiber with "26A" representing carbon black, which is a byproduct of the incomplete combustion of heavy petroleum products. Having dual elastomer fibers allows the boot to be more elastic and optimized for strength, structural integrity, and conductivity. This improved elasticity and desired characteristics are achieved by the aligning of carbon allotrope materials with elastomer fibers at different loading levels which provides a non-woven fiber fabric sheet. The fibers themselves can also be of nanofiber (d $<$ 1000 nm) or microfiber (d $<$ 10 μm) in nature [7]. Having improved characteristics, such as strength, will improve the durability of the boot material. Also, a conductive

material will be able to be used as an electrothermal system. Potentially, the material can be optimized for both its elastic dexterity and conductivity receiving benefits of both pneumatic and electrothermal IPS.

Another pneumatic de-icing technique uses a metal material, rather than an elastic material, that covers the leading edge with an inflatable cavity. The leading-edge metal material is relatively thin, 0.03-in (0.762 mm) thick, to retain its dexterity and ability to deform with little applied pressure. The metal leading-edge shell is bonded to the airfoil via elastomers that can deform. The described pneumatic system in a deflated and inflated state is shown in Figure 1.12.

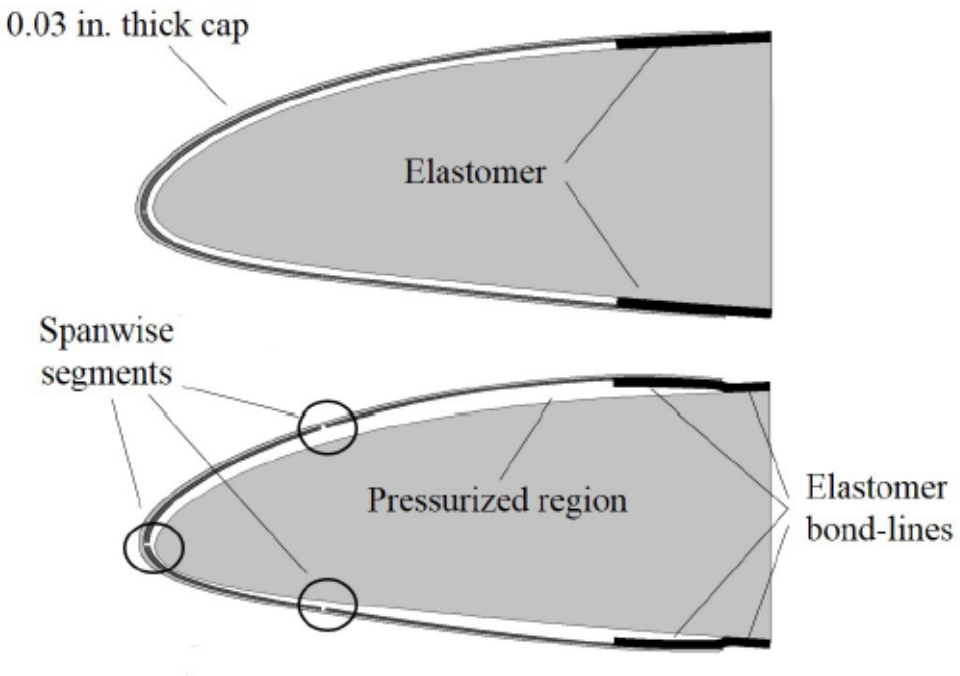

Figure 1.12: Single Cavity Pneumatic System [2]

The elastomer bond-lines allow the metal shell to deform creating the shear stress required to debond the ice like previously discussed pneumatic systems. This pneumatic de-icing system was conceived for rotorcraft applications where rubber

boots would not have enough structural integrity to be viable. The pressure difference that inflates and deflates the leading-edge cap is created by centrifugal pumping which occurs when rotor blades naturally rotate. The de-icing system consumes some of the power used to spin the rotor. The system that generates the pressure difference is shown below in Figure 1.13.

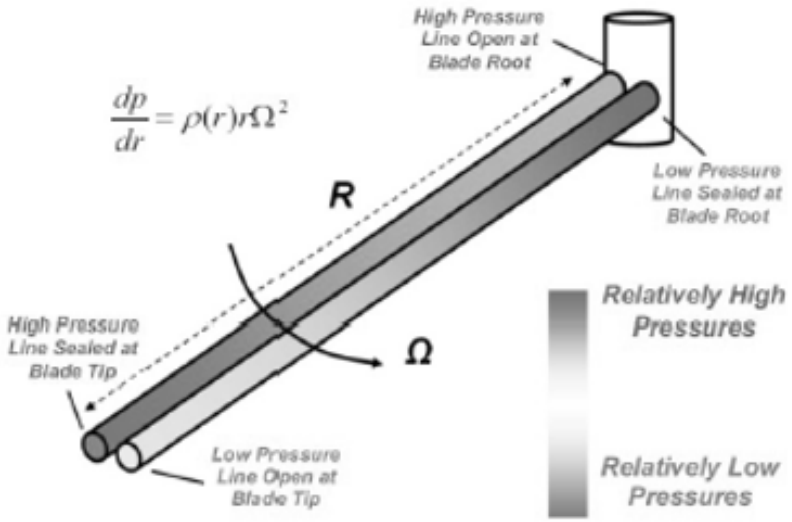

Figure 1.13: Centrifugal Pumping Mechanism [2]

There are two pressure lines that run span-wise, one high pressure and the other low pressure. Both lines are pressurized/depressurized by the rotor spinning. The pressure difference between the high and low-pressure lines is the force which inflates and deflates the shell on the airfoil. From testing, more power is required to deflate the system than to inflate it. This specific system can remove ice with as little thickness as 0.078-in (1.98 mm) at -14°C and 0.112-in (2.845 mm) at -5°C. Compared to a conventional electrothermal de-icing system, this system required 84% less power [2].

1.4.3 Low Adhesion Strength Coatings

A third IPS, which is conceived as being completely passive in nature, is low adhesion strength coatings. Coatings able to completely prevent ice accretion in aircraft representative environments do not exsist to date, but research is ongoing in the quest of passive ice protection coatings [12, 16, 17, 17, 19, 22]. The function of these coatings is to lower the adhesion strength between the ice and the surface of the aircraft so that the ice sheds at a faster rate. For rotorcraft applications, having a coating on the blades aims to have the ice shed naturally due to centrifugal forces. Aircraft coatings are usually paired with another IPS to improve the overall performance of the system. The effectiveness of a coating is measured as the adhesion strength, usually measured in units of lb/in^2. Ref. [34] conducted ice adhesion strength tests of several different coatings using impact ice on a rotor stand. The experimental setup is illustrated in Figure 1.14.

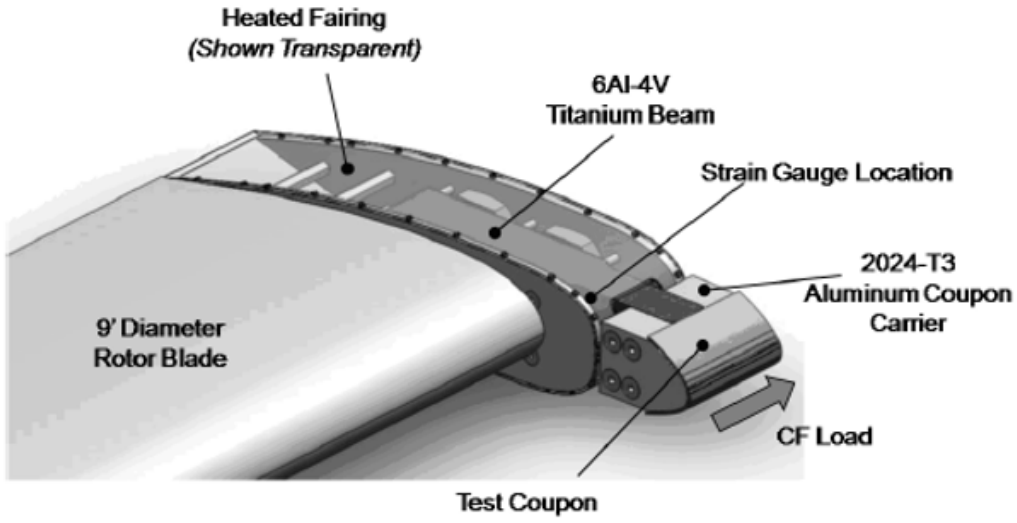

Figure 1.14: Adhesion Strength Experimental Configuration [34]

The low adhesion strength coating is applied to a test coupon and mounted on the

coupon carrier. Once the rotor is brought up to speed, an icing cloud is turned on and ice begins to accrete to the Test Coupon. Once there is a jump in the strain gauge voltage values, the ice has shed off the coupon. The adhesion strength is quantified by Equation 1.1.

$$Adhesion\ Strength = \frac{V_{shed} - V_{Final}}{Area} \frac{M_{tip} R (RPM \frac{\pi}{30})^2}{V_{RPM} - V_o} \tag{1.1}$$

Where $Area$ is the area of the shed ice and M_{tip} is the structural mass of the tip of the blade. The relevant voltages needed in Equation 1.1 are labeled in Figure 1.15.

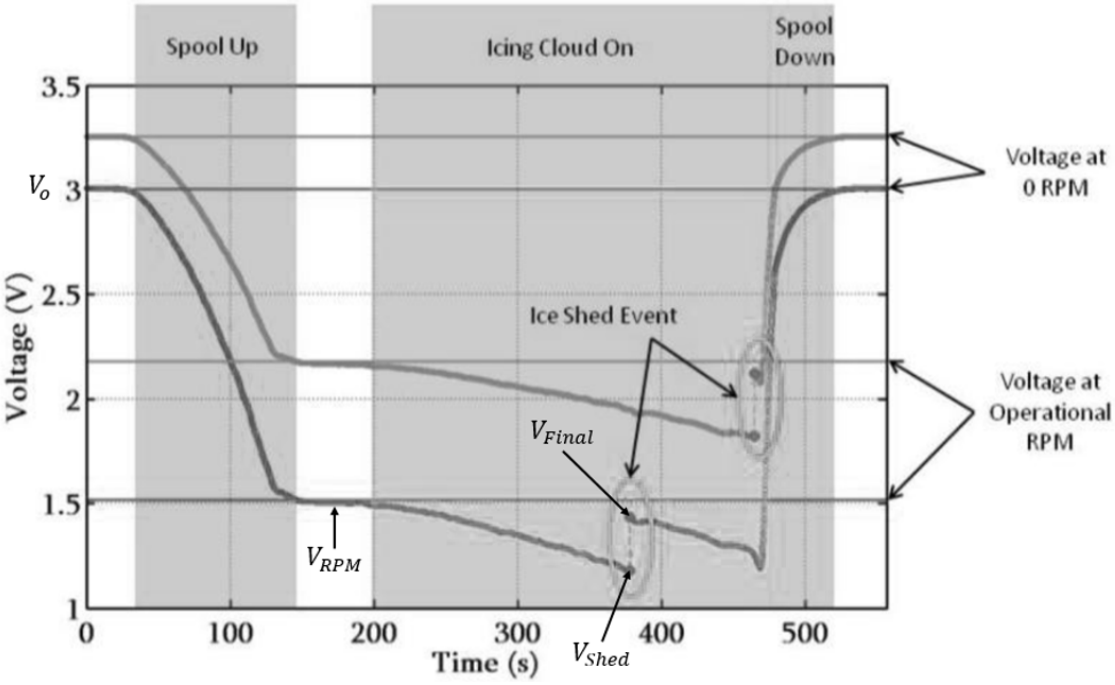

Figure 1.15: Adhesion Strength Testing Voltages [35]

The results of the adhesion strength testing are shown in Figure 1.16. Each coating was tested and then eroded by exposure to a sand loading of 8-10 g/cm^2 with angular quartz and then retested.

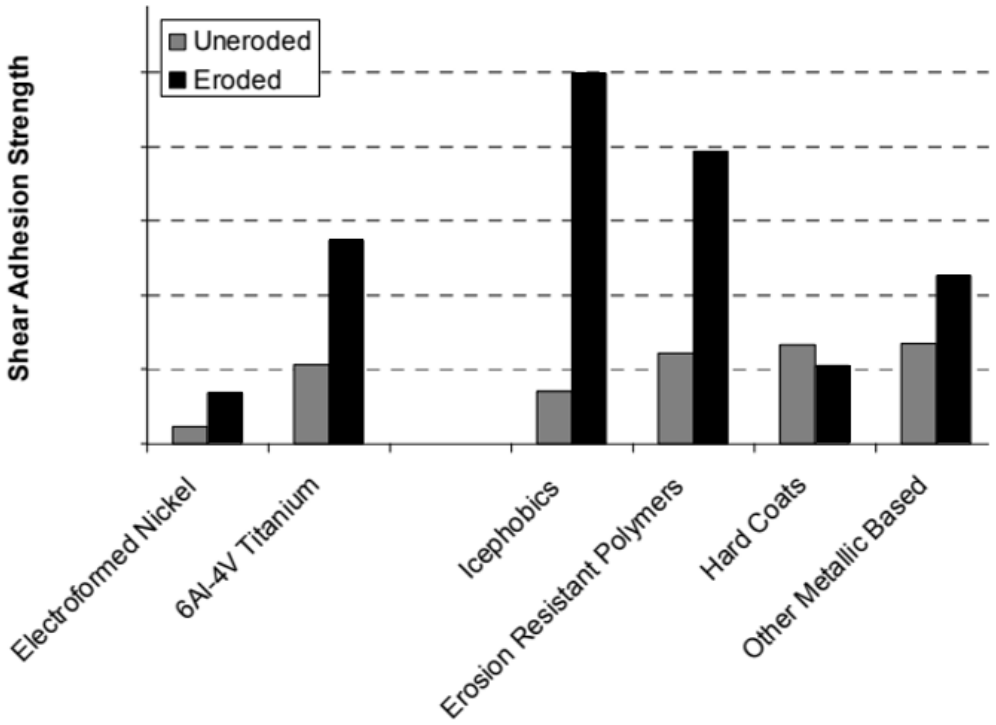

Figure 1.16: General Coating Adhesion Strength Results [34]

Before erosion, both the Electroformed Nickle and Icephobic coating performed well. After the erosion, the Electroformed Nickle coating still yielded an adequate adhesion strength while the "Icephobic" coating dramatically worsened showing that Icephobic coating generally under-perform after being eroded.

Currently, despite the significant erosion issues, there is still an abundance of research on "Icephobic" coatings, particularly superhydrophobic coatings. Superhydrophobics are materials that repel water droplets and hence are called “ice phobic.” The surface of a super hydrophobic coating forms a contact angle between the material and the water droplet greater than 90° which prevents the droplet from collapsing due to cohesive forces. The large angle arises due to the superhydrophobic material’s surface morphology. The described contact angle is illustrated below in Figure 1.17.

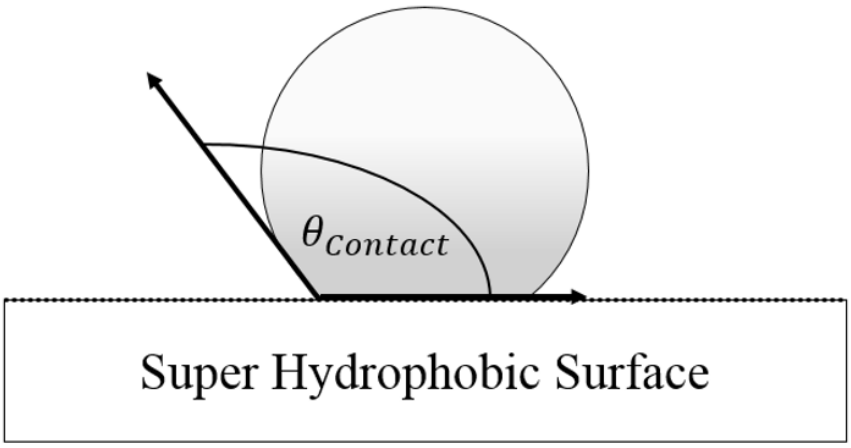

Figure 1.17: Super Hydrophobic Contact Angle

Research conducted (Ref. [16–19]) concluded that superhydrophobics are only capable of delaying ice accretion, but in time ice accretion will be seen. In other experiments, the testing conditions are not truly representative of aircraft icing environments in that the temperatures are too warm and the impact velocities are too low [20,36–38]. At warmer temperatures, water droplets can impact the aircraft and roll aft due to the large contact angle meaning superhydrophobics yield lower surface wetting. During testing similar to Ref. [20, 37, 38], liquid water rivulets can form which contain coalescing droplets. These water rivulets can be large enough in size to foster Cassie-Baxter states which describes a heterogeneous wetting scenario where the droplets do not saturate the gaps in the superhydrophobic's surface morphology resulting in misleading conclusions [39].

A significant problem that arises with superhydrophobic coatings is their durability. The results of a study of how super hydrophobic coatings decay over repeated tests are summarized in Figure 1.18. These tests were conducted at Penn State's AERTS lab at -12°C, a LWC of 2.0 g/m^3 , a MVD of 20 μm, and a tip speed of 59 m/s [36].

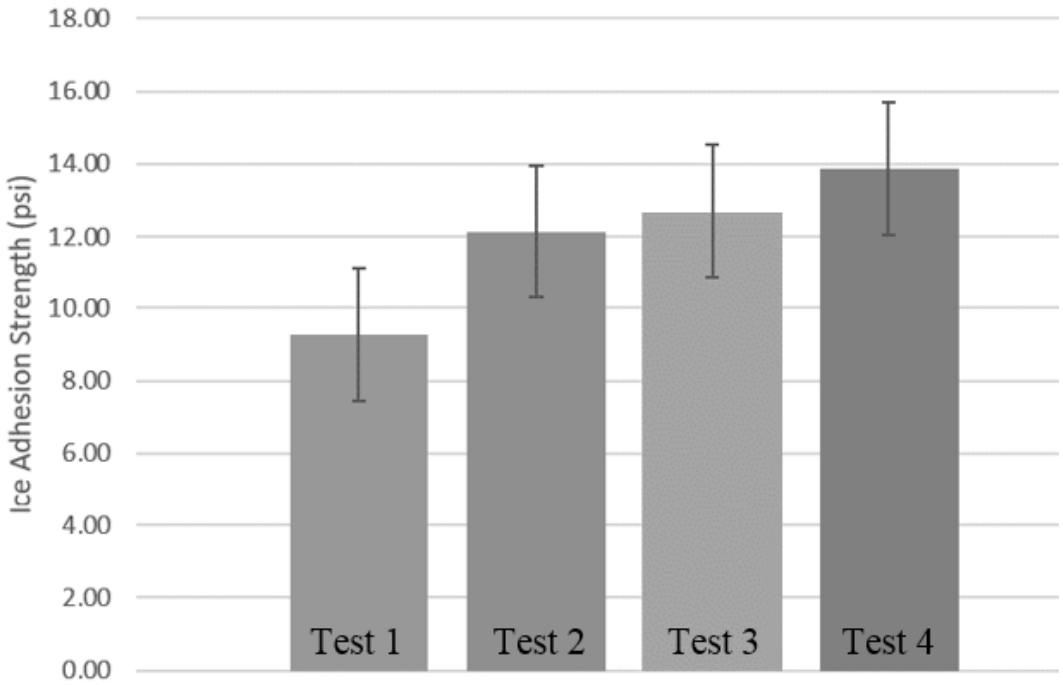

Figure 1.18: Adhesion Strength of Ultra Ever Dry (Super Hydrophobic) [36]

After Test 1, the adhesion strength decreases by 33% and then continues to decrease. A trend of decreasing adhesion strength shows that super hydrophobics tend to deteriorate quickly matching previously shown trends. This is one of the major problems facing low adhesion strength coatings, they tend to deteriorate after continued use, especially in rotorcraft applications where the incoming velocity is greater than that of fixed wing aircraft.

Despite superhydrophobic's poor performance as a primary IPS on the leading edge, a beneficial use of superhydrophobic coatings is to use them on the trailing edge while also using an electrothermal system on the forward section of the wing. If the ice interface melts and runs aft, superhydrophobic coatings would prove to be very beneficial to prevent icing on aft control surfaces (Figure 1.19).

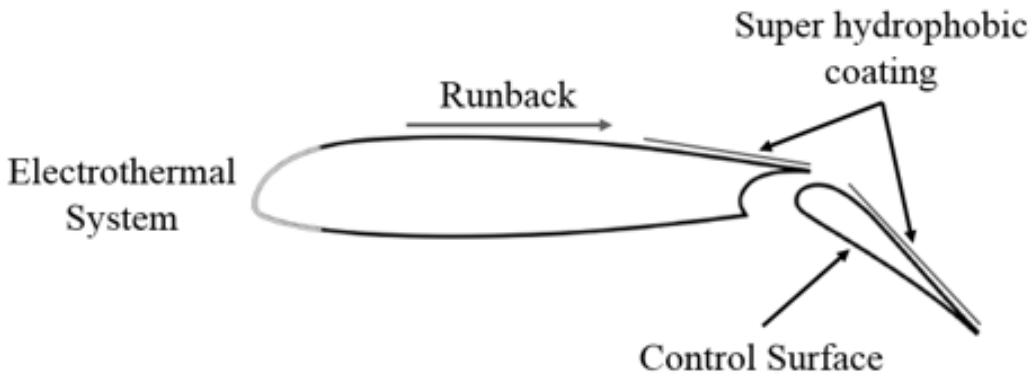

Figure 1.19: Super Hydrophobic Coating of Aft Section

1.5 Icing Testing Methods

Testing of IPS usually begins with scaled testing in a smaller testing facility to prove that the concept works as designed and to initially cut costs. As the IPS develops, testing is moved to a more sophisticated facility where a full-scale system can be tested. Eventually, after potentially many rounds of scaled testing, to be deemed ready for flight, the IPS will make it to full-scale in-flight testing.

1.5.1 Icing Tunnel Testing

There are many icing tunnels throughout the United States and around the world. Icing tunnels are typically used to verify a systems performance and computer simulations before transitioning to in flight testing. Tunnel testing allows for sub-scale models to be tested which can reduce testing costs although some tunnels are large enough to perform full scale testing. One of the most prominent icing tunnels in the United State is NASA's Icing Research Tunnel (IRT) located at NASA Glenn in Ohio. The IRT has a 9 ft. (2.743 m) by 6 ft. (1.829 m) test section

and can achieve a test section speed of approximately 374 knots (430 mph, 192 m/s). A side view layout of the IRT is illustrated in Figure 1.20.

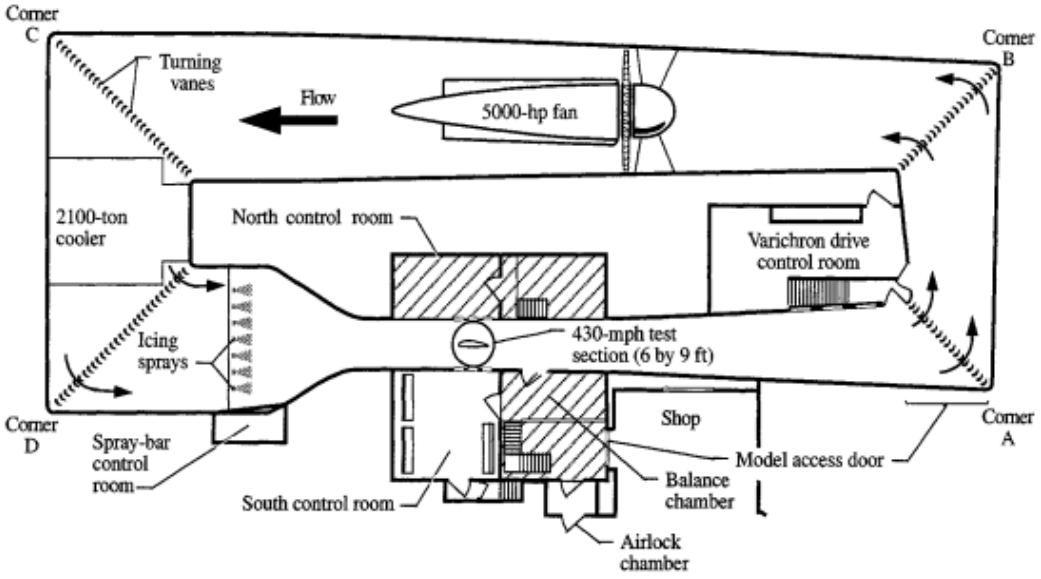

Figure 1.20: NASA's Icing Research Tunnel [40]

The test section is downstream of the spray bars by a specific distance that allows the water droplets to become super-cooled before impacting the test model. The spray bar contains nozzles that can be controlled via air and water pressure to manipulate the icing cloud in the test section. Icing tunnels can vary greatly in size, and the chosen tunnel is decided by the size of the system being tested as well as budget. Icing tunnels can test down to devices such as pitot probes and up to full scale trains. The Climate Wind Tunnel (CWT) in Vienna has a test section 5.6 m (18.37 ft.) wide and 6.2 m (20.34 ft.) tall which can simulate rain, snow, and ice [41]. There are many other icing tunnels in operation of varying size such as Boeing's Research Aerodynamic Icing Tunnel [42], Goodrich Icing Wind Tunnel [43], and Cox and Company's Icing Research Facility [44].

1.5.2 Rotor Stand Testing

Rotorcraft too need to test their de-icing systems before being implemented. A rotor can be placed in a wind tunnel, but the direction at which the water droplets impact the rotor is not accurate over the span. To accurately produce conditions experienced in flight, an icing rotor stand was constructed at Penn State's AERTS facility. The facility can produce icing conditions in correspondence to FAR requirements [24]. A schematic of the icing rotor stand in the AERTS facility is shown in Figure 1.21.

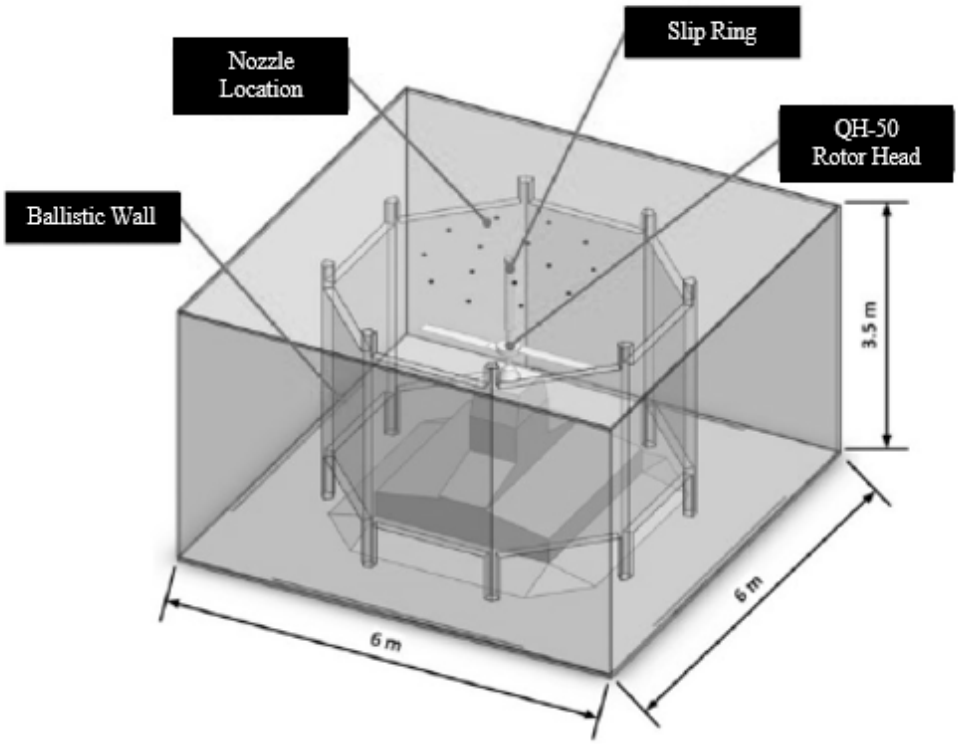

Figure 1.21: AERTS's Icing Rotor Test Stand [24]

The AERTS rotor stand can spin 5 ft. (1.524 m) radius blades while varying

the collective and cyclic pitch using a QH-50 hub. The AERTS rotor stand was constructed with de-icing testing in mind; therefore, there are options for both an electrical and a pneumatic slip ring [24].

In total, there are 15 NASA standard nozzles located in the ceiling of the AERTS facility which generate the icing cloud. Each nozzle can be individually turned on or off yielding the ability to control the LWC of the cloud. The nozzles are arranged in two concentric circles having 10 nozzles on the outer ring and 5 on the inner ring. The outer ring of nozzles has a diameter of 84-in (2.134 m), and the inner ring a diameter of 40-in (1.016 m). Having and inner and outer ring of nozzles allows for a uniform cloud along the span of the rotor blades. On the outer ring, there are two separate systems, the Super-cooled Large Droplet (SLD) System and Appendix C System (Figure 1.22 (b)). Using two systems, each on its own air and water supply, can produce a bi-modal cloud [45]. Like icing tunnels, the test plane must be a specific distance from the spray system so that the water droplets have sufficient time to become super-cooled. A schematic of the ceiling spray system is shown in Figure 1.22.

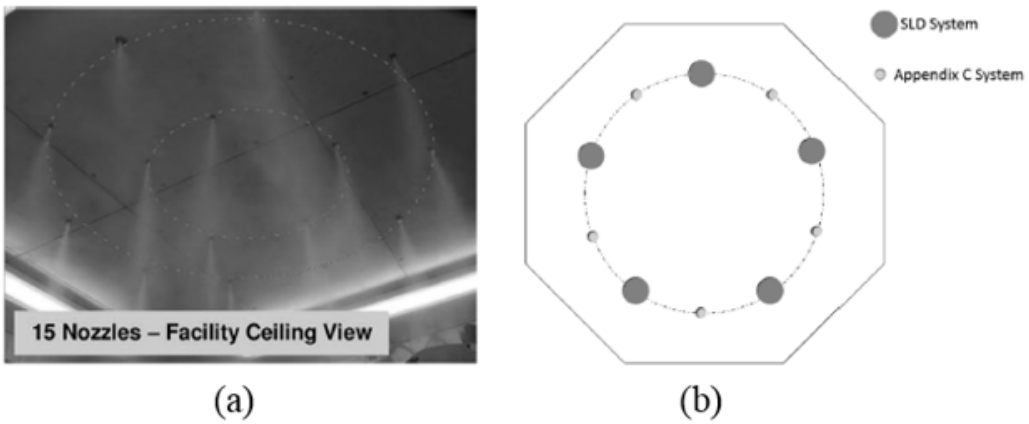

Figure 1.22: (a) AERTS Rotor Stand Ceiling Layout (b) Nozzle Configuration [45]

The AERTS facility was shown to be able to replicate ice shapes acquired during testing at NASA's IRT covering Appendix C icing conditions [10]. At relatively cold conditions with small droplet sizes, the difference between icing tunnel and rotor stand ice shapes are small. As the temperatures and droplet size increase, the centrifugal force causes the water that does not instantly freeze to run span-wise along the rotor blade changing the ice shape; therefore, at warmer temperature and larger MVD, differences become evident between the AERTS rotor stand and NASA's IRT.

1.5.3 In Flight Testing

If an aircraft component is too large for wind tunnel or rotor stand testing, the other option is in flight testing. There are two methods of in flight testing which differ by how the icing cloud is generated. The first method is deemed "weather chasing" where the icing conditions are naturally produced. This method requires the testing team to wait for the correct weather conditions that would yield the desired icing environment. "Weather chasing" is easier for long range aircraft because the aircraft can fly for longer durations and can operate at a large range of altitudes making finding the correct conditions easier. The second method of in flight testing is when the icing environment is created artificially. This method is more suited for general aviation aircraft and helicopters where range and altitude are more limited. Having an artificial icing cloud will likely reduce the cost and duration of the testing campaign [46]. One testing configuration of an artificially created icing cloud at the Canadian National Research Council (NRC) Low Temperature Facility where a helicopter hovers behind a spray system is shown in Figure 1.23.

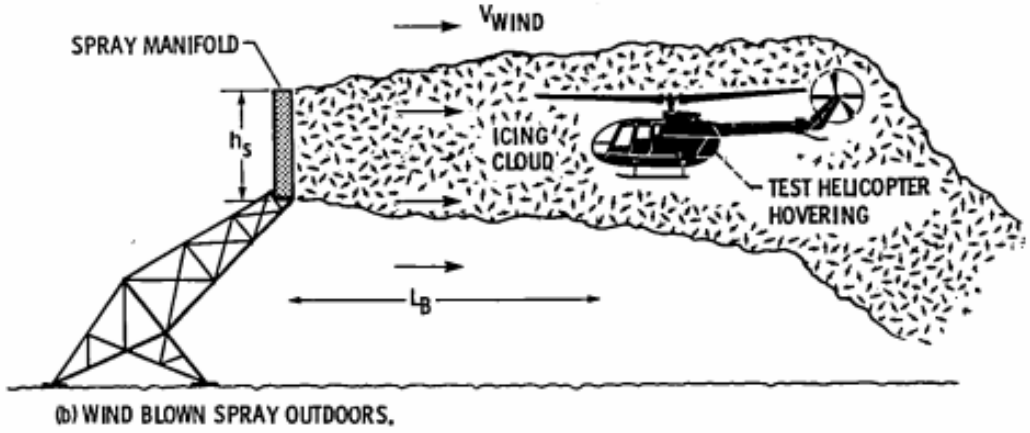

Figure 1.23: Canadian NRC Low Temperature Testing System [46]

The Canadian NRC Testing System had inherent safety flaws which led to its closure. Figure 1.23 shows a low speed test since the water particles are accelerated by natural winds. Slow airspeeds might not be sufficient for all icing testing, so another in flight testing system is the Army's Helicopter Icing Spray System (HISS) (Figure 1.24).

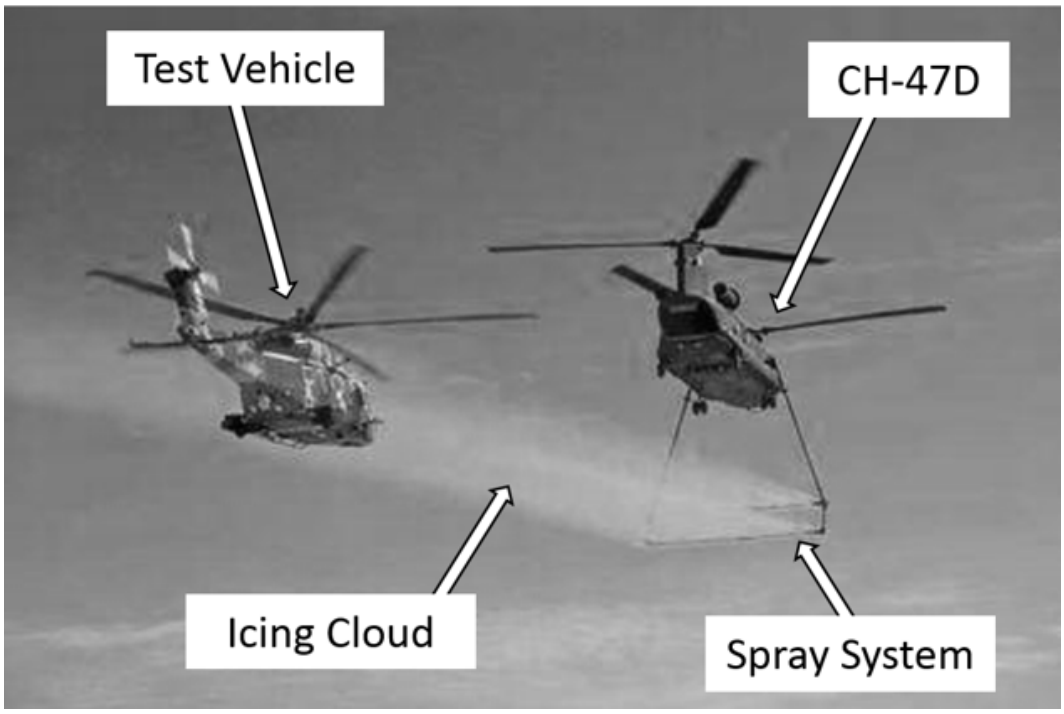

Figure 1.24: Army's HISS Testing [8]

The HISS can produce icing clouds with an LWC between 0.25 g/m^3 and 3 g/m^3. The icing cross sectional profile that the spray system produces is 8 ft. high and 36 ft. wide. Once the spray system has reached a steady state, a chase plane with wing mounted equipment enters the cloud to verify that the icing conditions are consistent with what is desired [47]. Tanker spray systems like the HISS have drawbacks though. According to Ref. [22], a lot of ice builds up on the nose of the aircraft which indicates that there are large droplets (SLDs) in the icing cloud. The desired small droplets would only accrete to a small stagnation region at the nose of the aircraft resulting in a small amount of ice. Ref. [47] also reported that the military tankers like the HISS were producing droplet sizes 2 to 20 times the desired size of 20 μm during testing.

1.6 UAS Icing

UAS have had an increasing role in aviation including Intelligence Surveillance Reconnaissance (ISR), agricultural purposes, search and rescue, aerial photography, and scientific research. UAS usually fly at lower altitudes than larger aircraft where icing environments are more frequently encountered [3]. While operating in all these encompassing roles, there are instances where UAS encounter icing environments where de-icing systems need to be employed. Due to the expanding use of UAS, more instances of icing will likely be reported in the future.

The United States Military, a large holder of UAS, has reported issues with UAS icing in the recent past. The United States Military reported that on December 13th, 2012 that the Navy lost a MQ-8B Fire Scout due to "icy conditions" with witnesses on the USS Robert G. Bradley stating that they saw "a two-foot chunk of ice fall off the tail." [48]. Also, Ref. [49], a reliability study conducted by the Department of Defense, states that at least three MQ-1 Predators and two IAI RQ-5 Hunter drones crashed with icing as a primary cause. According to a Congressional Research Study (Ref. [50]), over the period of 2002 to 2010, the Department of Defense's UAV inventory increased by more than 40 times. Also, the monetary investment in UAVs has increased from $284 million in 2000 to $3.3 billion in 2010. With the growing use of unmanned aerial vehicles (UAVs), particularly for the military, icing could become more evident.

In piloted aircraft, the pilot usually notices the ice building up on parts of the aircraft through sight or feel and can engage the IPS. Therefore, an autonomous system must be present on UAS to calculate when sufficient ice is present to

employ the IPS. There has been recent development to fabricate a highly accurate autonomous ice detection system to be used in UAS. One area of ongoing research on ice detection involves systems that utilize neural networks [9]. The structure of the feed-forward neural network given two inputs, M_α and M_{δ_E}, which are stability and control derivatives of the aircraft is shown in Figure 1.25.

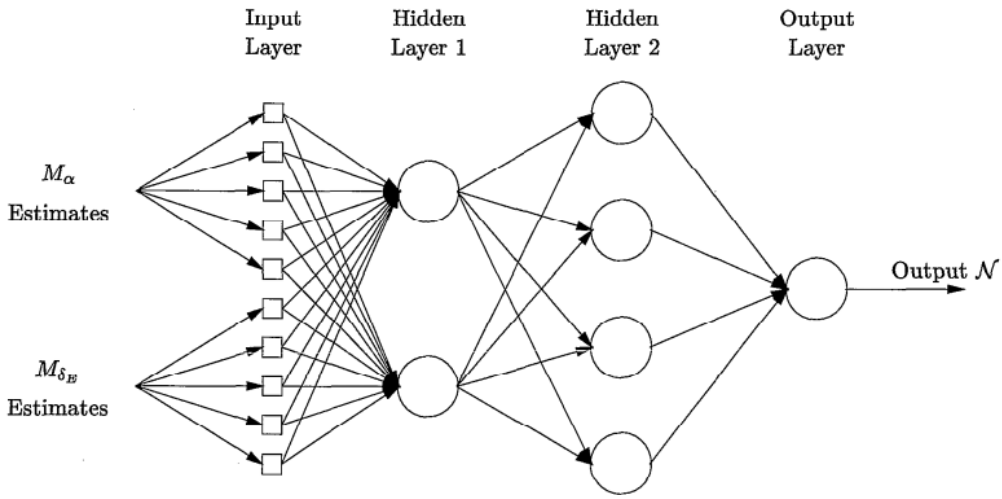

Figure 1.25: Feed-Forward Neural Network Structure [9]

Using neural network techniques, the autonomous ice detection system can better detect when icing is occurring and possibly the amount of ice that has accreted. The only drawback of implementing a neural network is that requires test data which may not be abundant. A lot of test data must be given to the neural network to be as accurate as possible. Also, a recurrent neural network is more modern and would provide more accurate results, but no published work attempts to implement such a network to aircraft icing detection.

The neural network scheme presented above is specifically for manned fixed wing aircraft, but could have potential in rotary UAS. One method to detect icing on rotary UAS is through measuring the sound levels coming from the rotors. Cheng

et al. (Ref. [51]) experientially showed a relationship between rotor broadband noise and surface roughness caused by icing. How the sound level changes with surface roughness is shown in Figure 1.26.

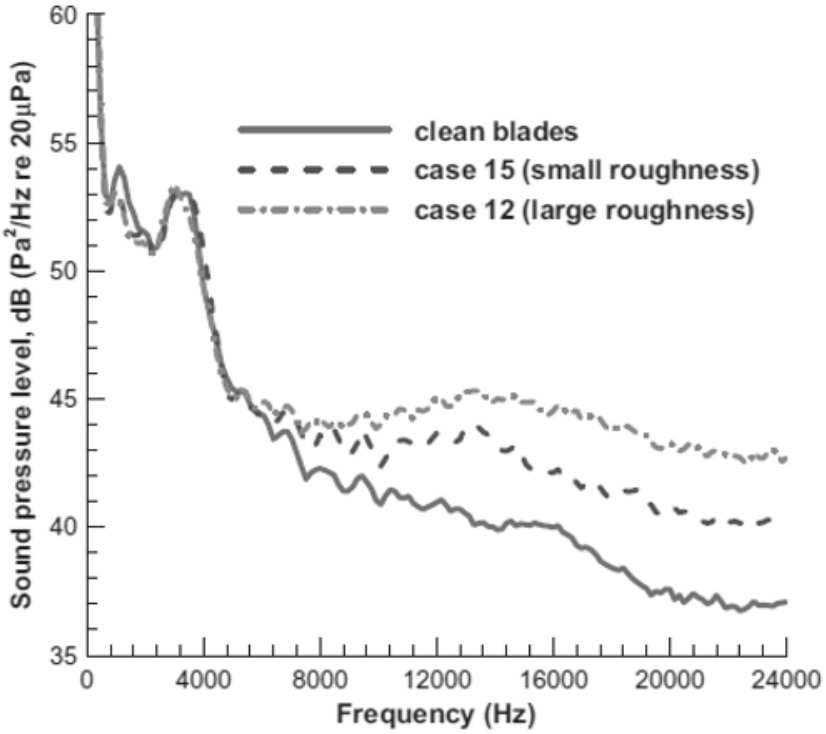

Figure 1.26: Sound Level versus Icing Induced Surface Roughness [51]

Generally, as the surface roughness increases (more ice has accreted) the broadband rotor sound level too increases. The differences in sound level can only be distinguished after 4000 Hz. This research could potentially lead to an audible signal from a rotary UAS characterizing the severity of icing and thus have the de-icing system(s) act accordingly.

UAS are more sensitive to weight and power consumption than traditional aircraft; therefore, improvements to common IPS must be made [3]. UAS IPS use the same concepts as discussed in Section 1.3, but use new techniques in attempt

reduce the size and power while increasing the efficiency. One such proposed improvement discussed in Ref. [3] is a new algorithm and implementation of an electrothermal system operating as both an anti-icing and de-icing system. What distinguishes this IPS is the newly developed algorithm that incorporates the wing's surface temperature and atmospheric measurements. The electrothermal IPS also employs what is deemed the Electrothermal Based Icing Detection Algorithm (ETB-IDA). The ETB-IDA implements a thermodynamic model of the aircraft's surroundings and addresses "icing detection in a fault diagnosis framework" [3]. The electrothermal source is composed of carbon nanomaterials and is applied to the wing of the aircraft as a coating. A schematic of the electrothermal IPS on the X8 Skywalker is shown in Figure 1.27.

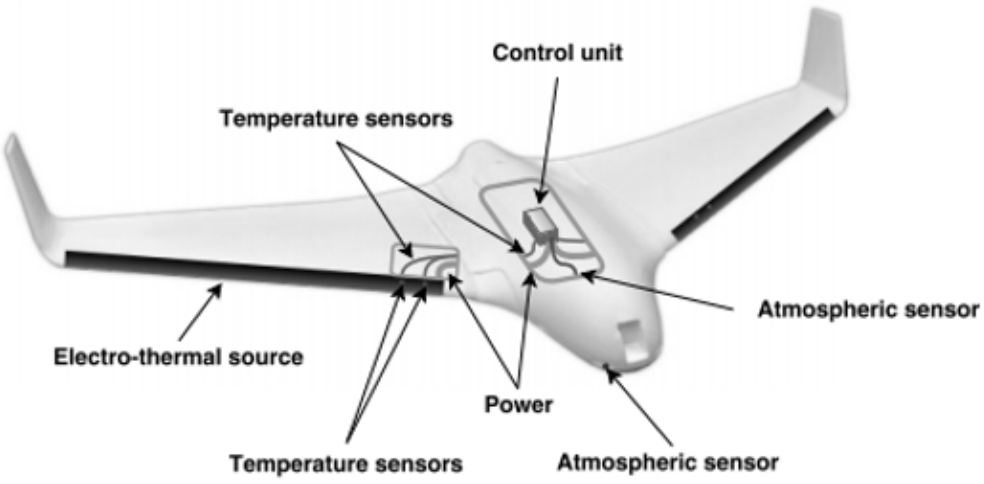

Figure 1.27: Electrothermal IPS onto a X8 Skywalker [3]

From test flight data, the electrothermal IPS maximum power consumed was 450 W, which was also the maximum available power showing that this system still needs improvement. The power to the IPS is supplied via a lithium polymer battery

or an onboard generator. Other than electrothermal systems, few other IPS have been explored for use in the UAS realm.

1.7 Thesis Overview

Chapter 2: Design and Analysis of a FEA Flat Plate Pneumatic-Impulsi

De-Icing System

In this chapter, the capabilities of Abaqus FEA are presented focusing on the ability to simulate an ice interface using cohesive elements. An overview of the needed fracture mechanics and traction-separation laws are too presented. The impulsive-pneumatic flat plate de-icing device is created and analyzed in Abaqus FEA. A mesh convergence study for both stress-strain and traction-separation relationships are presented. A method to quantify the delamination performance is shown. A study is conducted which compares the delamination performance of three inflation methods: static, symmetric dynamic, and asymmetric dynamic.

Chapter 3: Flat Plate Impulsive-Pneumatic Experimental Evaluation

An experimental system is fabricated which represents the flat plate Abaqus model. Experimental results to delaminate accreted ice are compared to the predicted performance found using Abaqus FEA. From the results, a cohesive surface modulus is found which represents stainless steel.

Chapter 4: Development of an Airfoil Abaqus FEA Model

The impulsive-pneumatic principles described in Chapter 2 & 3 are implemented onto an NACA 0024 airfoil in Abaqus FEA. The inflation techniques: static, symmetric, and asymmetric are compared for the airfoil model in addition to the propagation time in between boundary conditions being released. The affect of aerodynamic pressure on the airfoil de-icing system are presented.

Chapter 5: Airfoil De-Icing System Icing Tunnel Testing

The Abaqus model presented in Chapter 4 is fabricated into a NACA 0024 airfoil. This model is tested in AERTS icing tunnel for a range of testing conditions. The required pressure to de-ice the airfoil is compared to the Abaqus predicted pressure.

Chapter 6: Conclusions

Conclusions regarding the development and testing of the hybrid impulsive-pneumatic aircraft de-icing system are presented. Recommendations for future work on both the modeling and experimental configurations are also proposed.

Chapter 2

Design and Analysis of a FEA Flat Plate Pneumatic-Impulsive De-Icing System

2.1 Introduction

A pneumatic de-icing system requires pressure to sufficiently inflate to create adequate transverse shear stresses to delaminate the ice from the outer shell material. There is an added benefit when the shell inflates non-uniformly in an impulsive fashion which creates additional stresses and adds inertia effects that improve the de-icing capabilities. To model ice adhesion with impulsive-pneumatic effects, Abaqus FEA is used. A simple flat plate with attached ice is used to show the capabilities and methods of the FEA model. How this model is set up and the functionality of the cohesive methods is shown in this chapter.

2.2 Flat Plate Design

A pressure can be applied to a stainless steel plate causing a small deformation. If ice is accreted to the plate, during deformation, transverse shear stresses are present. Two parts are used to model the flat plate impulsive-pneumatic de-icing system: the plate with tabs and ice. The plate is 11-in (279.4 mm) in length and 0.03-in (0.762 mm) in thickness. Two tabs are on the underside of the plate where boundary conditions are applied (Figure 2.1).

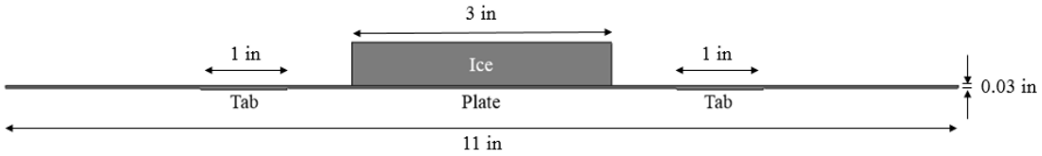

Figure 2.1: Plate and Ice Model in Abaqus

The model in Abaqus FEA with an applied pressure on the underside of the plate and boundary conditions are shown in Figure 2.2.

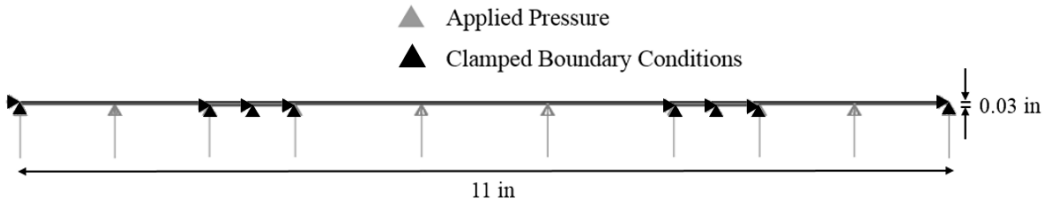

Figure 2.2: Plate Part Model under Load and Boundary Conditions

The boundary conditions on the edges of the plate are clamped, so there is no displacement or rotation. The plate is constructed of a 400 series stainless steel metal and the material properties are listed in Table 2.1.

Table 2.1: Material Properties of 400 Series Stainless Steel [52] [53]

Density	7800 $\frac{kg}{m^3}$
Modulus of elasticity	200 GPa
Poisson's Ratio	0.30
Structural Damping Ratio	3%

To analyze the effectiveness of the impulsive-pneumatic de-icing system, ice is attached to the plate using Abaqus's cohesive zone method. The material properties of ice used in this model are shown in Table 2.2, which is from research conducted by Ref [54].

Table 2.2: Material Properties of Ice

Density	918 $\frac{kg}{m^3}$
Modulus of elasticity	9 GPa
Poisson's Ratio	0.27

2.2.1 Static & Dynamic Steps

To run the Abaqus model, both static and implicit dynamic steps are used. When analyzing the traditional pneumatic system, only a static step is used due to inertial effects being negated. Once an impulsive effect is desired, an implicit dynamic step is introduced to capture the inertia effects of the ice and plate.

During a static step, the model can behave in a linear or nonlinear fashion. Time

dependent material effects such as creep, swelling, and viscoelasticity are ignored, but the model includes hysteretic and rate dependent plasticity behavior which are not necessarily selected by the user [55]. While the static step is running, nonlinear effects and large deformations are included in the analysis. The static model implements a direct equation solver with a full Newton solution technique [55]. The pressure which is applied to the plate is ramped linearly from zero to the desired pressure over the entire time.

Once the inertia effects desired due to the impulsive release of the plate are met, an implicit dynamic step is used. Again, a full Newton technique is implemented. During the implicit dynamic step, the FEA approximation to equilibrium is represented as

$$M^{NM}\ddot{\mathbf{u}}^{M} + I^{N} - P^{N} = 0 \tag{2.1}$$

where M^{NM} is the mass matrix and is defined as

$$M^{NM} = \int_{V_0} \rho_0 \mathbf{N}^{N} \cdot \mathbf{N}^{M} dV_0. \tag{2.2}$$

$\ddot{\mathbf{u}}^{M}$ is the second derivative of the displacement field (acceleration field) [55]. I^{N} is the internal force vector defined as

$$I^{N} = \int_{V_0} \beta^{N} : \sigma dV_0. \tag{2.3}$$

β is a parameter used in the Hilber-Hughes-Taylor integrator. Lastly, P^{N} is the external force vector which is defined as

$$P^{N} = \int_{S} \mathbf{N}^{N} \cdot \mathbf{t} dS + \int_{V} \mathbf{N}^{N} \cdot \mathbf{F} dV. \tag{2.4}$$

where $\mathbf{N}^N$ are interpolation functions, and superscript N are indices representing the material coordinates.

In the impulsive Abaqus model, a static step is initially used until one or both of the plate constraints are deactivated. Once deactivated, the static step ends and an implicit dynamic step begins. Once the model can propagate for a sufficient time, the implicit dynamic step ends and another static step begins to inflate the plate to a final desired state. There are two different types of impulsive cases. The first case is where both plate constraints release simultaneously creating symmetric inertia forces. The three steps that are used in the symmetric release case are shown in Figure 2.3.

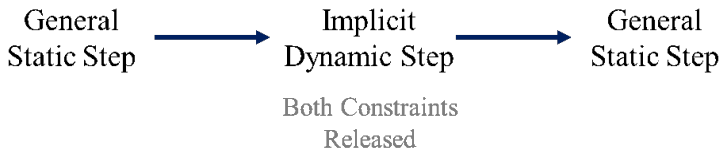

Figure 2.3: Impulsive Symmetric Release Case Steps

During the implicit dynamic step, at the beginning of the step, an impulsive force is applied to the plate and then the model can propagate for a short duration of time. After model propagation, the implicit dynamic step transitions to a general static step to continue to increase the pressure to an end state. The steps used for an asymmetric release case where one of the plate constraints is released and then the second is released after a prescribed time is shown in Figure 2.4.

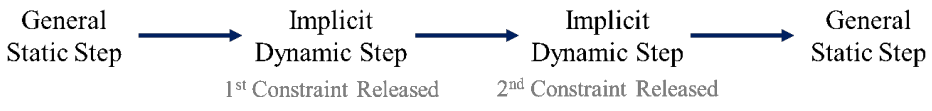

Figure 2.4: Impulsive Asymmetric Release Case Steps

During the propagation of the plate while the implicit dynamic step is running, damping is present. The main source of damping in the model comes from the plate's structural damping (Table 2.1).

2.3 Cohesive Behavior

Abaqus FEA can simulate the bonding characteristics of ice to the plate by utilizing cohesive surfaces. Using the cohesive surface outputs, the performance of the de-icing model can be quantified based on a method developed by Ref. [56]. The method that Ref. [56] presents is based on modeling composite delamination when small cracks form between layers of composite layers and propagate. The following subsections analyze how Abaqus employs cohesive behavior, and a brief review of cohesive failure theory.

2.3.1 Cohesive Material Theory

The bonding between the ice and the plate can be analyzed using cohesive zone methods. Unlike traditional behavior of stress-strain laws, the behavior of cohesive materials follows traction-separation laws. The main principle of cohesive zone method is that as two substrates are increasingly separated, the load carrying capability of the cohesive layer decreases. As the cohesive layer is damaged, the stiffness of the layer degrades which lessens the stress transfer capacity between two delaminating layers. Once the substrates have separated, which is defined by input parameters such as damage criteria, the cohesive layer has failed and can no longer carry any load [56]. Figure 2.5 illustrates a Mode I loading with the corresponding

stress versus separation plot.

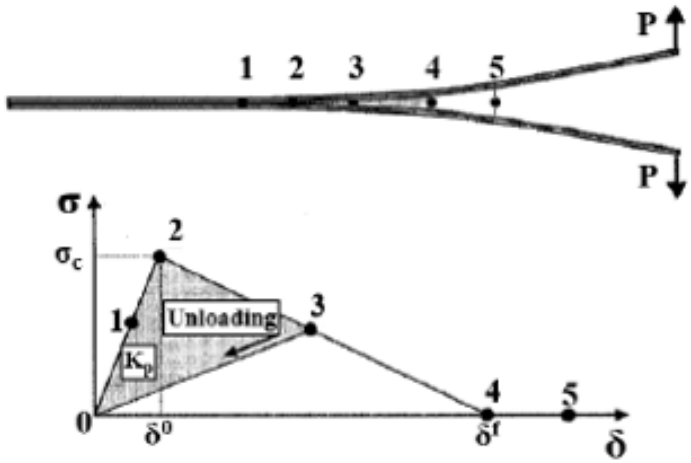

Figure 2.5: Mode I Loading (top) Stress vs. Separation (bottom) [56]

Point 5 in Figure 2.5 has failed; therefore, there can be no transferred stress which is shown in the bottom portion of Figure 2.5. Points 1 to 2 in Figure 2.5 show a linear elastic range where damage has yet to occur. In the linear region some penalty stiffness (K_P) exists which is responsible for holding the two layers together. K_P also defines the relationship between the separation of the two layers, defined by δ, to the surface tractions. Ref. [56] points out that point 2 in Figure 2.5 is where the damage is initiated and corresponds to the inter-laminar strength of the interface. From points 2 to 4, after damage has occurred, the stiffness progressively weakens, so the stress transfer too decreases. Once damage has been initiated, the separation of the layer can be expressed as

$$\delta_I^o = \frac{T}{K_P} \tag{2.5}$$

where T is the Mode I inter-laminar tensile strength. If S and N are the Mode II

and Mode III inter-laminar shear strength values respectively, then the separation can be expressed as

$$\delta_{II}^{o} = \frac{S}{K_P} \tag{2.6}$$

$$\delta_{III}^{o} = \frac{N}{K_P}. \tag{2.7}$$

Once the separation reaches the failure separation (δ^f), the stiffness becomes zero, so the cohesive component fails. If the fracture energy of the layer interface is given as (G_{IC}, G_{IIC}, and G_{IIIC}), then the failure separation can be calculated as:

$$\delta_{I}^{f} = \frac{2G_{IC}}{T} \tag{2.8}$$

$$\delta_{II}^{f} = \frac{2G_{IIC}}{S} \tag{2.9}$$

$$\delta_{III}^{f} = \frac{2G_{IIIC}}{N}. \tag{2.10}$$

The above separation values assume only one independent mode failure. In reality, a mixed mode loading will be experienced which presents another set of relationships. One such relationship is the power law which uses quadratic failure criterion to predict the damage initiation. If σ_z is the normal traction and the shear tractions are τ_{xy} and τ_{yz}, then the quadratic failure criterion gives

$$\sqrt{(\frac{\sigma_z}{T})^2 + (\frac{\tau_{xz}}{S})^2 + (\frac{\tau_{yz}}{S})^2} = 1 \tag{2.11}$$

for a positive σ_z and

$$\sqrt{(\frac{\tau_{xz}}{S})^2 + (\frac{\tau_{yz}}{S})^2} = 1 \tag{2.12}$$

for a negative value of σ_z. Both Mode II and III are considered shear dominated;

therefore, both modes have the same interfacial shear strength value, S [56]. For a mixed-mode loading condition, a relative separation value is calculated as

$$\delta_m = \sqrt{\delta_I^2 + \delta_{II}^2} \tag{2.13}$$

where δ_{II} is defined as $\sqrt{\delta_x^2 + \delta_y^2}$ and δ_z is the Mode I separation. Making the assumption that the penalty stiffness in Mode I and II are the same, the damage displacement (δ_o) for a mixed-mode loading can be calculated as

$$\delta_o = \delta_I^o \delta_{II}^o \sqrt{\frac{1+\beta^2}{(\delta_{II}^o)^2 + (\beta\delta_I^o)^2}} \tag{2.14}$$

where β is a mixed-mode ratio and is given by $\beta = \frac{\delta_{II}}{\delta_Z}$. Lastly, Ref. [56] defines the ratio of energy release rates of mixed-mode loadings to predict how delamination will propagate by

$$(\frac{G_I}{G_{IC}})^\alpha + (\frac{G_{II}}{G_{IIC}})^\alpha = 1. \tag{2.15}$$

where α is the power law coefficient and is either the value 1 or 2. The exact value of α is selected based on inter-facial behavior properties.

2.3.2 Abaqus Cohesive Methods

In an Abaqus model, surfaces or parts can be bonded together using a cohesive bonding. There are two cases of cohesive bondings: a cohesive surface or a cohesive element. A cohesive element is suited for models where the bonding would have a finite thickness such as a glue or epoxy. Alternatively, a cohesive surface is optimal for models where the bonding mechanism has a negligible thickness. To most

accurately model the ice/plate bonding, since there is no physical bonding layer, cohesive surfaces are to be used.

To be able to implement cohesive behavior in an Abaqus model, interaction properties must be defined. The required properties define the behavior of how the ice and plate surfaces will interact with one another under loading. As described in Ref. [11], cohesive behavior and damage contact properties can used to simulate the ice/plate bonding. Cohesive behavior contact properties allows the user to define if cohesive behavior can be repeated during post-failure contacts. In the case of ice delaminating, no post failure contacts would result in the reinitiation of cohesive behavior. Within the cohesive behavior property, the traction separation behavior is also definable being able to input the stiffness coefficients K_{nn}, K_{ss}, and K_{tt} corresponding to normal and shear directions.

Contact properties also allow the damage evolution and stabilization of the cohesive element to be defined. Once the cohesive element is found to fail, no load can be transmitted through it allowing the ice to delaminate from the plate. Abaqus has four criterion that indicate the cohesive element's failure: maximum nominal stress, maximum separation, quadratic traction, or quadratic separation. In the impulsive-pneumatic model, the initiation criterion used is the maximum nominal stress. The damage evolution is also definable specifically through displacement or energy methods. For a displacement evolution, the displacement at failure must be input. Once the total plastic displacement has been reached, the cohesive element has failed. Instead of displacement damage evolution, energy methods can be used, particularly fracture energy which is used in the impulsive-pneumatic model.

History output requests can be created that contain data sets that are used to

analyze the cohesive element degradation. There are many output variables, but the contact displacements variable, which is known as CDISP, is used to quantify the performance of the cohesive element. Within the CDISP output variable, there are outputs COPEN and CSLIP which correspond to fracture modes. The three fracture modes and their corresponding Abaqus variables are shown in Figure 2.6.

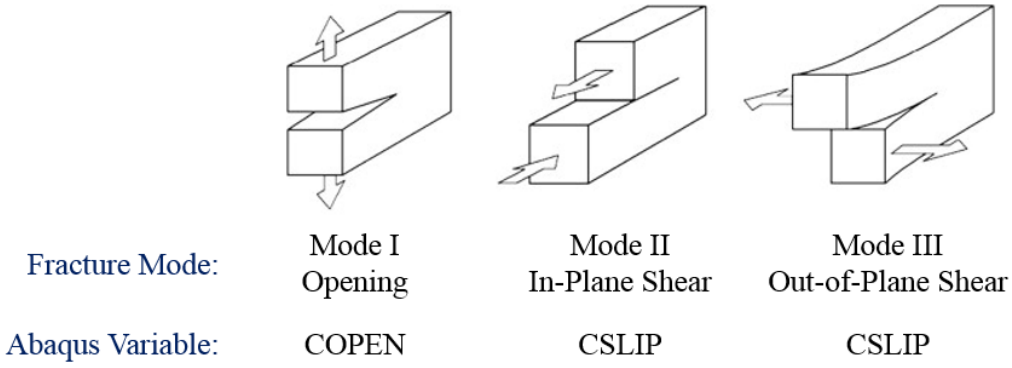

Figure 2.6: Abaqus CDISP Output Variables

The COPEN output variable corresponding to a Mode I opening can show the separation between the ice and the plate. The CDISP output variable contains data corresponding to the shearing modes II & III.

Table 2.3 comprises the cohesive behavior interaction properties discussed in this section and in Cohesive Material Theory. The ultimate strength modes (T, S, and N) are determined experimentally by Ref. [11]. The fracture energy (G), stiffness (K), and mixed-mode behavior were determined by Ref. [12]. These values were found specifically at -10° for pure water and an Aluminum bonding surface.

Table 2.3: Cohesive Properties used in Abaqus FEA [11] [12]

AbaqusOption	**Property**	**PropertyValues**
Elastic Type = Traction	Cohesive surface modulus K_{nn}, K_{ss}, K_{tt}	1 x $10^{12}\,\frac{N}{m^3}$
Damage Initiation Criterion = Quads	Ultimate Strength Mode I (T)	1 x $10^{12}\,\frac{N}{m^2}$
	Ultimate Strength Mode II (S)	1.95 x $10^{12}\,\frac{N}{m^2}$
	Ultimate Strength Mode III (N)	1.95 x $10^{12}\,\frac{N}{m^2}$
Damage Evolution Type = Energy	Mode I Fracture (G_{IC})	1 $\frac{N}{m}$
	Mode II Fracture (G_{IIC})	2 $\frac{N}{m}$
	Mode III Fracture (G_{IIIC})	2 $\frac{N}{m}$
Mixed-mode Behavior	Power Law (α)	2

2.3.3 Meshing

To run the Abaqus model, both parts need to be meshed. The mesh element type used is CPE8R which are 2-D, plain strain, biquadratic, reduced integration elements with eight nodes per element. A mesh convergence study is conducted to find the optimal mesh element size to ensure fast computational time and still preserve the accuracy of the results. This study is performed by tracking the displacement of a node on the center of the plate while decreasing the size of mesh elements until the displacement stops changing by less than 5%. Once the displacement of the selected node stops changing by the prescribed percentage, the current mesh element size will optimize model accuracy and computational time.

To run the mesh convergence, the pressure applied to the plate is linearly built

up to 3 psi over 3 seconds. At the end of the pressure buildup, the node location is recorded. The mesh element size is started at 7 mm and decreased by 1 mm each iteration until 5 mm and then decrease by 0.5 mm until the deformation changes by less than 5%. The results of the mesh convergence are shown below in Figure 2.7.

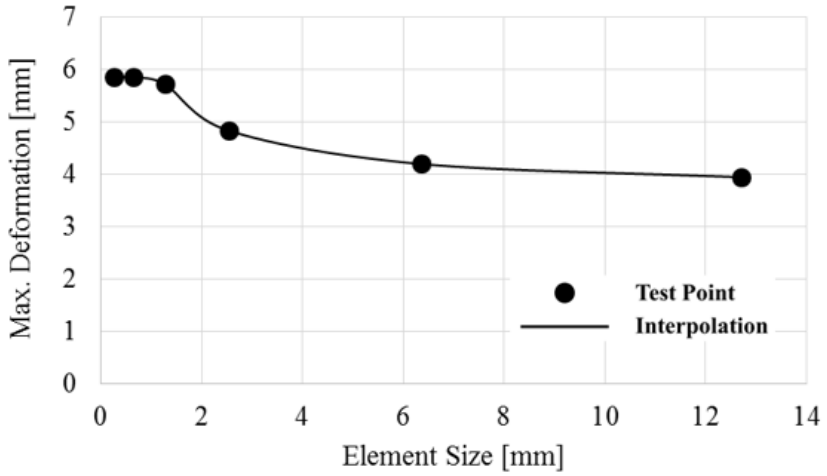

Figure 2.7: De-Icing System Mesh Convergence

The mesh size is not uniform throughout the parts, but rather is biased to lower the computational expenses. Therefore, the changing element size during the mesh convergence is both the top of the plate and the bottom of the ice where the cohesive behavior is most important. On the ice part, the important results come at the ice/plate interface, so the element size on top of the ice part is large and become smaller closer to the ice/plate interface. The meshing visualization of the described ice component is illustrated in Figure 2.8.

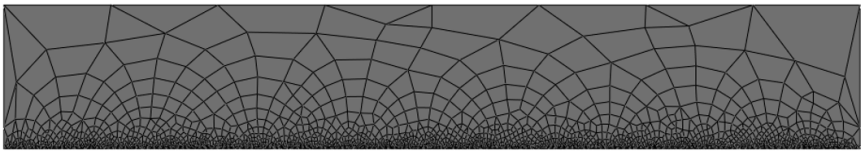

Figure 2.8: Abaqus - Ice Part Meshing

The ice stresses are not as important due to the assumption no ice internal cohesive failure occurs. Fracture of the ice is not considered in the Abaqus model. Although, the ice stresses cannot be ignored since the thickness of the ice will relate to the surface transverse shear stresses [57]. The stresses throughout the plate are valuable, so the element size in the plate does not vary greatly.

Once a convergence study has been completed that finds the optimal element size for stress-strain relationships, the element size must go another process due to the cohesive zone method. Ref. [58] performed a study that determines nodal displacement when the mesh sizing along the cohesive bounding line is changed. The results show that as element size in the direction of delamination (l_e) changes, the displacement continues to change. This result means that there will be no converging displacement value with decreasing element size. This phenomenon occurs due to "elastic snap-back instability which occurs after the stress reaches the peak strength of the interface [59]." The instability stems from the Newton-Raphson scheme radius converging to zero, in return diverging from an equilibrium state. Gao and Bower (Ref. [59]) conclude that if cohesive behavior is implemented in a model, a changing mesh size will have varying results given the same loading condition (Figure 2.9).

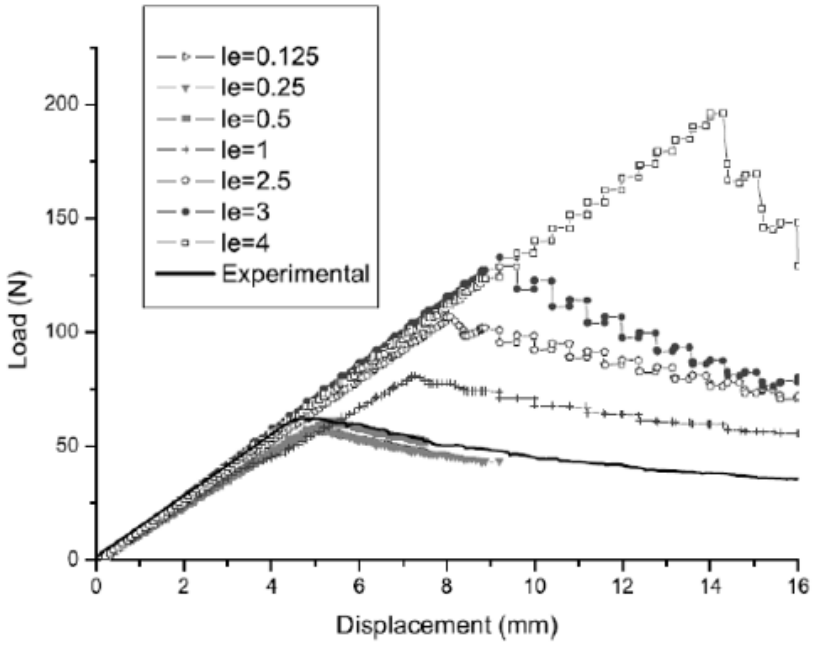

Figure 2.9: Nodal Displacement vs. Cohesive Element Length [58]

To verify the mesh size is accurate, experimental results are compared to simulation results. If the results are determined to be the same, then the mesh size used in the simulation is accurate. The mesh sizing is changed until the simulation results match the experimental results. This model tuning method of determining the mesh size is tedious and difficult. In addition, another method for preventing the solution from diverging is to add a small viscosity term in the cohesive interaction properties. Ref. [59] describes the validity of this technique for two and three-dimensional objects for both elastic and elastic-plastic materials. Introducing the viscosity term ensures that the simulation is rate dependent and will also introduce extra energy dissipation. The viscosity term is small enough that the energy dissipated is insignificant. Ref. [59] states that the energy dissipated by the additional viscosity term is equivalent to the energy radiated from the crack in the form of elastic

waves. Abaqus provides a viscosity coefficient parameter under the stabilization tab while defining the damage criteria within the interaction properties. A viscosity is chosen on the order of 10^{-10} to ensure the simulation converges and dissipates energy. Figure 2.10 shows how the addition of a viscosity term stabilizes the nodal separation with a changing mesh element size.

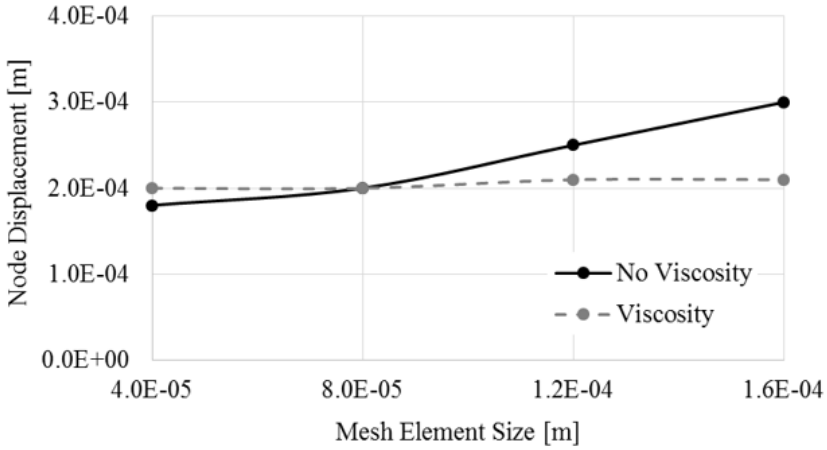

Figure 2.10: Effect of Viscosity on Nodal Separation at 1 psi

When the mesh size changes by factors of two, without the viscosity term, the nodal separation continues to vary. When a small viscosity term is implemented in the cohesive properties, the nodal separation changes much less stabilizing the solution. Table 2.4 shows the element sizing that is used in the flat plate model in addition to using a viscosity coefficient. Ref. [11] uses these element sizes for a model of similar physical dimensions, so mentioned size will be used in the flat plate model too with the assistance of a small viscosity coefficient. A confirmation that the cohesive element length is acceptable can be done by comparing to the element length found from stress-strain relationships, which is lesser in size, making the selected element length acceptable.

Table 2.4: Meshing Size for Flat Plate Cohesive Configuration [11]

Part	Element Length
Ice	0.86 mm
Plate	0.25 mm

2.4 Impulsive & Static Behavior Comparison

Using the constraining tabs described earlier, the dynamics of the deforming plate can be controlled. Specifically, the applied boundary conditions that constrain the tabs can be deactivated at different times. A study was performed to compare the results of three impulsive-pneumatic system configurations: static, symmetric release, and asymmetric release, all of which are described in the following sections. The effect of the applied pressure to the flat plate is also analyzed for the inflation types.

2.4.1 Method to Quantify Ice Delamination

The ice delamination is quantified by tracking the nodal separation between the plate nodes and the ice nodes. The separation of the nodes is tracked and plotted against the interface of the ice and plate which is normalized using the Abaqus output request CDISP which was described in Section 2.3.2. The nodal separation is the sum of the separation in both Mode I and Mode II directions. The line along which the nodal position is normalized is shown in Figure 2.11.

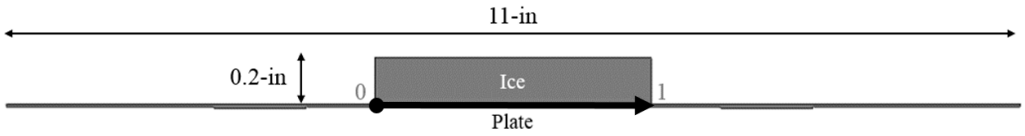

Figure 2.11: Normalized Path along Ice/Plate Interface

2.4.2 Static Deformation

Traditional pneumatic de-icing systems for fixed wing aircraft have uniformly inflating discretized cells that create localized transverse shear stresses and constructed of a rubber material [4,6]. Since the de-icing system design in this project implements a metal deforming shell, like rotor-craft pneumatic de-icing systems, only one large cell is inflated to create the required transverse shear stresses [2, 11]. This case was created in Abaqus for four loading conditions: 1 psi, 2 psi, 3 psi, and 4 psi. The applied pressure is linearly applied to the surface of the shell. The nodal separation results of the static deformation are shown in Figure 2.12.

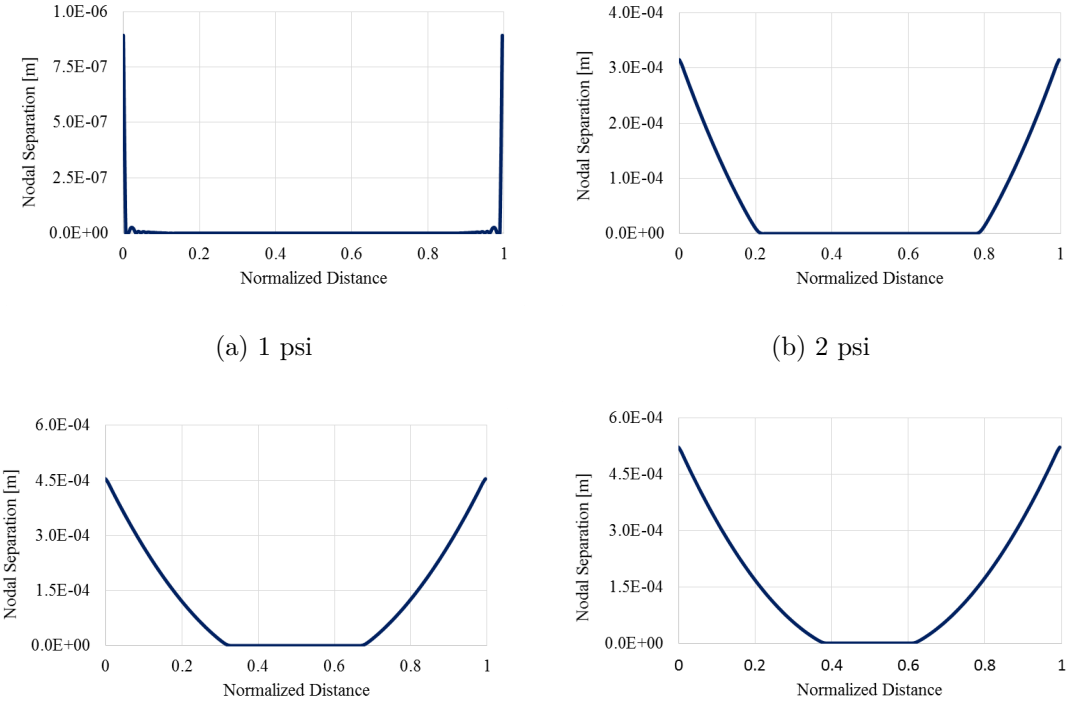

(a) 1 psi

(b) 2 psi

(c) 3 psi

(d) 4 psi

Figure 2.12: Nodal Seperation - Static Deformation

Figure 2.13 overlays the nodal separation of the four loading cases to illustrate the progression of ice delamination with an increasing applied pressure.

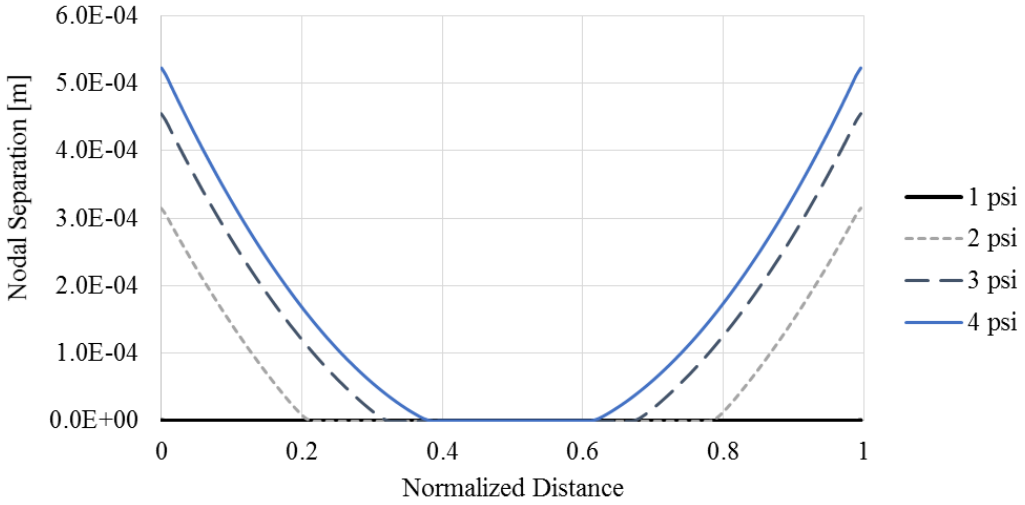

Figure 2.13: Static Deformation Nodal Separation Comparison

As the pressure applied to the plate increases, less of the ice remains attached to the plate. The percent of ice delaminated as a function of pressure for a static deformation is summarized in Figure 2.14.

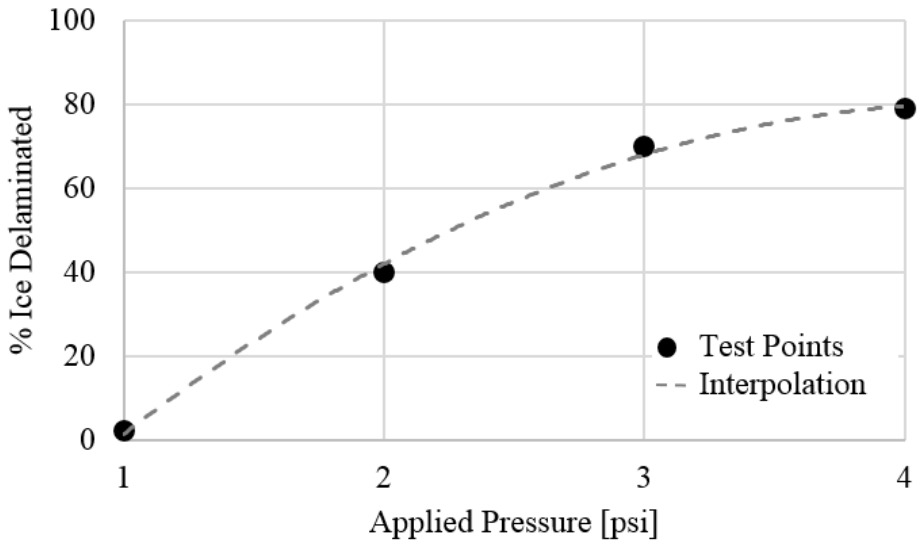

Figure 2.14: Static Deformation Nodal Separation Comparison

2.4.3 Symmetric Dynamic Deformation

The symmetric dynamic deformation is achieved by applying boundary conditions on the tabs of the plate initially. Once the dynamic step begins, both boundary conditions are deactivated simultaneously to introduce inertia forces that the ice and plate exert. The nodal separation results of the same four loading conditions for a symmetric dynamic deformation are shown in Figure 2.15.

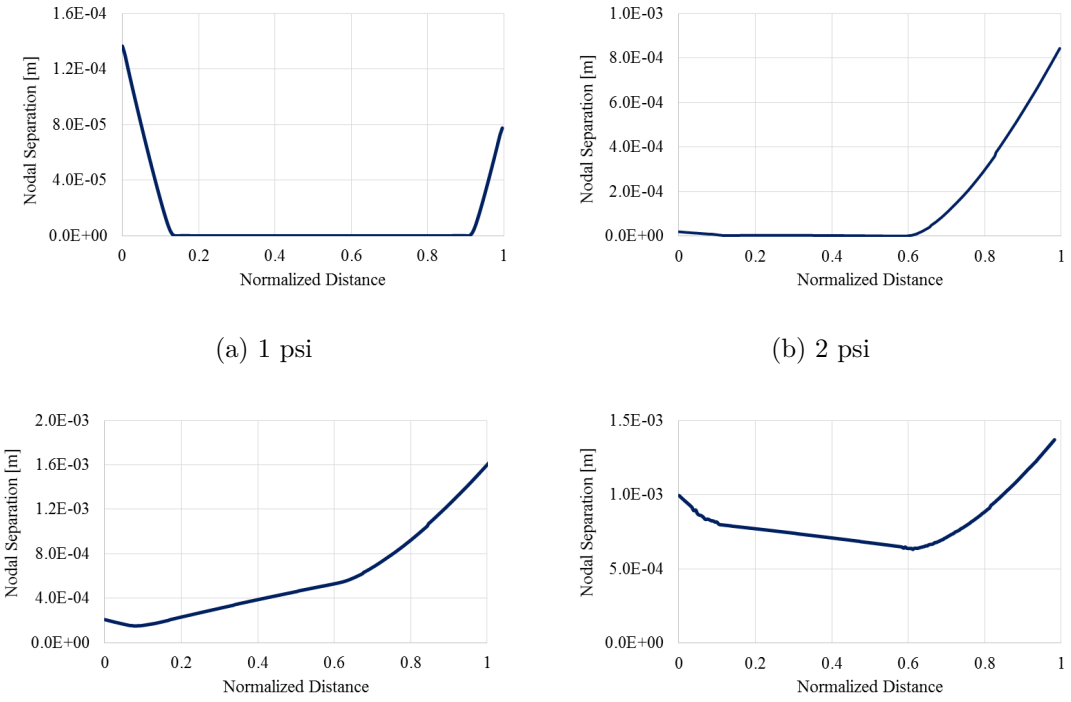

(a) 1 psi

(b) 2 psi

(c) 3 psi

(d) 4 psi

Figure 2.15: Nodal Separation - Dynamic Symmetric Deformation

During the first two loading conditions (1 and 2 psi), the ice remains attached to the plate. Once the loading condition reaches 3 psi, the ice completely delaminates from the surface of the plate. Again, as the pressure increases, the nodal separation also increases. The percent of ice delaminated as a function of pressure for the

dynamic symmetric case is shown in Figure 2.16.

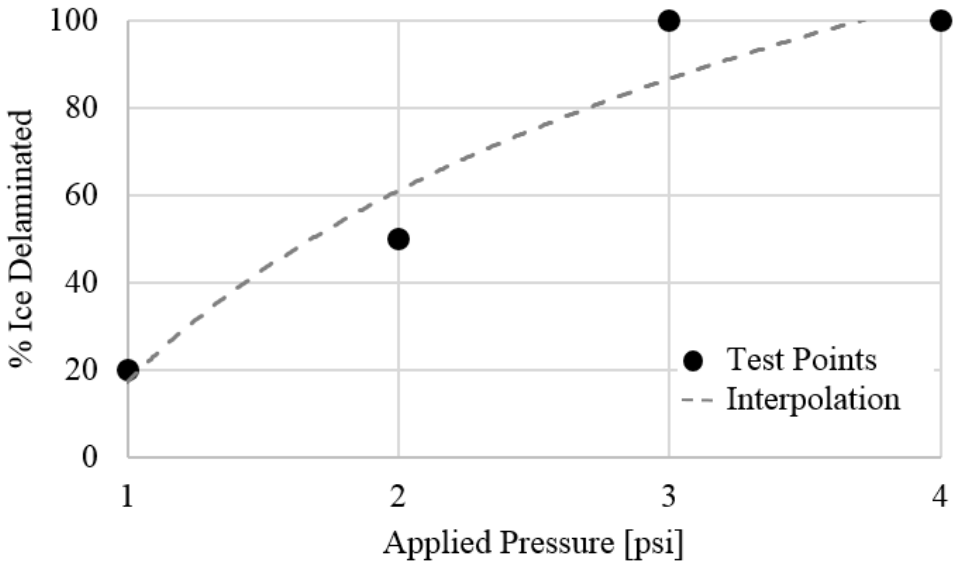

Figure 2.16: Dynamic Symmetric Deformation Nodal Separation Comparison

2.4.4 Asymmetric Dynamic Deformation

The asymmetric dynamic deformation is achieved by applying boundary conditions on the tabs of the plate initially. Once the dynamic step begins, one boundary condition is deactivated and the model propagates for a short duration. Once the second dynamic step is started, the second tab boundary condition is deactivated allowing the whole plate to move freely besides the ends which are still clamped. The nodal displacement results of the asymmetric dynamic deformation are presented in Figure 2.17.

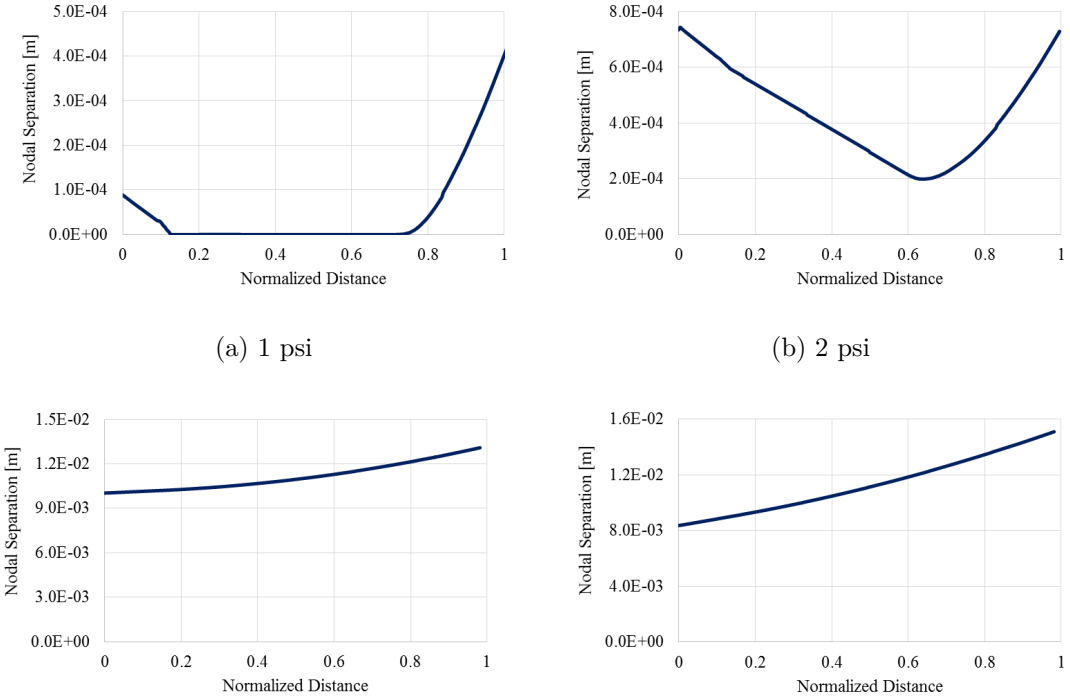

(a) 1 psi

(b) 2 psi

(c) 3 psi

(d) 4 psi

Figure 2.17: Nodal Separation - Dynamic Asymmetric Deformation

At 1 psi, the ice remains attached to the plate, but the edges have started to delaminate. Somewhere between 1 and 2 psi the ice fully delaminates from the surface of the plate. There is little difference between the 3 psi and 4 psi case where the ice has completely delaminated from the surface. The percent of ice delamined for the dynamic asymmetric case is shown in Figure 2.18.

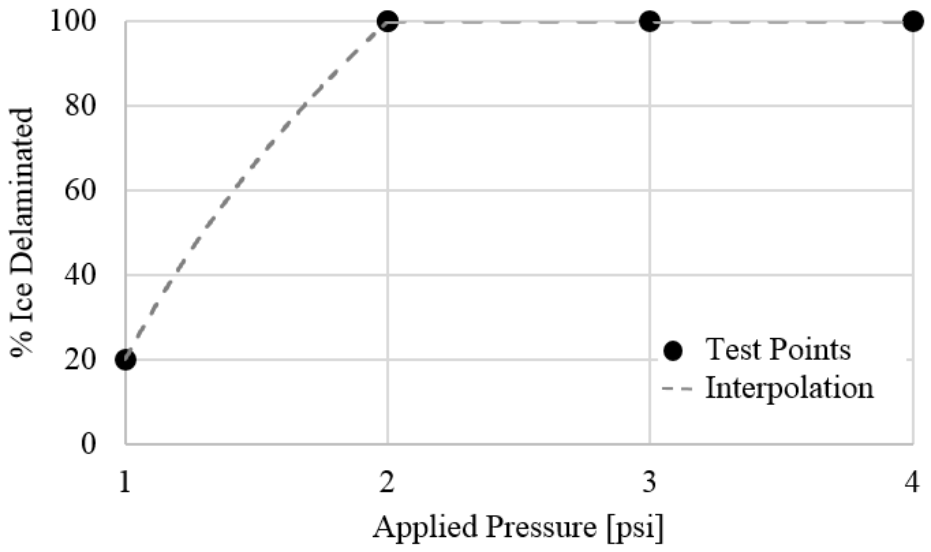

Figure 2.18: Dynamic Asymmetric Deformation Nodal Separation Comparison

2.4.5 Deformation Comparison

The three methods of deforming the plate, static, dynamic symmetric, and dynamic asymmetric, can be compared to see which method offers the largest nodal separation for a given pressure. The comparison of the nodal separation of the 1 psi and 2 psi cases are shown in Figure 2.19 and Figure 2.20 respectively.

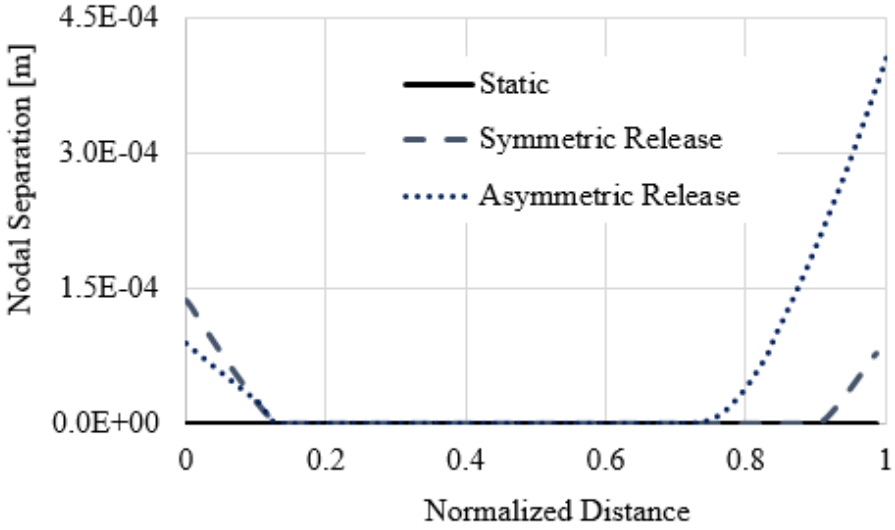

Figure 2.19: Deformation method Comparison - 1 psi

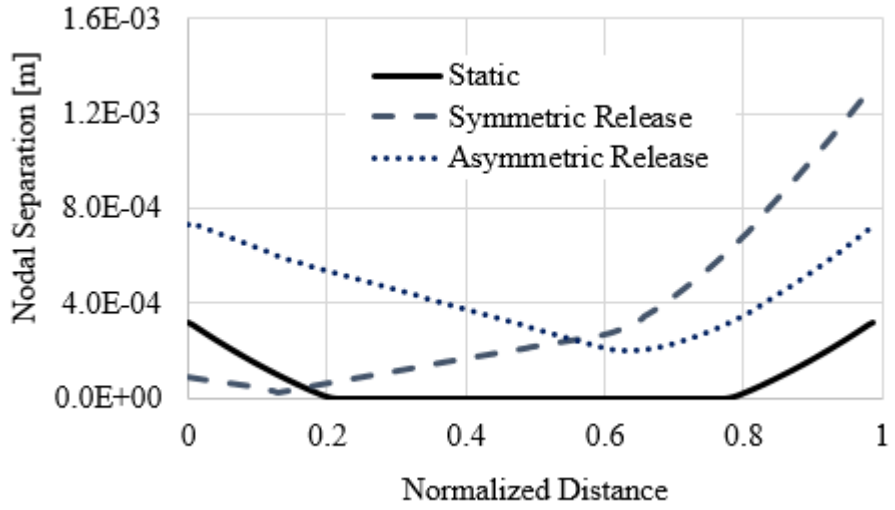

Figure 2.20: Deformation method Comparison - 2 psi

When 1 psi is applied to the system (Figure 2.19), in all cases most of the ice remains attached to the plate; although, one end on the asymmetric release is delaminated. Once the applied pressure is increased to 2 psi (Figure 2.20), most of the ice in the static deformation case remains attached while both dynamic deformation cases

are delaminated. At 2 psi, the symmetric and asymmetric cases are on the same order of magnitude, so their performance is similar. The comparison between the three deformation methods for 3 psi and 4 psi is shown in Figure 2.21 and Figure 2.22 respectively. As the pressure rises to 3 psi and 4 psi, the difference in nodal separation between the symmetric and asymmetric cases drastically increases. On average, the nodal separation of the asymmetric case is an order of magnitude greater than the symmetric case.

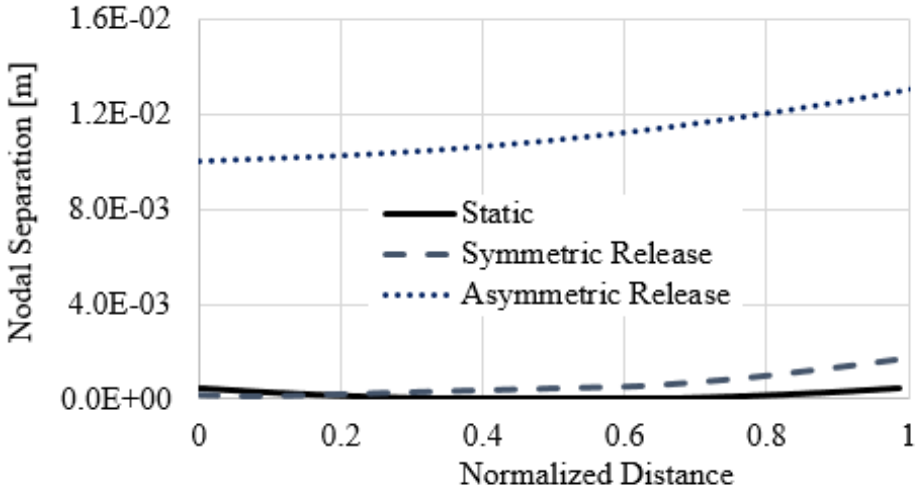

Figure 2.21: Deformation method Comparison - 3 psi

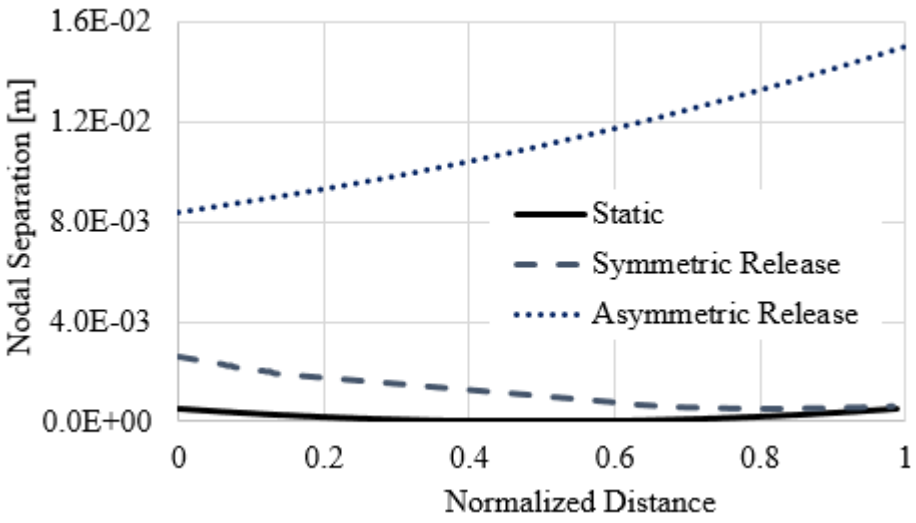

Figure 2.22: Deformation method Comparison - 4 psi

The performance of the asymmetric release outperforms both the symmetric release and the static deformation. This trend continues for the 4 psi case too. From the results presented in Figures 2.21 and 2.22, as the pressure applied to the plate increases, the asymmetric release method yields the best performance of the three cases. This trend can be seen in terms of the percent of ice delaminated (Figure 2.23). At all pressures, the percent ice delamination is greater for the dynamic cases. The dynamic asymmetric inflation technique is the first to completely delaminate.

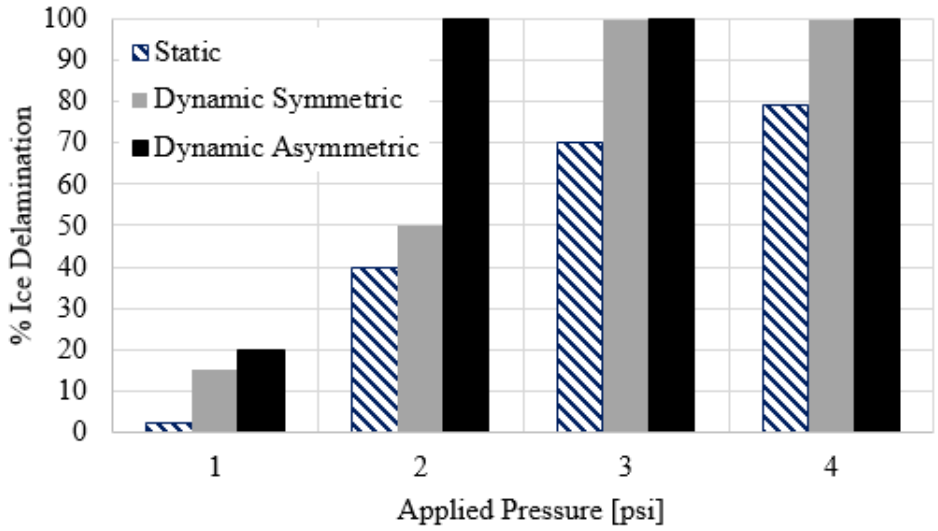

Figure 2.23: % Ice Delaminated Comparison

2.4.6 Asymmetric Release Comparison

In the case of an asymmetric release, the time between boundary condition releases can be controlled. A study can be performed to see how changing the time between releases impacts the final nodal separation. Five different release times are used for a given pressure and the nodal separation is recorded. The nodal separation for the five test cases at a pressure of 1 psi is shown in Figure 2.24.

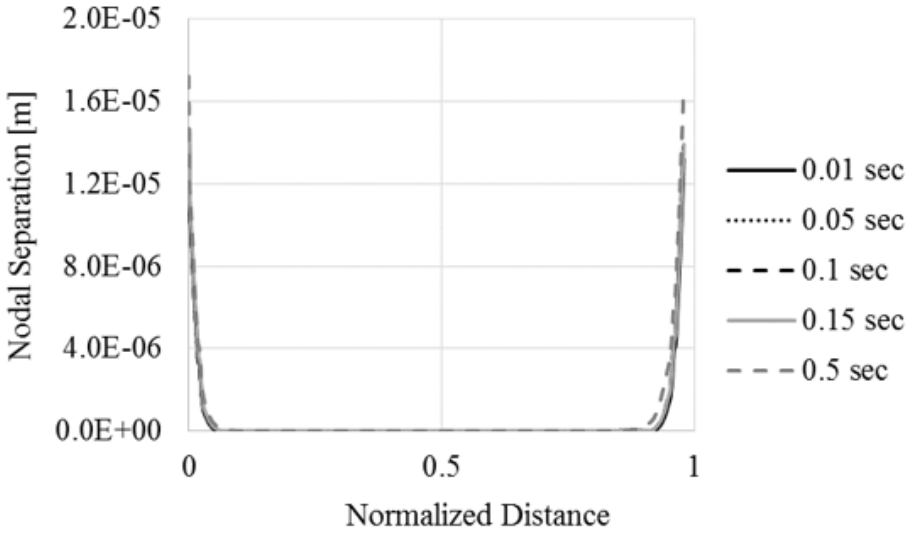

Figure 2.24: Nodal Separation with varying Propagation Times - 1 psi

For a pressure of 1 psi, the time between boundary conditions being released has a negligible effect on the final nodal separation. Although, as the pressure is increased, the dependence on time between boundary conditions released is more noticeable. How the final nodal separation changes with time between boundary conditions being released at 3 psi is presented in Figure 2.25.

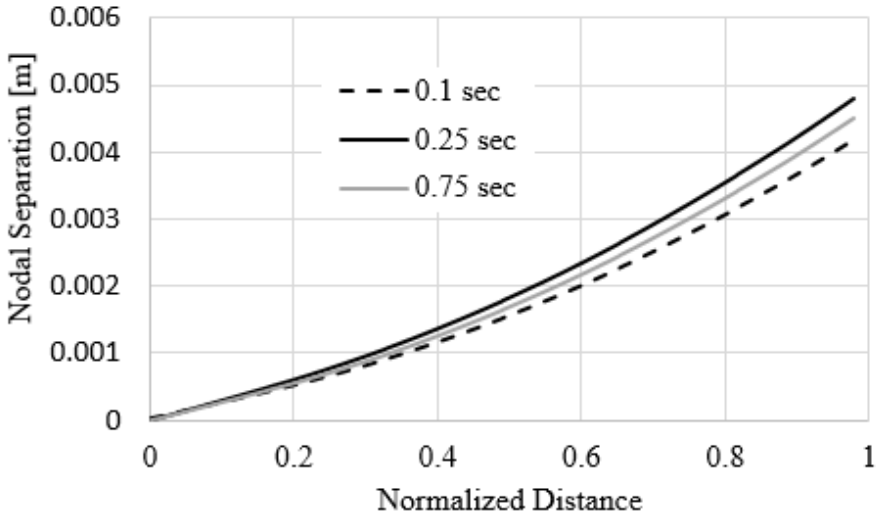

Figure 2.25: Nodal Separation with varying Propagation Times - 3 psi

At a larger pressure, there is a propagation time where the nodal separation reaches a maximum, and this occurs at approximately 0.25 sec. Therefore, during experiments and further Abaqus flat plate modeling, the time between boundary conditions being released will be 0.25 sec to maximize nodal separation.

Chapter 3

Flat Plate Impulsive-Pneumatic Experimental Evaluation

In this chapter, an experimental flat plate model is fabricated and tested following the results obtained in the parametric modeling of the system. The model implements an impulsive release system which takes advantage of the benefits of an asymmetric release as disused in Chapter 3. In this Chapter, the stainless steel cohesive surface modulus is experimentally determined by varying the Abaqus model values to match experimental results as required by the cohesive failure model.

3.1 Plate Configuration

A square flat plate model which implements a release system that constricts the plate movement results in impulsive behavior. This flat plate model is identical in dimensions to the Abaqus model constructed in Chapter 3. Unlike the Abaqus model, the physical model needs a base for the plate to be bonded to. To ensure

the base does not deform under load, a half inch Plexiglas boundary plate is used. The flat plate experimental layout with relevant dimensions and components is illustrated in Figure 3.1.

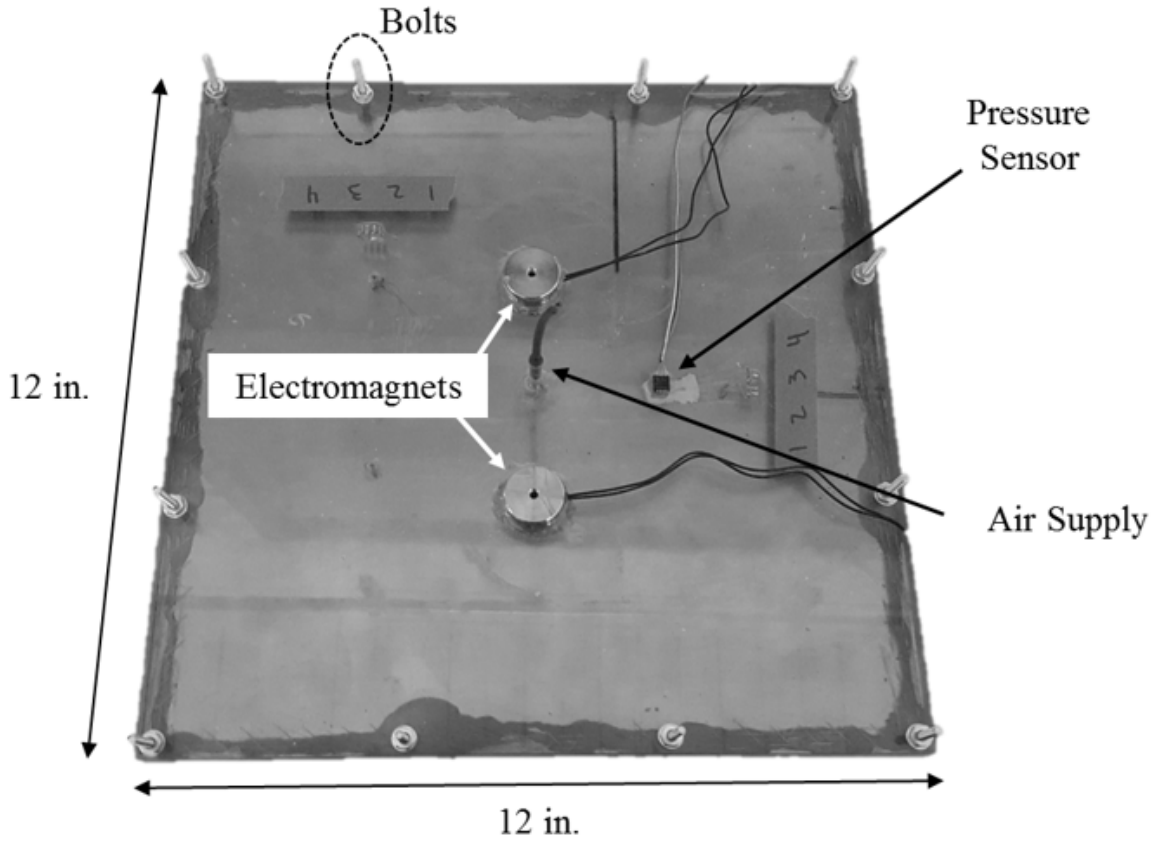

Figure 3.1: Plate Configuration

The outer half inch on each side can be seen to be epoxied and bolted which are used to simulate a clamped boundary condition. A side view of the plate with relevant dimensions is shown in Figure 3.2.

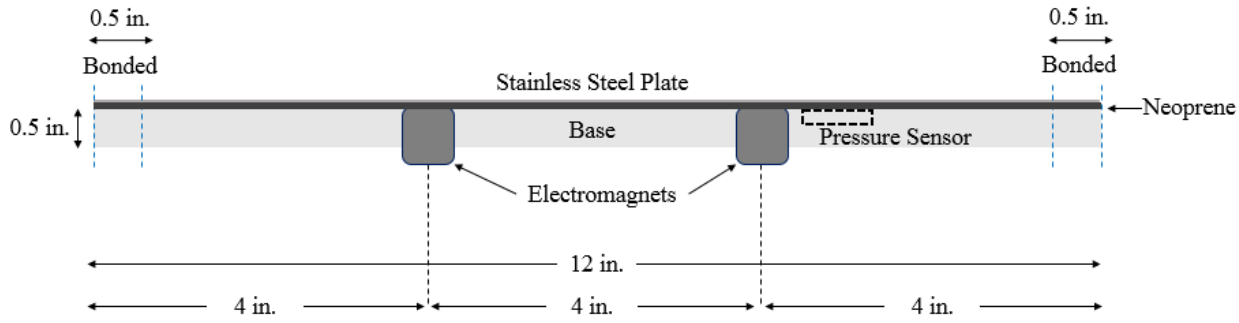

Figure 3.2: Plate Configuration - Side View

An additional modification that is made to best seal the plate is the use of a neoprene rubber sheet that covers the 0.5-in bonding region. The plate is a 400 series stainless steel with the same material properties listed in Table 2.1. The plate is constructed of a 400 series stainless steel due to its ferromagnetic properties; therefore, the electromagnets can be turned on to constrict the movement of the plate. The interface parameters for for the stainless steel are quantified in Section 3.2.2

3.1.1 Implementation of Neoprene Behavior in Abaqus

The addition of a neoprene rubber material to seal the plate must be accounted for in the Abaqus model to best represent the physical model. Hyperelastic material properties can be used to define the characteristics of a material in Abaqus. One way in which Abaqus defines the behavior of a hyperelastic material is through stress-strain data and fitting a hyperelastic model to the data. Ref. [5] experimentally constructed stress-strain plots for a neoprene rubber sample which is used in the flat plate model (Figure 3.3).

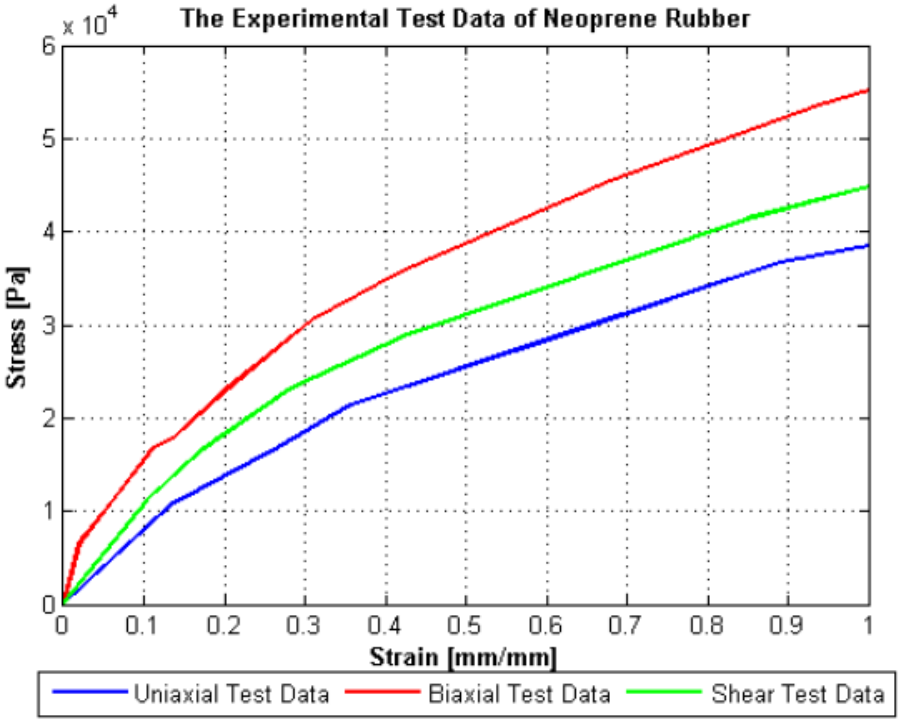

Figure 3.3: Stress-Strain Test Data for Neoprene Rubber [5]

The data from Figure 3.3 can be imported into Abaqus and used to model the behavior of the hyperelastic material. Abaqus offers many hyperelastic models to represent the behavior including: Arruda-Boyce, Mooney-Rivlin, Neo Hooke, Van der Waals, and Yeoh. A study was performed by Ref. [60] which compares experimental data to several different hyperelastic models. The results of this study are shown in Figure 3.4.

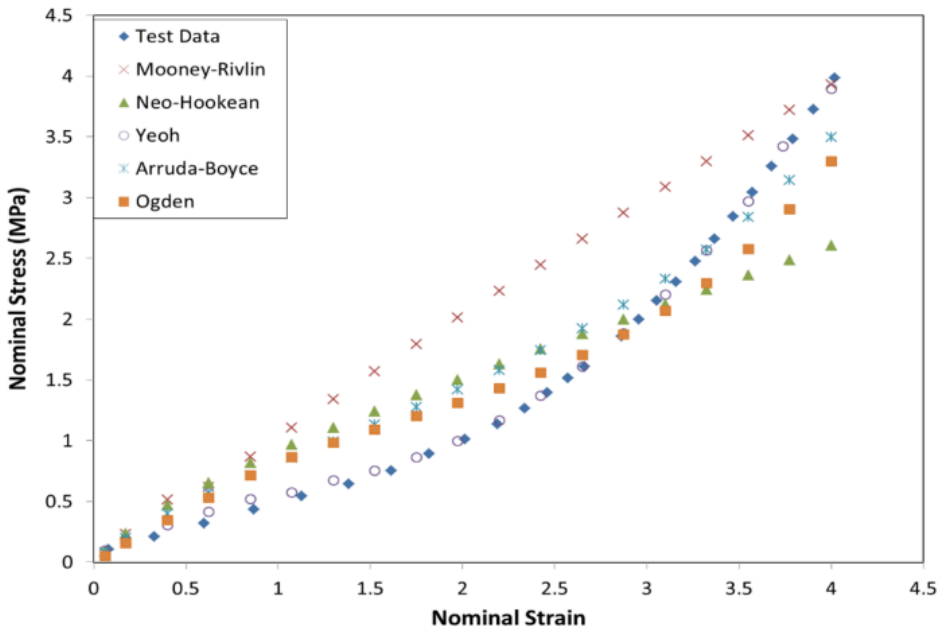

Figure 3.4: Comparisons of Hyperelastic Models under Uniaxial Loading [60]

Under uniaxial loading, the Yeoh method matches the test data best for a wide range of nominal strains; therefore, the Yeoh strain energy potential is used in the Abaqus model to define the behavior of the hyperelastic neoprene material. The Abaqus model with the addition of a hyperelastic material is shown in Figure 3.5. A notch on the top of the plate is used to simulate bolts that constrain the motion of the plate along the outer edge.

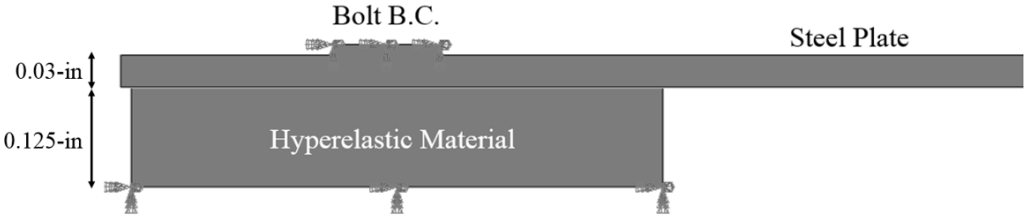

Figure 3.5: Hyperelastic Neoprene Material Implemtation in Abaqus

3.2 Experiential Results and Abaqus FEA Comparison

The Abaqus FEA model can be verified by comparing simulation results to experiential data. First, a test is performed to compare the plate deflection without ice to ensure stress-strain laws hold between the flat plate and Abaqus model. Abaqus predicts the center deflection of the plate for varying pressures and are compared to experimental results. Experimental ice delamination tests are used to determine a stainless steel cohesive surface modulus in the Abaqus model.

3.2.1 Plate Deflection

The FEA model constructed in Abaqus can be compared to the flat plate experimental results. One method of comparing Abaqus and experimental results is through plate deformation. In Abaqus, when applying a pressure to the plate, the displacement of individual nodes can be tracked. The displacement of sections of the physical model can too be tracked using a linear variable differential transformer (LVDT). The experimental configuration to record the plate displacement is shown in Figure 3.6.

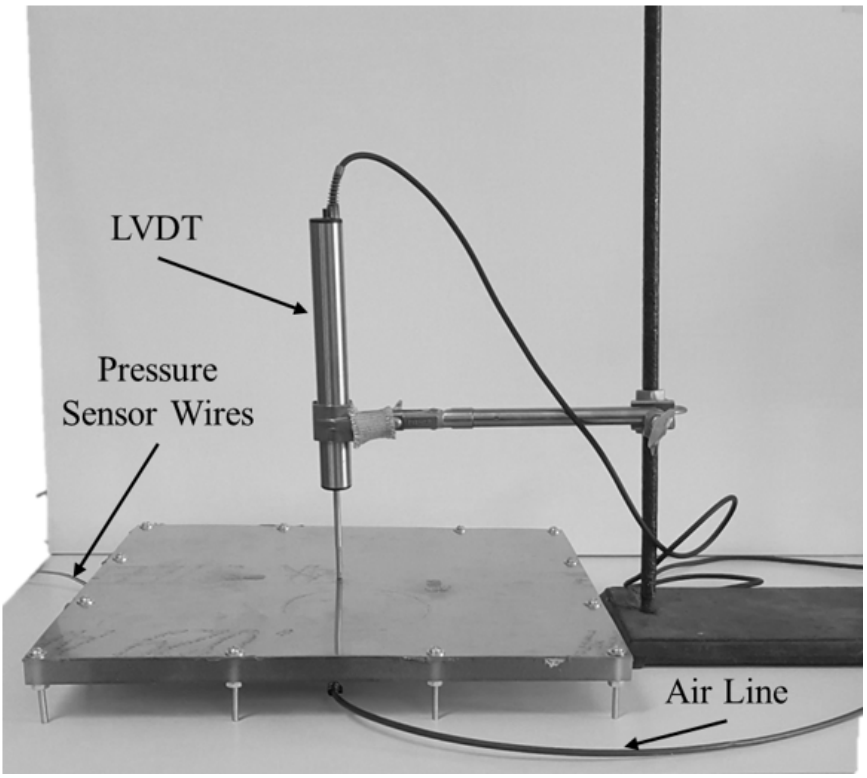

Figure 3.6: Experimental Layout to Record Plate Deformation

Other instruments used that are used are an air compressor, power supply, air regulator, and LabView data acquisition module. Labview records the LVDT and pressure sensor values at the same rate so that pressure and displacement readings are at the same time. The tip of the LVDT is centered on the plate and is calibrated using three known points. The regulator is steadily opened to allow the pressure in the model to linearly increase which deforms the plate. The displacement of the center of the plate when pressure is applied for both the Abaqus and experimental model up to 3 psi is shown in Figure 3.7.

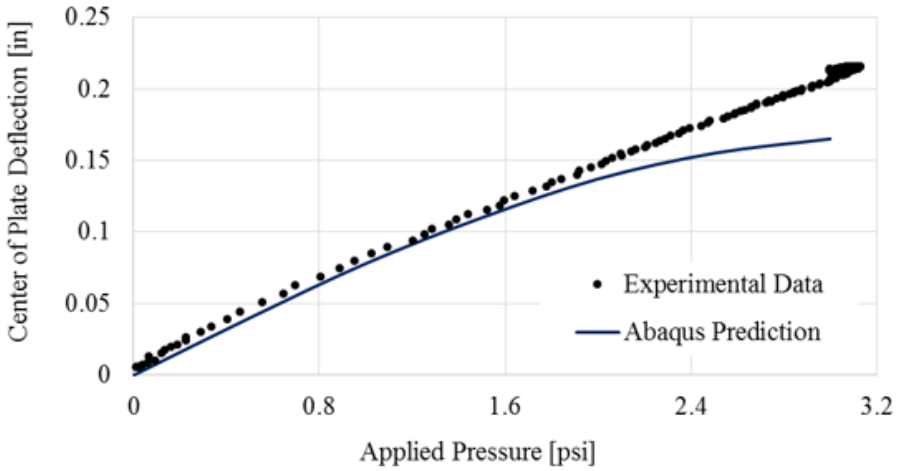

Figure 3.7: Center of Plate Deflection vs. Applied Pressure

For applied pressures less than 1.8 psi, the percent difference between Abaqus results and experimental data is no greater than 2%. After 1.8 psi, the results from Abaqus and experimental data begin to slightly diverge. The difference can most likely be explained by the experimental model not possessing perfect boundary conditions like the Abaqus model has. As the pressure is increased, the Abaqus model predicts more asymptomatic behavior. The dynamic behavior of the Abaqus model and the experimental model are also compared (Figure 3.8). At 0.31 sec, the electromagnets are deactivated allowing the plate to dynamically respond.

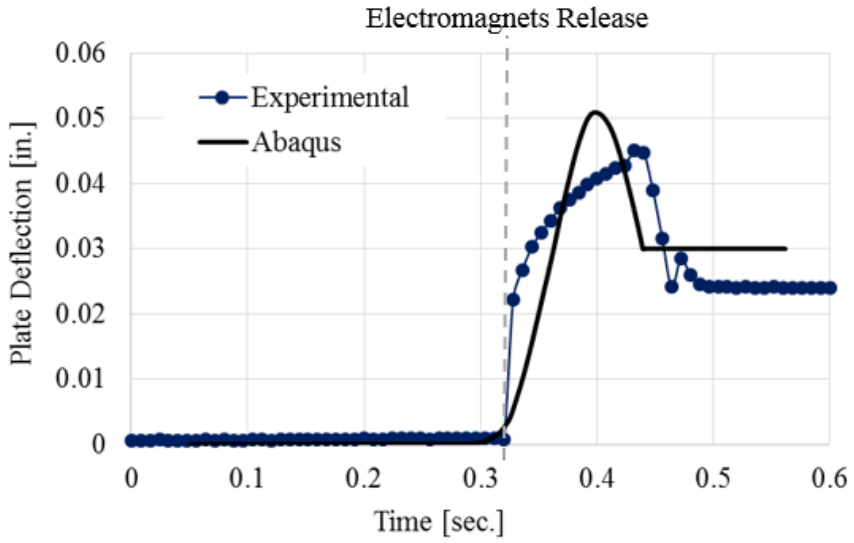

Figure 3.8: Abaqus and Experimental Center of Plate Deflection with Release at 0.25 psi

Overall, the dynamic behavior of the Abaqus model and the experimental model follow the same trends. Abaqus predicts a greater plate deflection than what the experiments yield. This difference can be explained by the pressure drop measured by the pressure sensor (Figure 3.9). The sudden pressure drop seen in the experiment is caused by the expanding volume once the electromagnets are deactivated. In the Abaqus model, the pressure remains constant; therefore, the plate deflection is expected to be greater than experimental results.

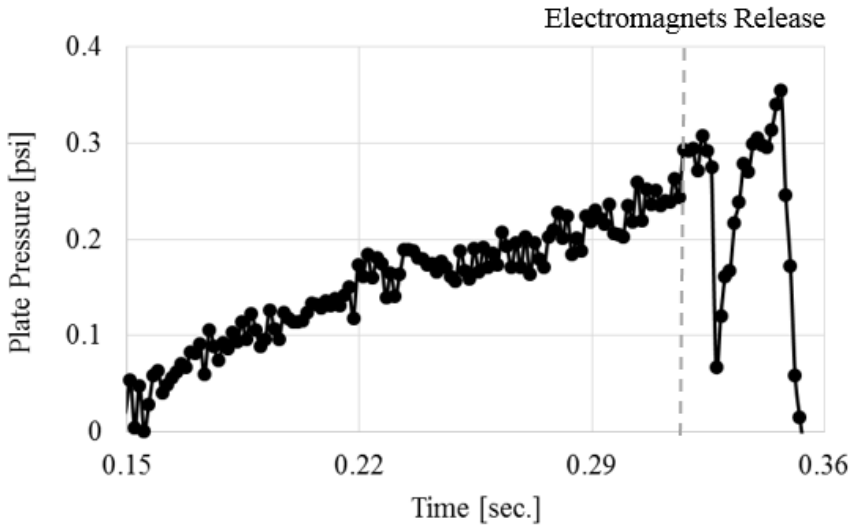

Figure 3.9: Plate Pressure with Release at 0.25 psi

Since the pressure quickly drops in the experiment, the maximum plate deflection will be less than that predicted by the Abaqus model.

3.2.2 Ice Delamination

The de-icing performance of the experimental model can too be compared to the Abaqus model. The process of comparing the results is straight forward. First, multiple simulations are run in the Abaqus model where in each successive job, the applied pressure is gradually increased. The pressure continues to increase until the smallest nodal separation is greater than 6.88 μm, which is the cohesive failure separation calculated using Equation 2.14. Once all values of nodal separation surpass 6.88 μm, the ice is said to be completely delaminated.

The performance of the experimental model is quantified in a similar process. A starting pressure is chosen and applied to the plate using the air compressor and regulator. Once the desired pressure is achieved, a LabView program turns off the

first electromagnet, waits the optimal time (0.25 sec), and then turns off the second electromagnet. If the ice remains attached to the plate, the test is repeated with an increased applied pressure. The two applied pressures from the Abaqus model and the experimental model can then be compared. The temperature is kept at -10°C by the addition of a controller which uses a thermocouple at the level of the flat plate system (Figure 3.10).

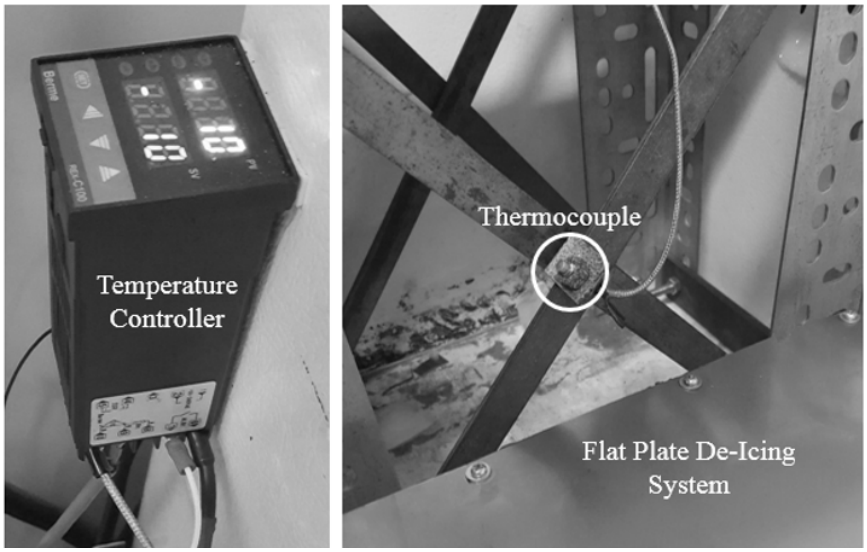

Figure 3.10: Experimental Configuration of the Ice Delamination Test

The experimental setup to quantify the deicing performance is illustrated in Figure 3.11.

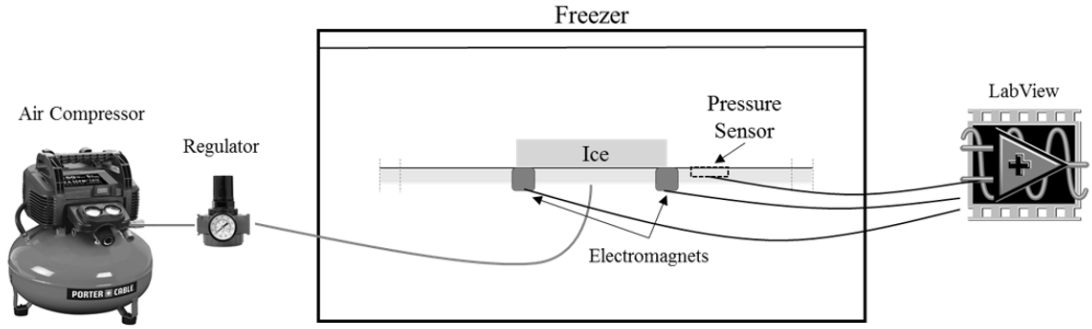

Figure 3.11: Experimental Configuration of the Ice Delamination Test

The ice that is used in the experiment is made in the freezer from distilled water on the center of the plate. The plate can cool to -10°C, and then water is poured into a mold and then freezes. This ensures that the ice/plate interface is formed at -10°C. The mold, with dimensions, for creating the freezer ice is shown in Figure 3.12. The thickness of the freezer ice is dictated by the amount of layers of tape that make up the border. This strip of ice sits between the two electromagnets.

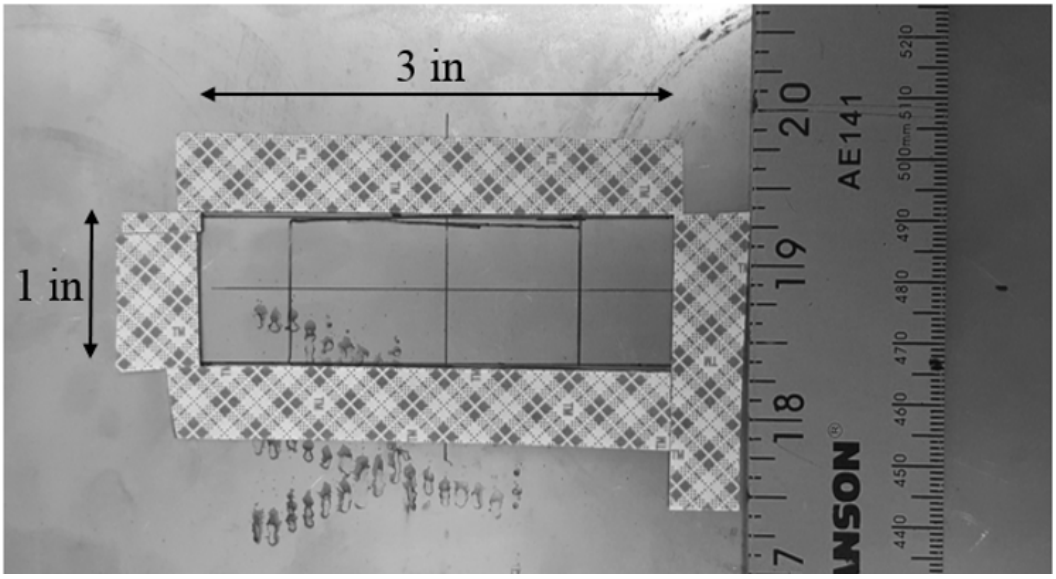

Figure 3.12: Mold to create Freezer Ice

To ensure that the experimental results can be reproduced, a procedural list to conduct the tests is implemented. The steps for conducting the ice delamination experiment are listed in Table 3.1.

Table 3.1: Steps to Conduct Ice Delamination Experiments

Step	Description
1	Allow plate to reach thermal equilibrium at -10°C
2	Place tape to form water barrier
3	Allow system to again reach thermal equilibrium
4	Add distilled water to the ice mold
5	Allow water to freeze throughout & remove tape
6	Use regulator to acquire the desired pressure
7	Use LabView program to release the electromagnets
8	Remove ice remnants if any
9	Adjust applied pressure and repeat until delamination

A case where the thickness of the ice was two layers of tape thick (0.3 in.) was preformed. Based on the FEA model, to completely delaminate the accreted ice, a pressure between 0.26 and 0.27 psi is needed. The corresponding nodal separation for the symmetric inflation case is shown in Figure 3.13.

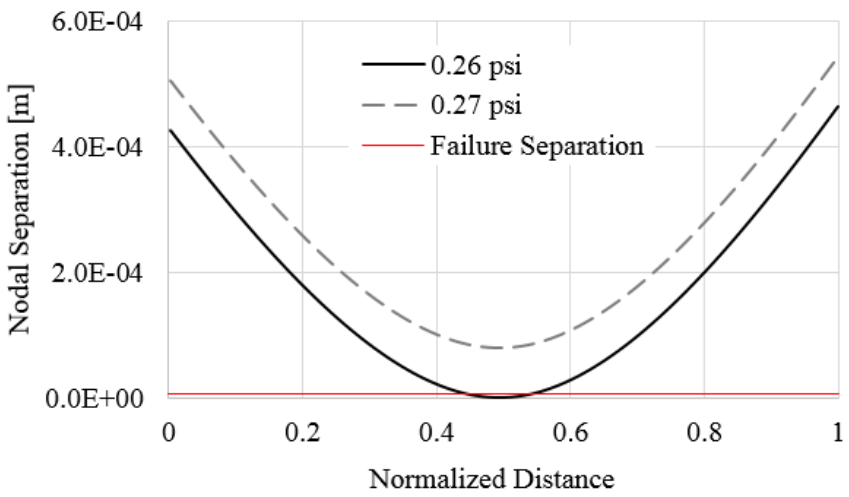

Figure 3.13: Abaqus Symmetric Inflation - 0.3-in thick Ice Nodal Separation vs. Pressure

Using the steps listed in Table 3.1, it was experimentally determined that an applied pressure of 0.43 psi is required for complete delamination to occur. This is a percent difference of 45.7% between experimental results and modeling predictions. The process of comparing predicted Abaqus results and experimental results can be repeated for varying ice thicknesses. The predicted Abaqus delamination pressure and the average experimental results with the associated error bars for symmetric releases are shown in Figure 3.14.

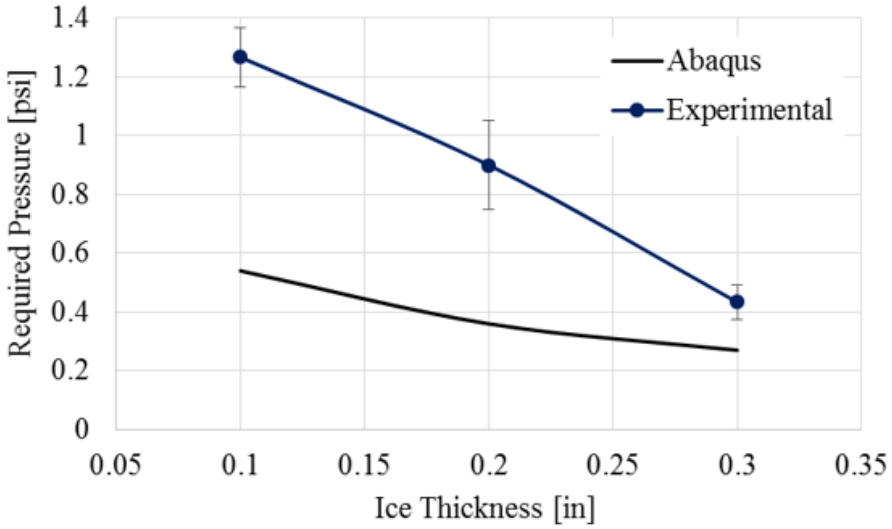

Figure 3.14: Abaqus and Experimental Delamination Results - Symmetric Release

As the ice thickness increases, the difference between the Abaqus and experimental pressure required to delaminate the ice decreases. One possible reason for the discrepancy at smaller thicknesses is the ice is too thin. As described in Section 1.4.2, if the ice accreted to the pneumatic boot is too thin, the ice will crack, but will remain attached forming a flexible layer of ice.

The same comparison can be made for the asymmetric release scenario. The predicted Abaqus delamination pressure and the average experimental results with the associated error bars for asymmetric releases are shown in Figure 3.15.

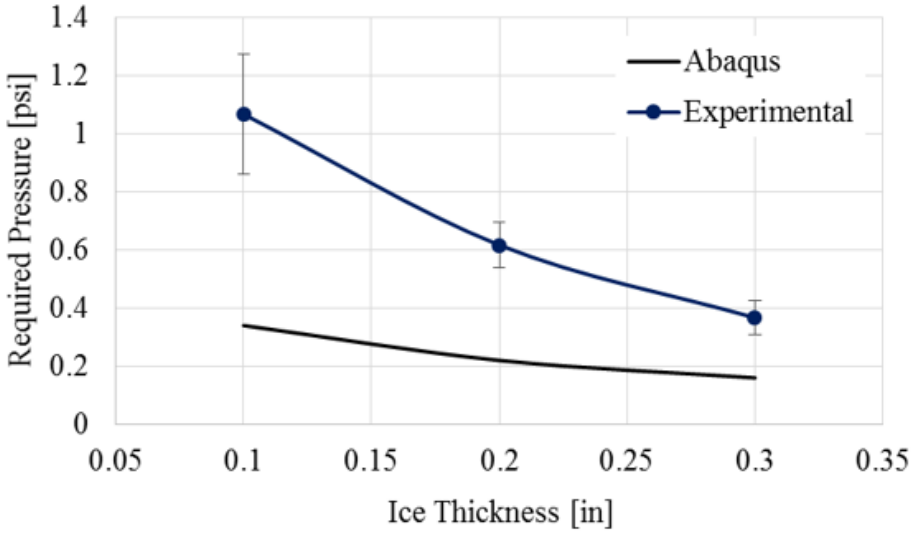

Figure 3.15: Abaqus and Experimental Delamination Results - Asymmetric Release

In both the symmetric and asymmetric inflation cases, the Abaqus model and Experimental results follow the same trend in that as the ice thickness increases the pressure required decreases. As the ice thickness increased, the shear stresses along the ice/plate interface too increased. As expected, the Abaqus model under predicts the pressure required to delaminate the ice. This implies that the cohesive surface modulus used is less than that of stainless steel. As presented in Ref. [61], the ice adhesion strength of stainless steel is larger than aluminum; therefore, the cohesive surface modulus of stainless steel is expected to be greater than that of aluminum.

To find the cohesive surface modulus of the stainless steel, an ice thickness is chosen and the Abaqus and Experimental results are matched by varying the surface modulus. In this symmetric inflation case, 0.2-in is chosen since it sits in the middle of the ice thickness range. For the symmetric case, at an ice thickness of 0.2-in, the experimentally determined required pressure is 0.9 psi. The applied

pressure in the Abaqus model is then held constant while the cohesive surface modulus is varied. The cohesive surface modulus is started at 1.0 x $10^{12} Nm^{-3}$ (value determined by Ref. [11]) and increased until a portion of the ice remains attached to the plate through the entire inflation period. The minimum nodal separation which quantifies delaminated is 6.88 μm, which was is indicated by the horizontal line in Figure 3.16. The cohesive failure distance (6.88 μm) was calculated using Equation 2.8.

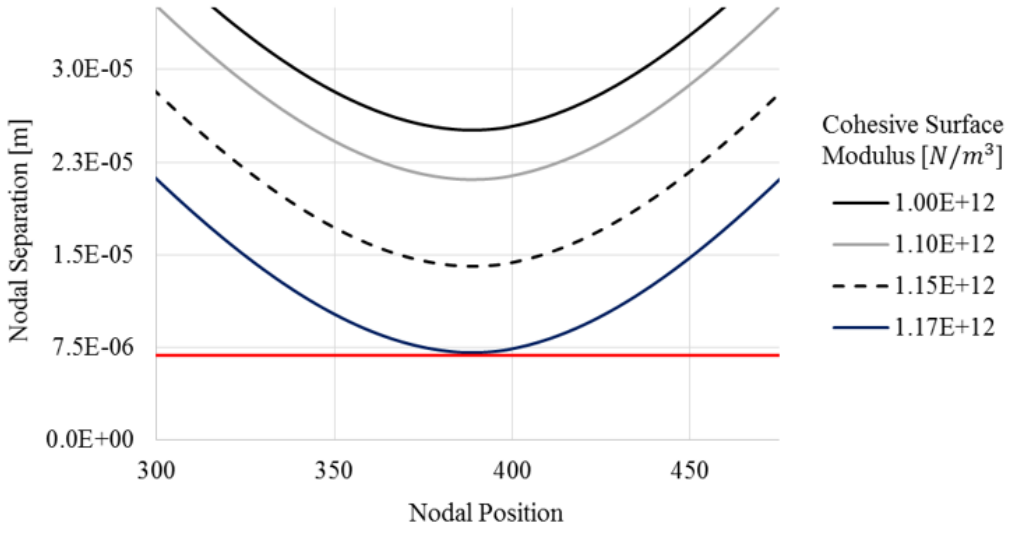

Figure 3.16: Cohesive Surface Modulus effect on Nodal Separation

Therefore, the cohesive surface modulus that is to be used for 410 stainless steel is 1.17x$10^{12} N/m^3$. This is an increase of 17% compared to the experimentally determined value for aluminum. This new value for the cohesive surface modulus is used going forward for the airfoil Abaqus model.

Once the new value for the cohesive surface modulus is implemented into the Abaqus flat plate model, the results tend to match better. The symmetric and asymmetric pressure required to delaminate using the new cohesive surface modulus

are shown in Figure 3.17 and Figure 3.18 respectively.

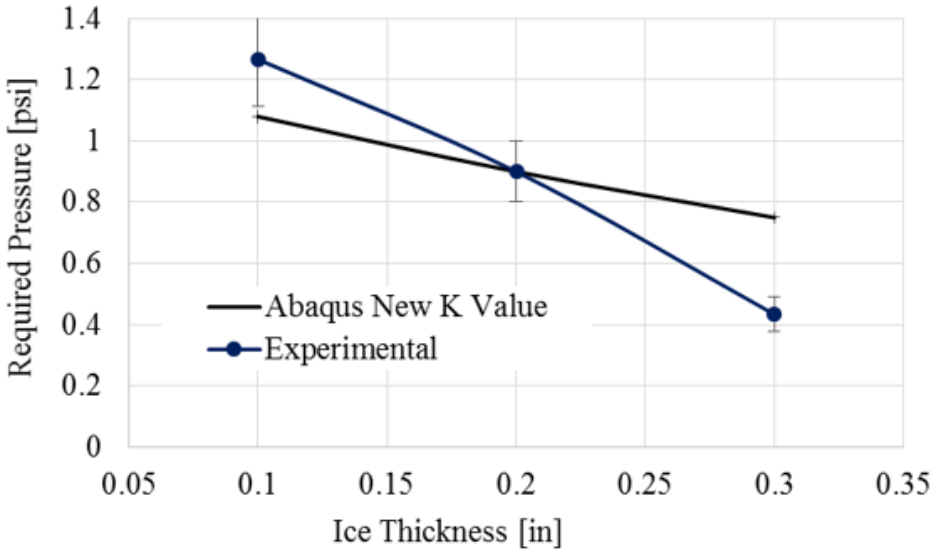

Figure 3.17: Updated Cohesive Surface Modulus Delamination Results - Symmetric

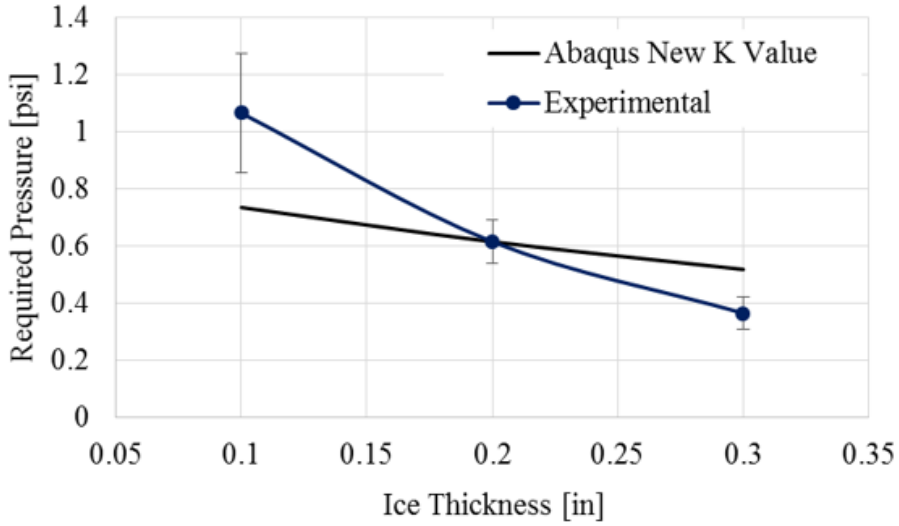

Figure 3.18: Updated Cohesive Surface Modulus Delamination Results - Asymmetric

After running the Abaqus flat plate model using the updated cohesive surface modulus, the Abaqus and Experimental results are better aligned. Effectively, the Abaqus results are shifted upwards until the pressures required for 0.2-in ice

thickness match. Now the Abaqus model tends to under-predict the required pressure at small ice thicknesses and over-predicts at larger ice thicknesses. A summary of the percent difference between the experimental results and FEA model predictions for both the old cohesive surface modulus and the adjusted cohesive surface modulus is shown in Figure 3.19.

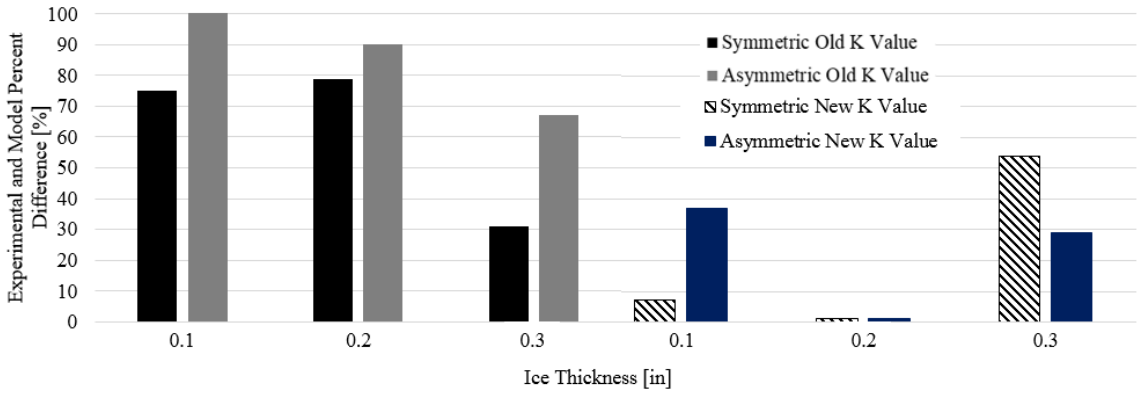

Figure 3.19: Summary of Percent Difference between Experimental Results and Model Predictions

Chapter 4

Development of an Airfoil Abaqus FEA Model

Similar to the flat plate model, an airfoil shape with attached ice can be constructed in Abaqus. Yet again, a mesh convergence study for both stress-strain and traction-separation relationships have to be conducted to ensure accurate results. Portions of the airfoil shell can be constrained and released to achieve the impulsive effects.

4.1 Airfoil Model Overview

The flat plate model created in Chapter 2 can take the shape of an airfoil, specifically a slightly modified NACA 0024. A NACA 0024 airfoil must be slightly modified to fit in the AERTS icing tunnel test section. The Abaqus FEA model with significant components labeled is illustrated in Figure 4.1. The connections are made of the same hyperelastic neoprene material used to seal the bonding area of the flat plate model. The gap between the shell and airfoil allows the leading edge of the shell to

move closer to the airfoil resulting in the sides of the shell to deform outwards. This deformation creates the necessary transverse shear stress to delaminate accreted ice.

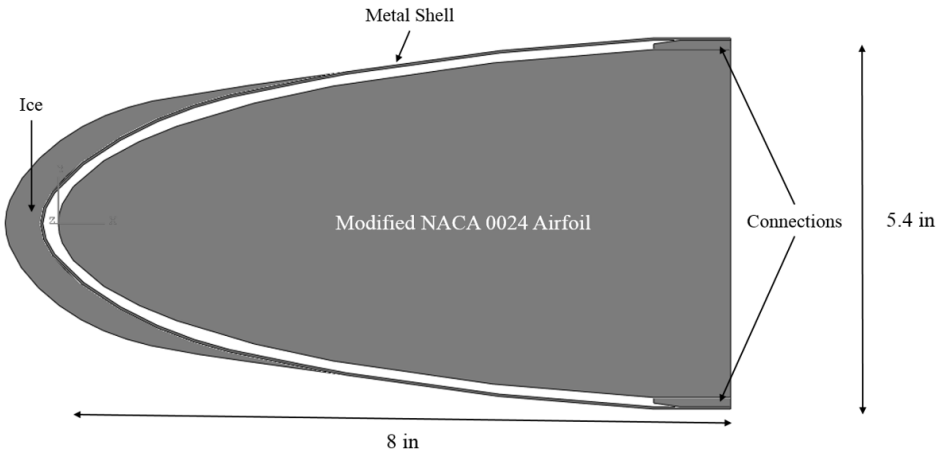

Figure 4.1: Abaqus Airfoil Model Layout

Pressure is applied in the shell/airfoil gap on the inner surface of the metal shell. Two locations on the metal shell can be constrained and released which introduces impulsive effects. The specific location that these boundary conditions exist are at the points of maximum deflection on the upper and lower portions of the shell. The constrains are at maximum deflection points because those are the points of maximum stress. Where the pressure is applied and the location of the boundary conditions is shown in Figure 4.2.

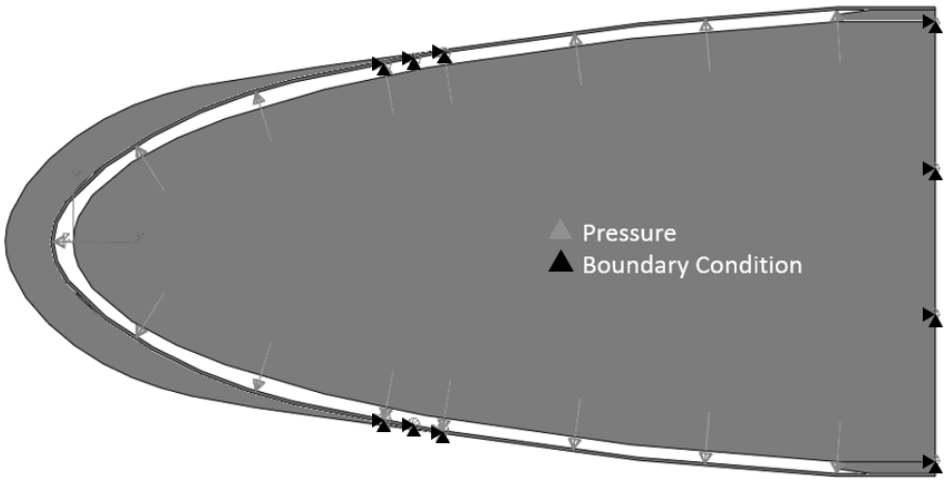

Figure 4.2: Abaqus Airfoil Model with Pressure and Boundary Conditions

The first step, like the flat plate model, is a general static step where all three boundary conditions are in place which constrains portions of the metal shell. Once the implicit dynamic step begins the shell boundary conditions can be disabled symmetrically or asymmetrically.

4.2 Mesh Convergence Studies

The following section presents the two mesh convergence studies conducted on the modified NACA 0024 Abaqus airfoil model, stress-strain & traction-separation.

4.2.1 Stress-Strain Mesh Convergence Study

Using the airfoil model described in Section 4.1 negating the leading-edge ice, the displacement of a unique node can be tracked. The mesh element size is continuously decreased until the displacement ceases to chance by 5%. The stress-strain mesh convergence study is summarized in Figure 4.3.

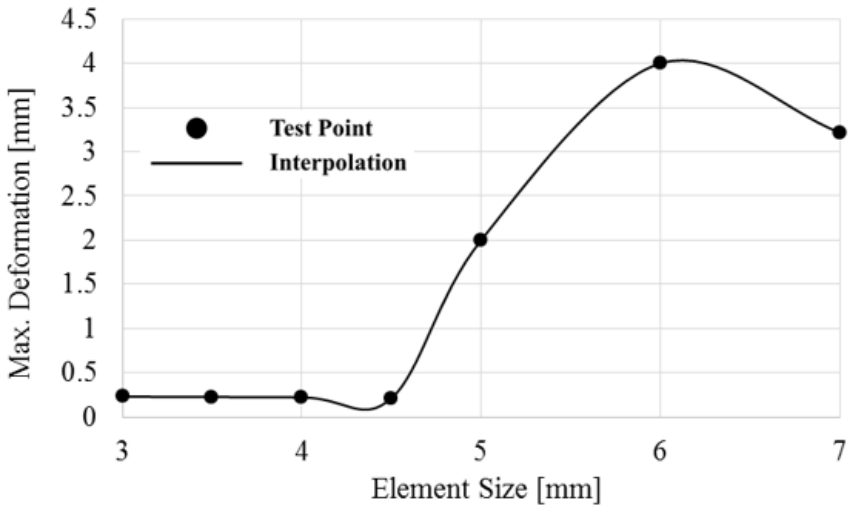

Figure 4.3: Stress-Strain Mesh Convergence

From a stress-strain relationship standpoint, the mesh element size that yields accurate results while reducing the computational cost is approximately 4.5 mm.

4.2.2 Traction-Separation Mesh Convergence Study

In addition to the stress-strain relationship mesh convergence, additional meshing must be considered with respect to traction-separation relationships. The airfoil model constructed in Abaqus has the same dimensions and ice/shell interface as those in Ref. [2]; therefore, has the same mesh element sizes shown in Table 4.1. Ref. [11] preformed calibrations to determine the required element size to accurately model the complex cohesive behavior. The calibration takes experimental results for all modes of failure and then iteratively changes the element size until the Abaqus model matches the results. The experimental results come from a peeling test for Mode I failure and lap-joint tests for Mode II and III failure. The required size of the elements due to the cohesive behavior are significantly smaller than the

size required for a traditional stress-strain mesh convergence study.

Table 4.1: Meshing Size for Cohesive Configuration [11]

Part	**Element Length**
Ice	0.86 mm
Plate	0.25 mm

The sizing presented in Table 4.1 will work since both are smaller than that required by the stress-strain relationships. The mesh sizing from the traction-separation relationship will not be as efficient from a computational perspective. Like the flat plate model, to improve the stability of the simulation approaching an equilibrium solution, a small viscosity coefficient will be used.

4.3 Shell Inflation Techniques

Like the flat plate model, three techniques can be used to create transverse shear stresses: static inflation, dynamic inflation with both boundary conditions releasing symmetrically, and dynamic inflation with boundary conditions releasing asymmetrically. The location of the boundary conditions are placed where the maximum shell deflection occurs since stress is proportional to curvature. The shell resting and deformed states are illustrated in Figure 4.4. The boundary conditions and electromagnets are placed at the highlighted points of maximum shell deflection.

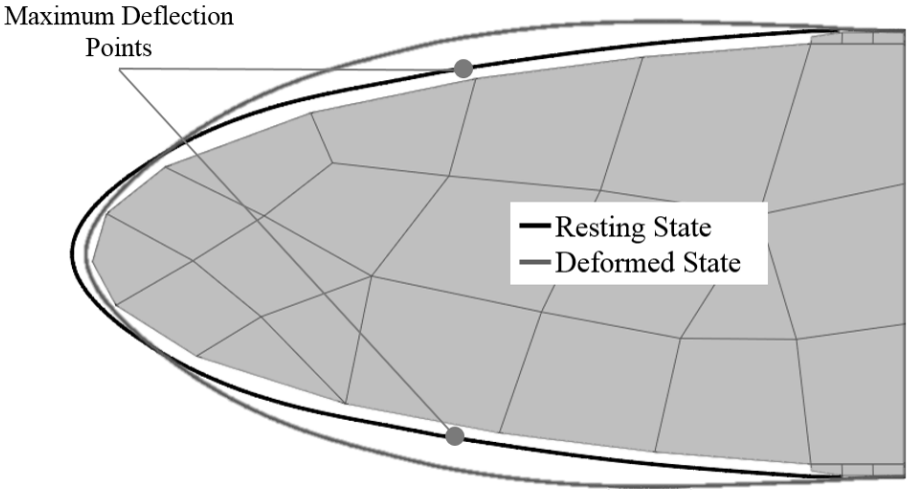

Figure 4.4: Shell Maximum Deflection Locations

Similar to the flat plate model, the nodal separation between the ice and shell can be compared to analyze the inflation technique's delamination performance. The nodal separation is plotted against the nondimensional path along the ice/shell interface (Figure 4.5).

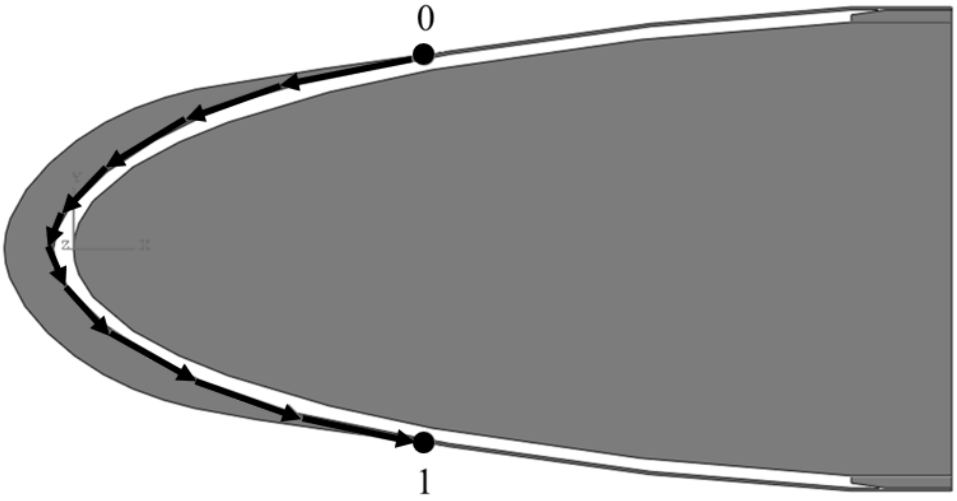

Figure 4.5: Nondimensional Path along Ice/Shell Interface

The nodal separation of the three inflation techniques are compared to analyze

the effectiveness of each. The nodal separation for all three inflation types at a pressure of 2 psi with the same step progression outlined in Section 2.2.1 is shown in Figure 4.6.

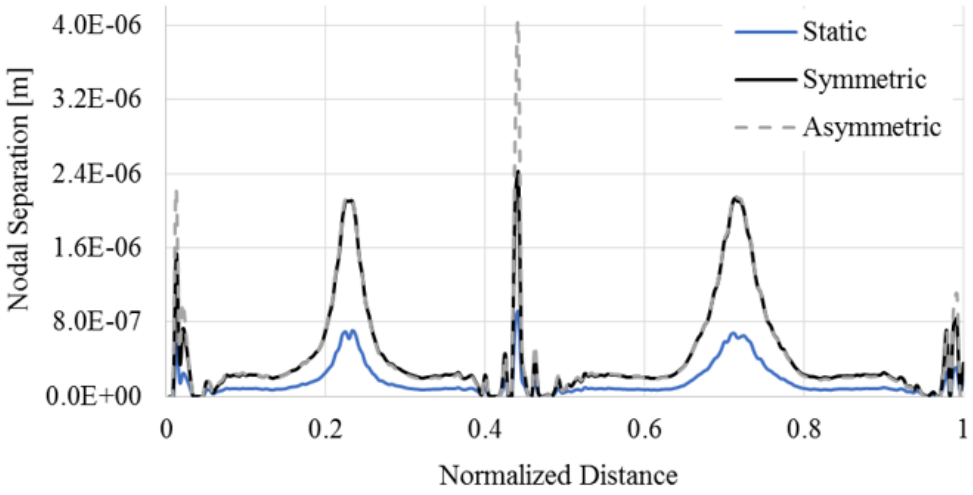

Figure 4.6: Inflation Types Comparison - 2 psi

The general static inflation generates less nodal separation on all points on the ice/shell interface than the dynamic inflation cases. The symmetric and asymmetric inflation are shown in Figure 4.7 to better illustrate the differences. The differences, circled in red, occur at the leading edge and the ends of the ice/shell bond interface. Other segments on the ice/shell interface show similar nodal separations for the asymmetric and symmetric cases.

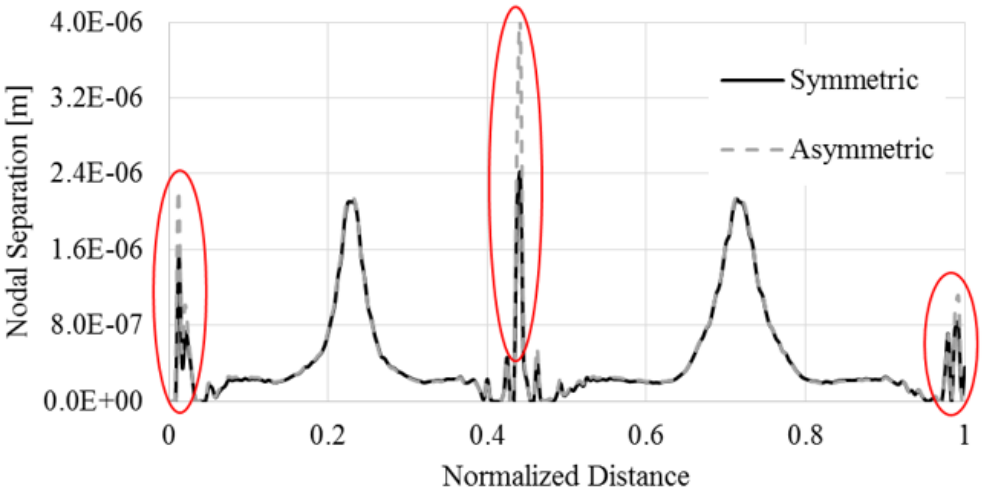

Figure 4.7: Nodal Separation Comparing Dynamic Inflation Cases - 2 psi

Similar to the flat model, the asymmetric release of the boundary conditions yields greater nodal separation than the symmetric case. Again, the time between the release of the top and bottom boundary conditions can be controlled and optimized to yield the greatest nodal displacement. The nodal separation for three different propagation times when an asymmetric inflation technique is used is shown in Figure 4.8. There is little difference between the three cases, but the 0.16 sec case does provide the greatest nodal separation and will be used when comparing the Abaqus model to experimental results.

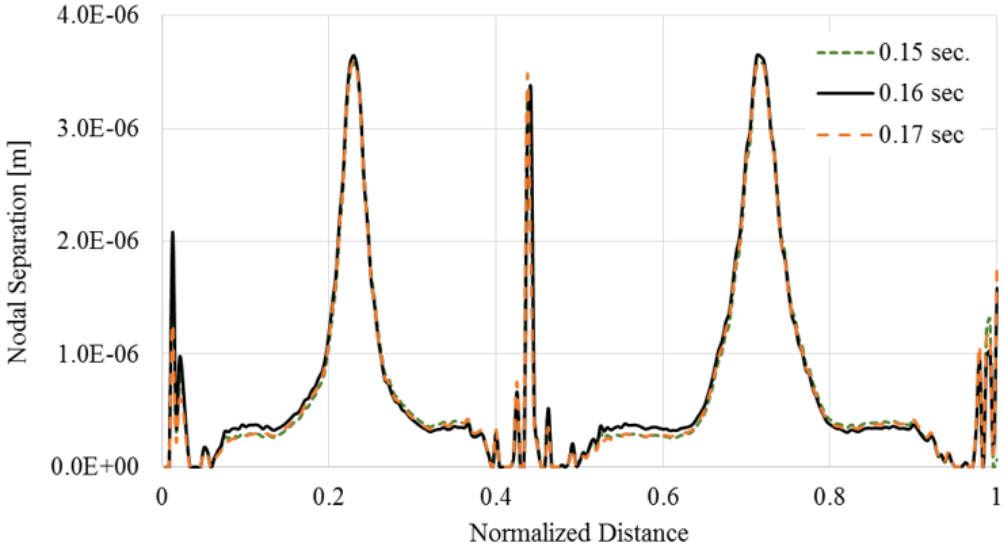

Figure 4.8: Comparison of Asymmetric Boundary Condition Release Times - 2 psi

There is also no dependency on which boundary condition releases first (top or bottom). This can be seen in Figure 4.9 where the two plots of nodal separation lay on top of each other which is expected since the NACA 0024 airfoil shape is non-cambered and symmetric.

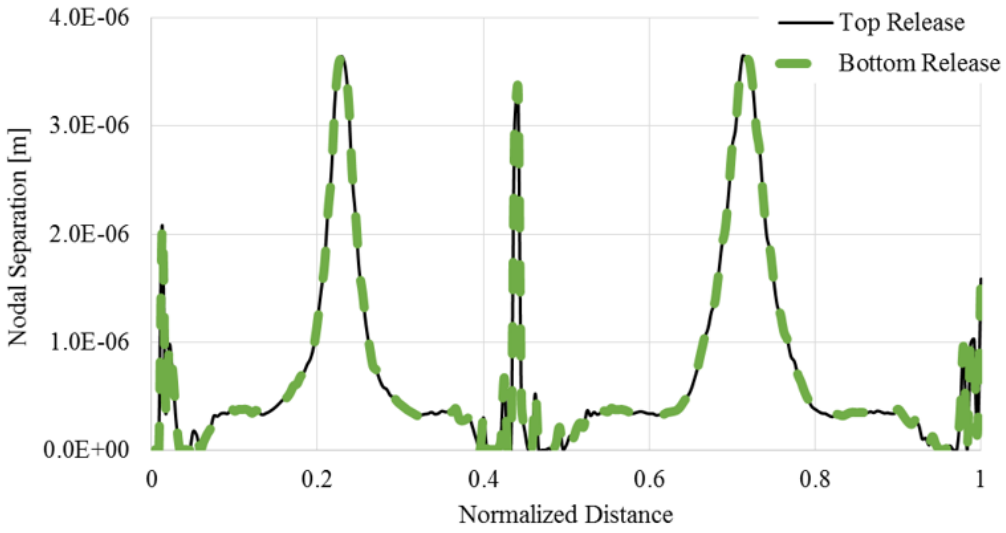

Figure 4.9: Top vs. Bottom Boundary Condition Release - 2 psi

4.4 Abaqus Model Dynamic Pressure Correction

When analyzing the Abaqus model, the only applied pressure comes between the airfoil and the metal shell. During wind tunnel testing, pressure will also be exerted on the metal shell due to the flow. This additional pressure is represented by

$$P = \frac{1}{2}\rho v^2 C_p \tag{4.1}$$

The pressure coefficient can be found using XFOIL and is shown in Figure 4.10 for three different angles of attack. The conditions at which the Reynolds number is found at 40 m/s and the air density and dynamic viscosity corresponding to -10°C, which represent the testing conditions expected in the AERTS icing tunnel.

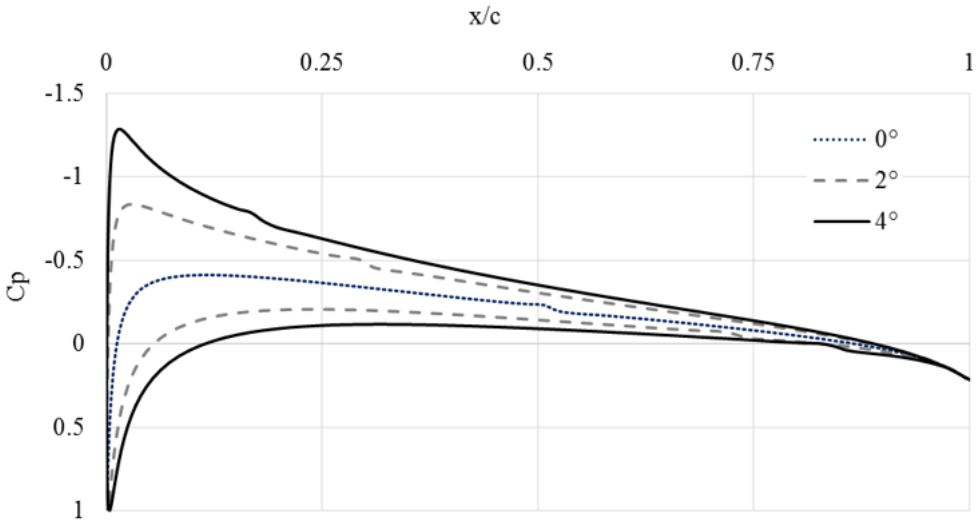

Figure 4.10: NACA 0024 Pressure Coefficient Distribution - Re ≈ 3.9e6

Abaqus allows for a user defined loading; therefore, the pressure coefficient distribution can be mapped to the shell in the Abaqus model as shown in Figure 4.11.

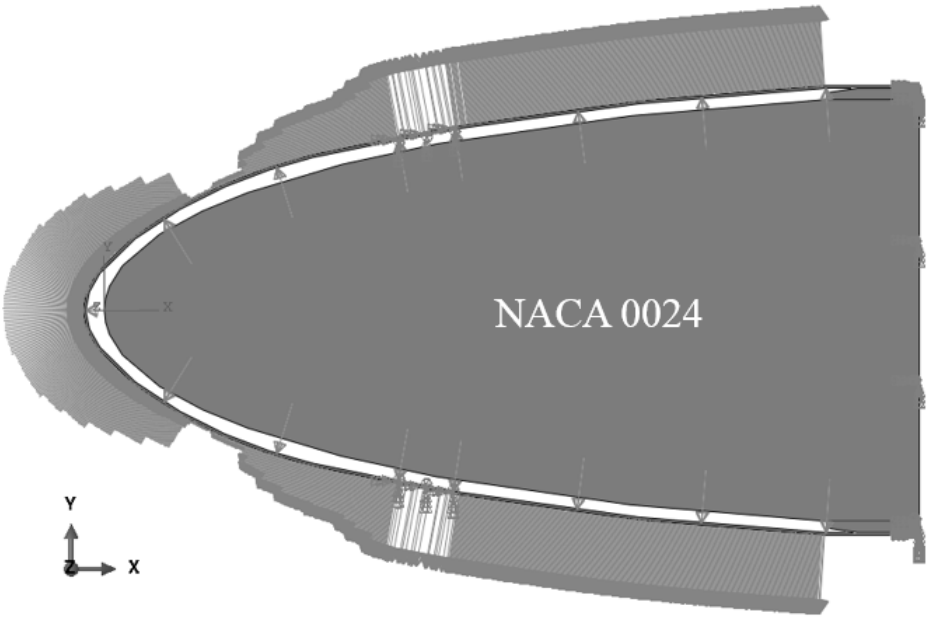

Figure 4.11: Dynamic Pressure Distribution over Shell - 0° AOA

At 0° AOA, the additional pressure distribution acts in a way which assists the preferred deformation, but at nonzero AOA, the aerodynamic pressure can inhibit inflation requiring additional pressure to delaminate the accreted ice.

Chapter 5

Airfoil De-Icing System Icing Tunnel Testing

In this chapter, the impulsive-pneumatic de-icing system from the flat plate model is implemented on an airfoil structure, specifically a NACA 0024. The Abaqus model described in Chapter 4 is used to predict ice delamination given the ice shape recorded during tunnel testing. Comparisons are drawn between experimental results of static and dynamic asymmetric inflation techniques. The experimental pressure required to delaminate the ice is then compared to the pressure predicted by the Abaqus model.

5.1 Impulsive-Pneumatic De-Icing System Description

The pneumatic-impulsive de-icing system used in the flat plate model in Chapter 3 is fabricated into a NACA 0024 airfoil. The experimental airfoil, represented in SolidWorks, without the outer stainless steel shell is shown in Figure 5.1(a) with relevant dimensions. The system is shown with the 410 stainless steel outer shell is

shown in Figure 5.1(b).

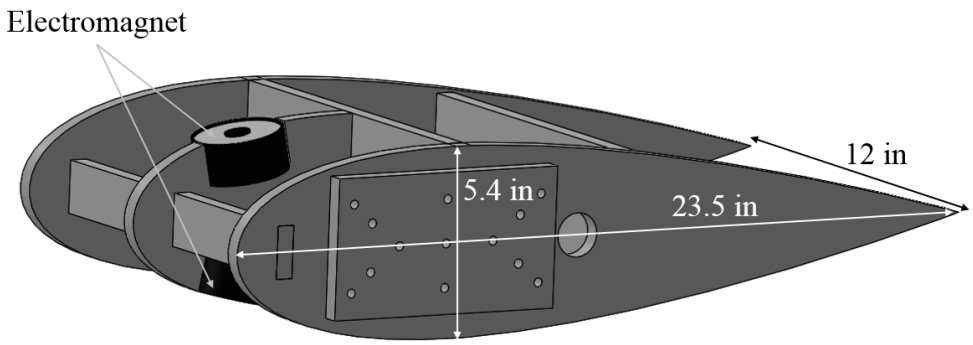

(a) No Outer Shell

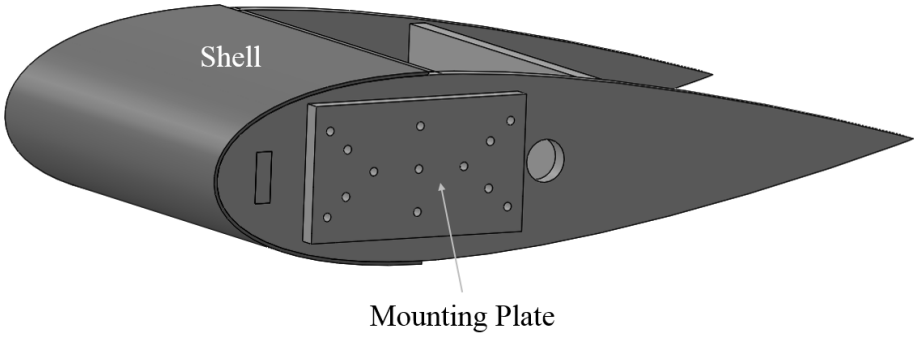

(b) Outer Shell Attached

Figure 5.1: Impulsive-Pneumatic De-Icing System

The de-icing system shown in Figure 5.1 covers the first 30% of the airfoil. The experimental model is fabricated entirely of Plexiglas and is shown in Figure 5.2 and Figure 5.3 without the outer stainless steel shell.

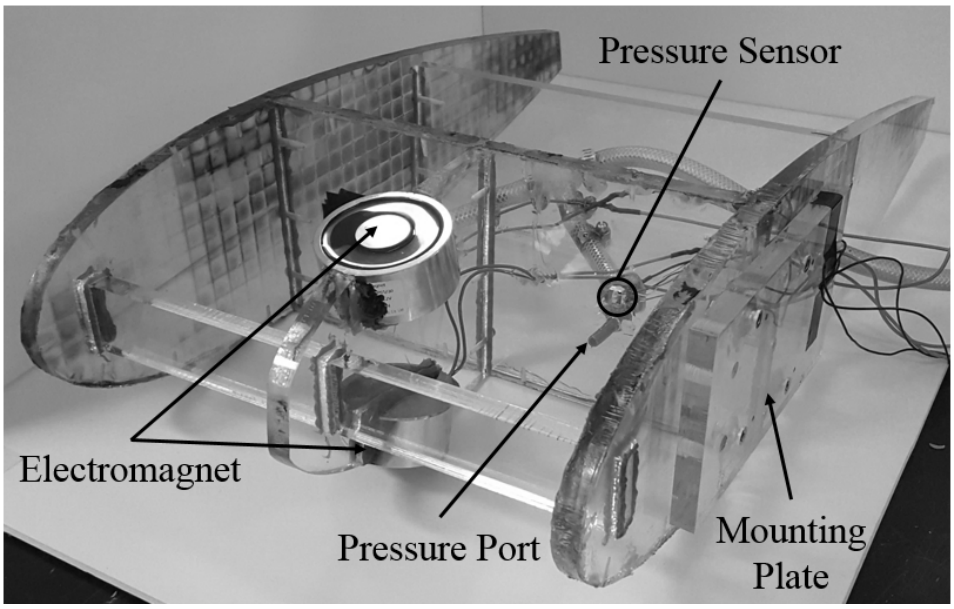

Figure 5.2: Experimental Impulsive-Pneumatic De-Icing System - Labeled

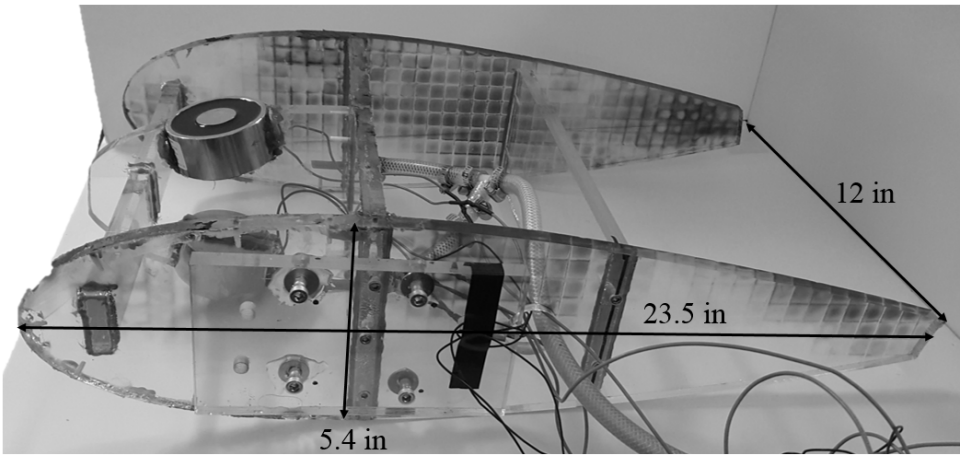

Figure 5.3: Experimental Impulsive-Pneumatic De-Icing System - Dimensions

Each electromagnet is rated to hold 800 N (180 lbf) at 12 VDC; therefore, the electromagnets provide a reasonable approximation to the boundary conditions used in the Abaqus model. The sizing of the electromagnets is not optimized for mass and power consumption. Like the flat plate model, additional ferromagnetic material must be attached to the underside of the shell so that the electromagnet fully

saturates through the material. The described additional ferromagnetic material is shown in Figure 5.4. The ferromagnetic material is glued to the stainless steel surface using an acrylic glue with a lap shear strength of 3,000 psi.

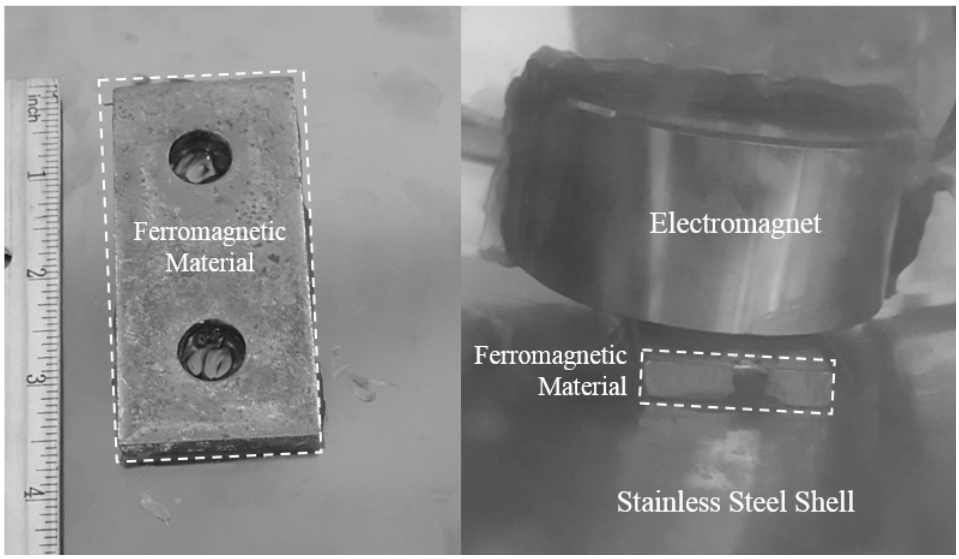

Figure 5.4: Experimental Impulsive-Pneumatic De-Icing System with Exterior Stainless Steel

The system is shown with the deformable external stainless steel surfaces is shown in Figure 5.5.

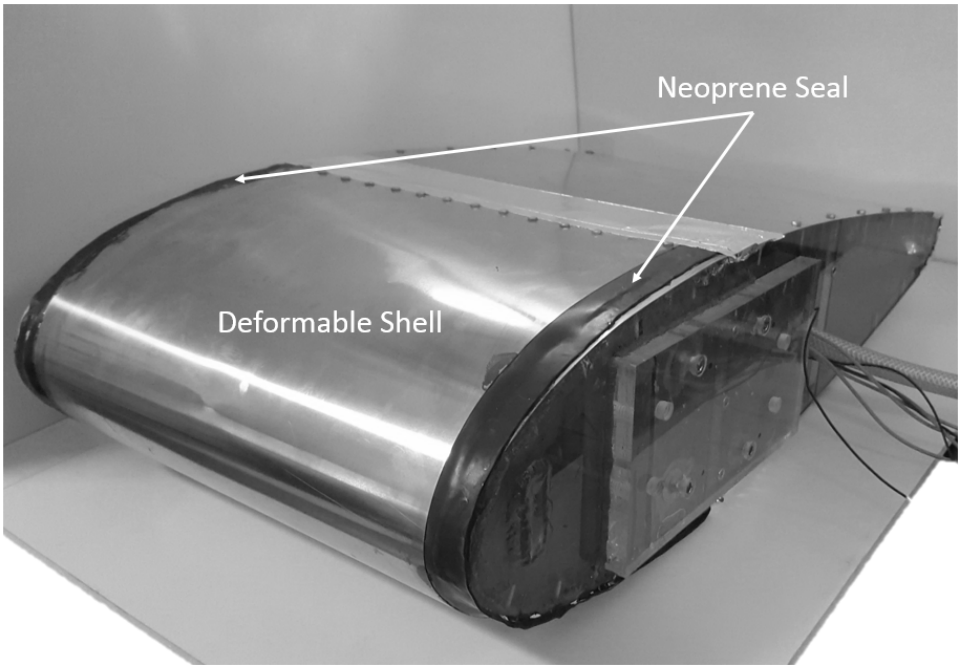

Figure 5.5: Experimental Impulsive-Pneumatic De-Icing System with Exterior Stainless Steel

A side view of the system shell under an applied pressure of 1.5 psi where deformation can be seen is shown in Figure 5.6.

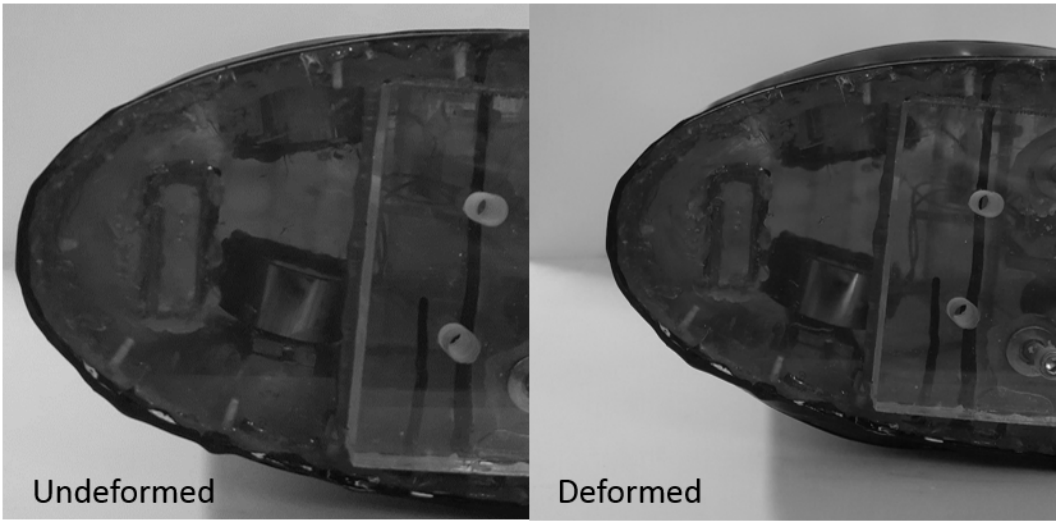

Figure 5.6: Side View Shell Deformation at 1.5 psi

5.2 Icing Tunnel Description

To verify the performance of the impulsive-pneumatic de-icing system predicted by the Abaqus airfoil model, testing was performed in Penn State's Icing Research Tunnel. The experiments are conducted to draw comparisons between predicted FEM results and experimental results.

5.2.1 Test Facility Description

The airfoil model verification took place in Penn State's Icing ResearchTunnel located in the Adverse Environment Research Testing Systems (AERTS) lab. A side view of the AERTS icing research tunnel is pictured in Figure 5.7.

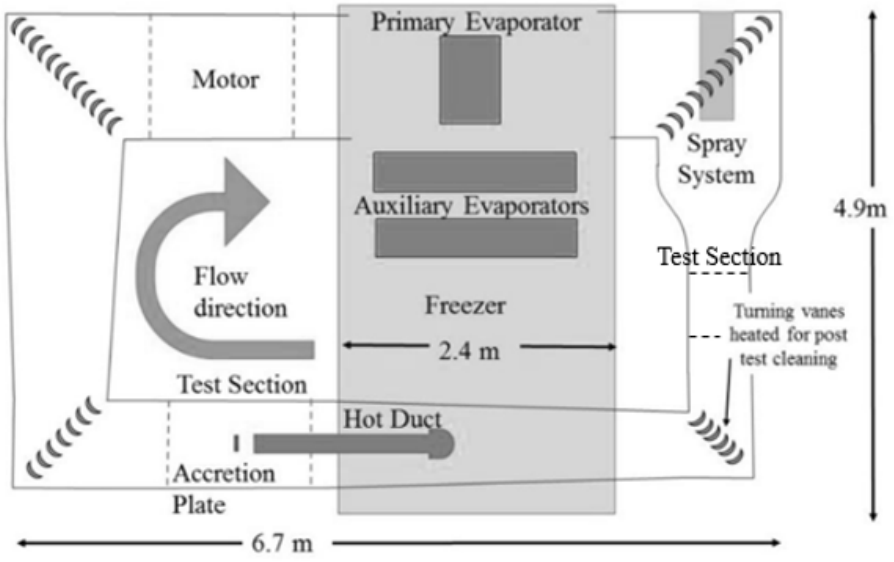

Figure 5.7: AERTS Icing Research Tunnel

The icing tunnel has two test sections, one on the lower-horizontal portion of the tunnel and one on the right-vertical portion. The horizontal test section has a

cross-section of 36.5 in. by 24.5-in, and the vertical test section has a cross-section of 20-in by 20-in. The tests ran for the verification of the airfoil Abaqus model were performed in the vertical test section immediately after the contraction section. The lowest achievable temperature at this location in the wind tunnel is -30°C (-22°F). The maximum wind speed is 77 m/s in the vertical testing section [3]. A spray system is located directly above the vertical testing section. The spray system uses four NASA Standard Nozzles to generate the icing cloud. In the NASA nozzle housing, the water pressure differs from the air pressure which effectively atomizes the water. The difference in pressures controls the MVD of the cloud. The calibration curves developed by NASA for these nozzles are shown below in Figure 5.8. During the icing tunnel testing, the airline used was 20 psi.

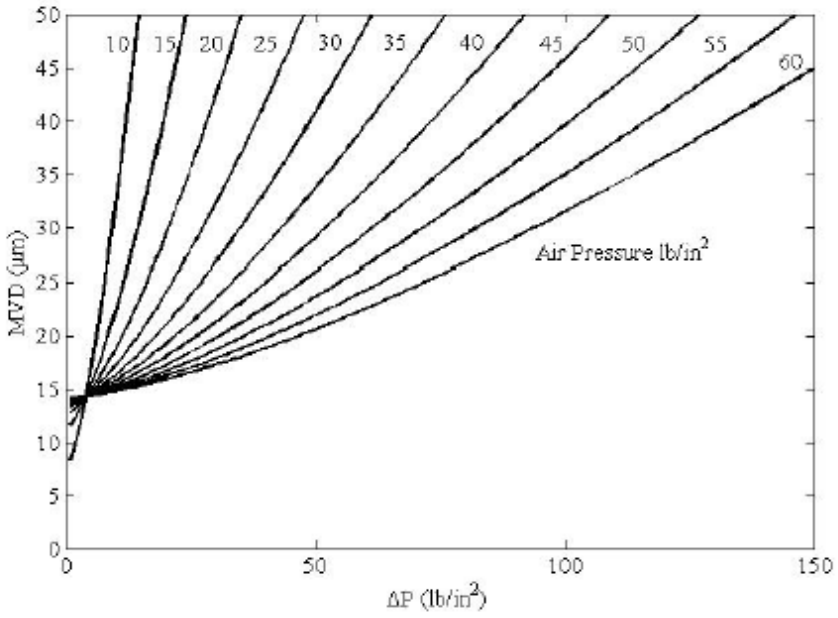

Figure 5.8: NASA Standard Nozzle Calibration Curves

5.2.2 Liquid Water Content Measurement

The LWC of the test section is important to measure as it characterizes the icing conditions. The units of LWC are typically given in g/m^3. The LWC is found by measuring the ice thickness at a stagnation point on a protruding rod in the middle of the icing cloud. A schematic of the measurement device is shown below in Figure 5.10.

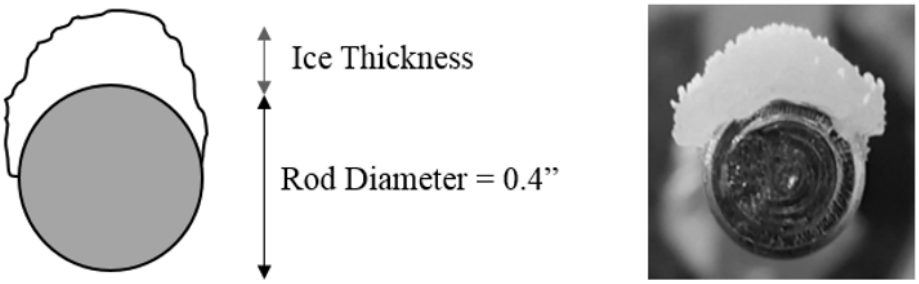

Figure 5.9: LWC Measurement

An algorithm designed by Han (Ref [24]) calculates the LWC when given the temperature, MVD, test duration, velocity of the water droplets, and the ice stagnation thickness. The basis of this algorithm stems from a NASA method to determine the LWC in the Icing Research Tunnel [24]. This process is an iterative scheme that compares the experimental ice thickness to a predicted thickness found by varying the freezing fraction. The freezing fraction is changed until the experimental thickness matches the predicted thickness. The logic the LWC algorithm follows is shown in Figure 5.10.

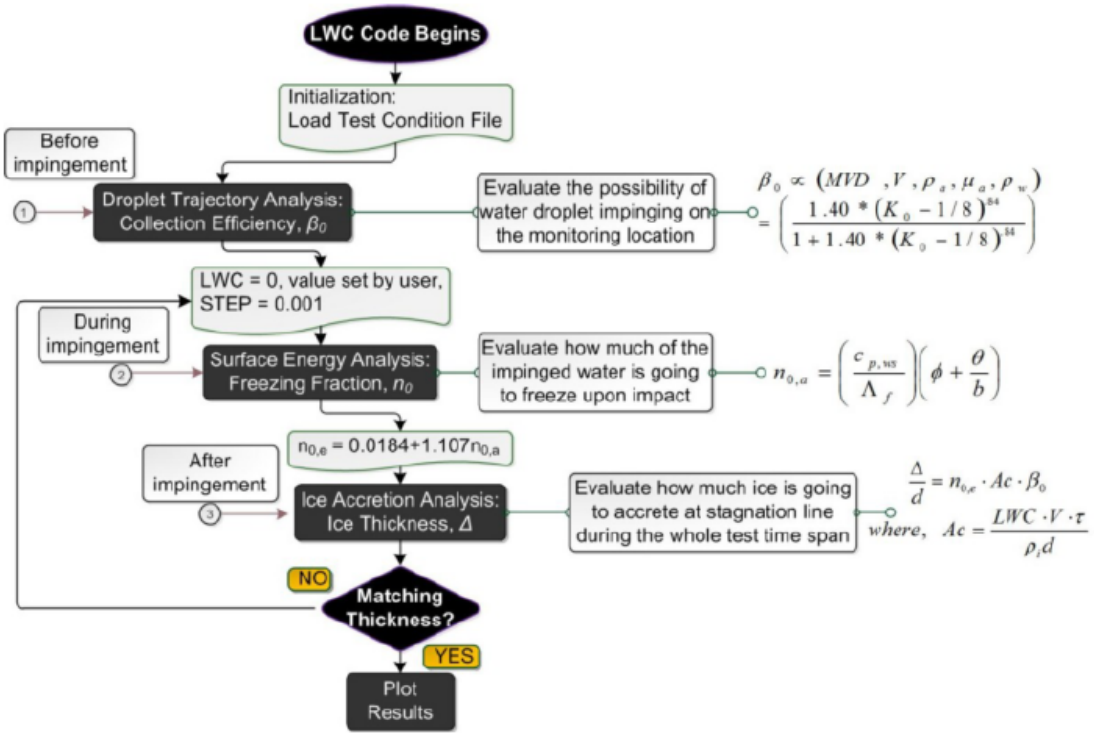

Figure 5.10: Algorithm to Determine LWC [10]

As Han discusses, there are certain testing conditions where this algorithm works best. At warmer temperatures, glaze icing conditions, the impacting water droplets can splash and run-back. Both effects will decrease the stagnation ice thickness which will result in a LWC which is lower than the true value. Since this is not desired, LWC measurements are best when taken at much colder temperatures which produce rime ice.

The time that is allowed for the ice to accrete to the measurement rod will also influence the calculated LWC. When the spray system is first turned on, it takes a short amount of time, approximately 10 seconds, until the cloud is uniform; therefore, the measurement time for LWC has to be longer than 10 seconds. Also, as time increases, ice is forming on the measurement rod and effectively changes the

aerodynamic shape of the rod. A change in the aerodynamic shape will also change the collection efficiency and thus the LWC calculations will not be representative of the physical cloud. It has been determined that to negate the effects of the cloud non-uniformity when measurement begins and collection efficiency changing as time increase, an appropriate measurement time is 30 seconds.

5.3 Comparison of Abaqus and Experimental Ice Delamination

This section describes the process by which Abaqus and experimental delamination results are produced and then compared. The delamination results for the experimental model for specific testing conditions are also shown.

5.3.1 Abaqus Modeling Process

The AERTS Icing Tunnel can change the temperature, airspeed speed, LWC, and MVD; therefore, there is an infinite combination of testing conditions. Therefore, only a select number of testing cases will be used to compare the experimental results to the Abaqus model. These cases are listed in Table 5.1.

Table 5.1: Testing Conditions for Abaqus and Experimental Comparison

Case	**Temperature**	**Duration**	**Speed**	**MVD**
1	-10°C	2 min	35 $\frac{m}{s}$	20 μm
2	-10°C	3 min	35 $\frac{m}{s}$	20 μm
3	-10°C	4 min	35 $\frac{m}{s}$	20 μm
4	-10°C	5 min	35 $\frac{m}{s}$	20 μm

The temperature is kept at -10°C since changing the test temperature would result in different ice/shell interface properties. The speed and MVD are also kept constant during the four test cases. If the speed and MVD were to change across the tests, due to physics & thermodynamics of ice accretion, the characteristics of the ice would change.

The process of obtaining Abaqus results begins with acquiring an ice shape from icing tunnel tests. After ice has accreted to the airfoil according to the conditions in Table 5.1, an image is taken from the side looking spanwise. Digital calibers are then used to measure the thickness of the ice along the leading edge. From the image and thickness measurements, an ice shape can be generated in Abaqus. The ice can be isolated and recreated in Abaqus FEA. The experimental ice and the ice generated in Abaqus are shown in Figure 5.11.

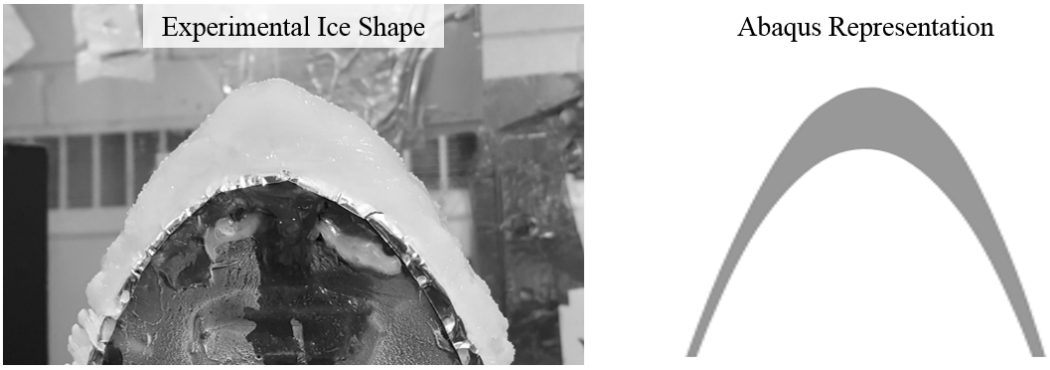

Figure 5.11: Experimental Ice Accretion and Abaqus Representation - Case 1

Once the Abaqus model has the attached ice, the same process can be performed as in the flat plate model. A pressure can be applied and the nodal position determined at the end of the inflation period. If the nodal separation has not exceeded the cohesive failure distance (6.88 μm), the pressure is increased and the process is repeated. The required pressure to completely delaminate the ice can be determined using this process for the three inflation techniques: static, dynamic symmetric, and dynamic asymmetric.

5.3.2 Experimental Process

The experimental airfoil model shown in Figure 5.2 and 5.3 is mounted in the AERTS Icing Tunnel in the vertical test section (Figure 5.12). The mounting plate is mated with a load-cell which is rigidly attached to the icing tunnel.

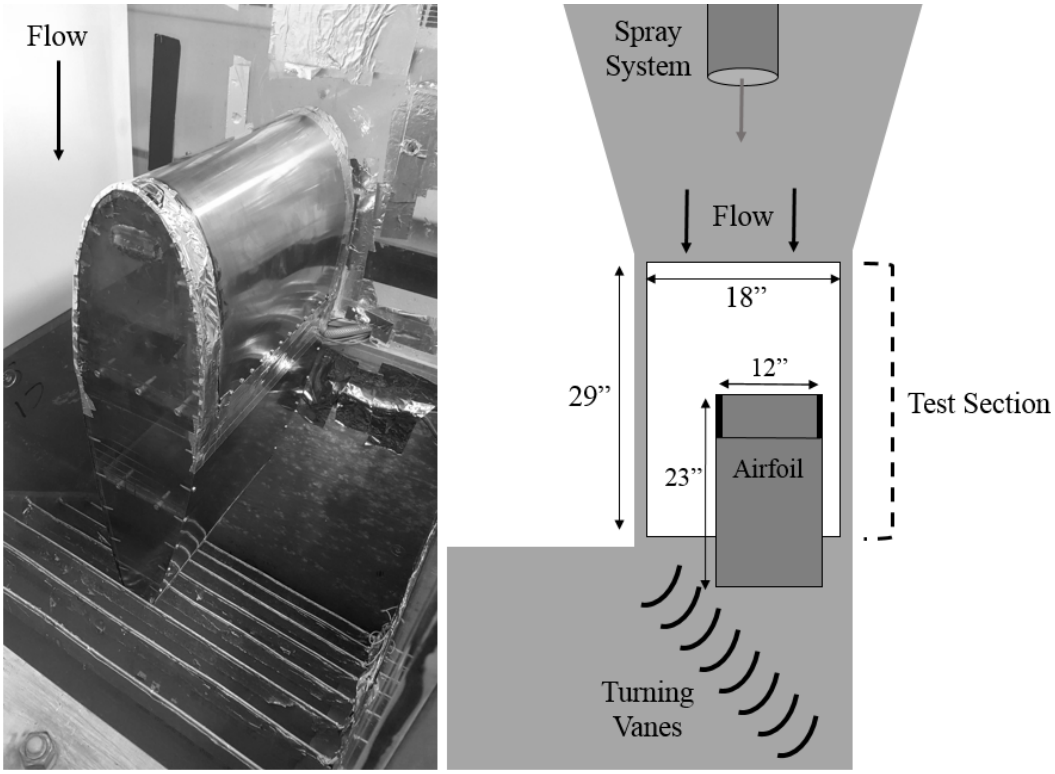

Figure 5.12: Experimental Model Mounted in the Vertical Test Section

The testing conditions, which are listed in Table 5.1, are set on the icing tunnel controller pictured in Figure 5.13.

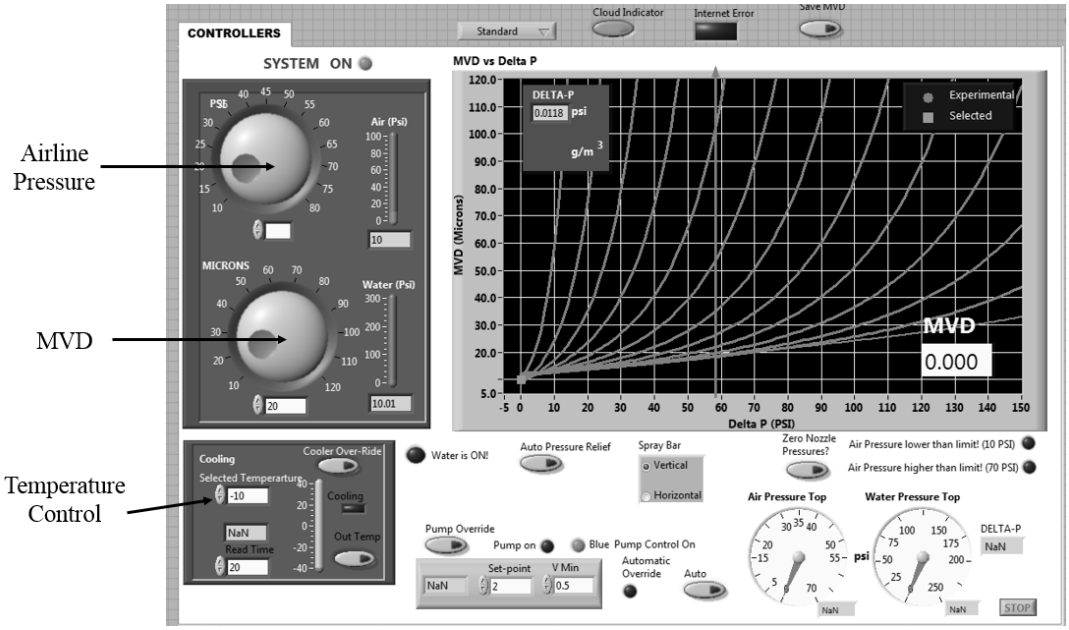

Figure 5.13: AERTS Icing Tunnel Controller

Once the testing conditions are correctly set, the tunnel is brought up to speed. Next, the water is turned on and the icing cloud forms. The ice is then allowed to accrete to the de-icing system for the prescribed amount of time. The accreted ice for case 1 is shown in Figure 5.14.

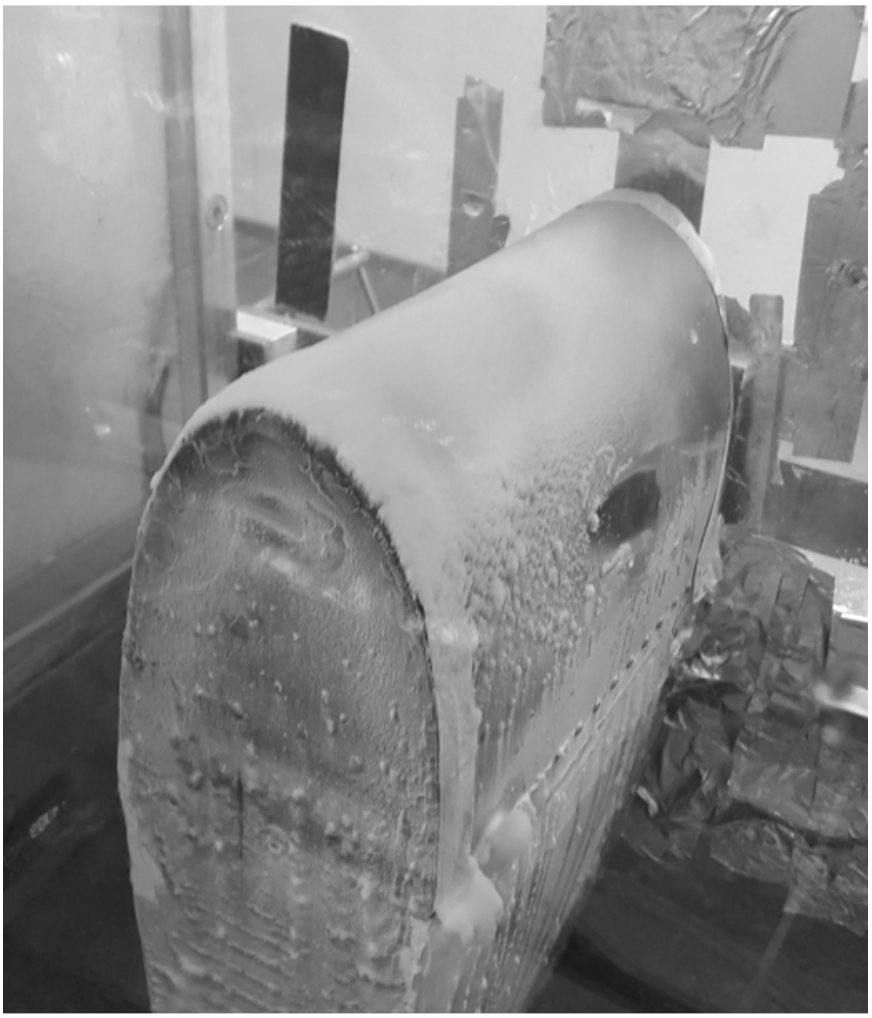

Figure 5.14: Final Ice Accretion - Case 1

After the icing is complete, since the Abaqus model does not account for the boundaries of the airfoil but rather where the electromagnets are located, the accreted ice on the edges are removed using a heated metal cutout. The removal of the ice has to be quick as to not melt the interface resulting in a lower required pressure to delaminate. The process of the ice removal is illustrated in Figure 5.15.

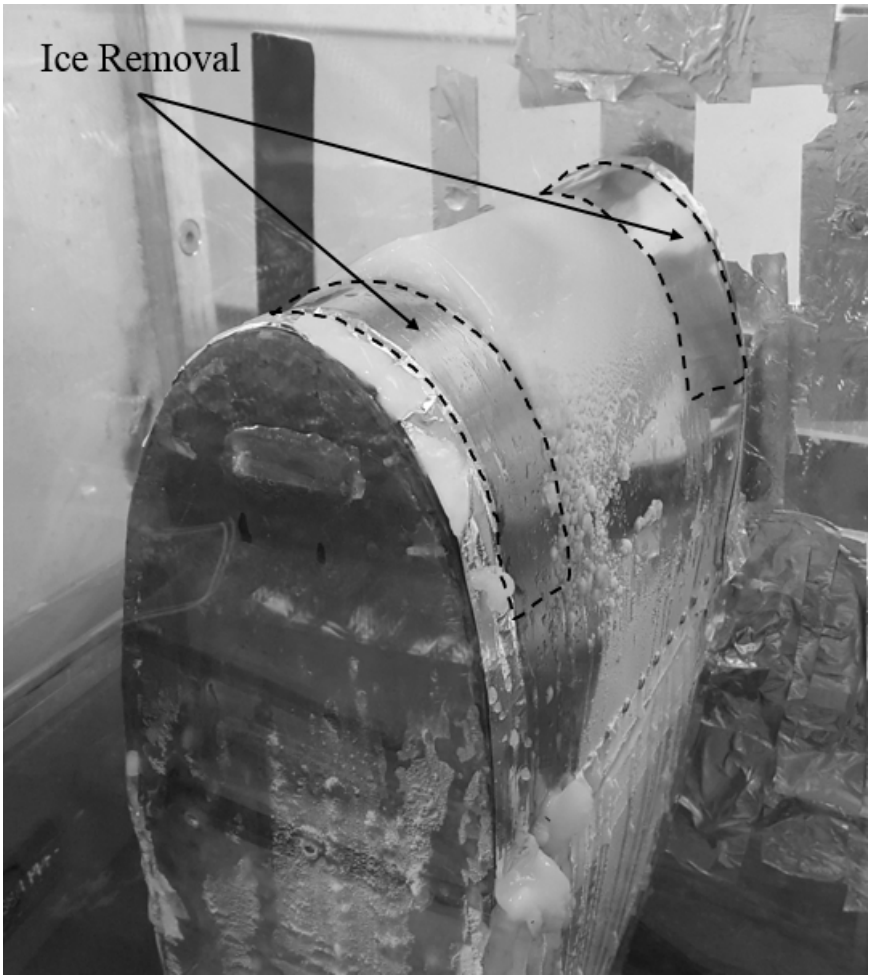

Figure 5.15: Ice Removal - Case 1

Once the ice has been removed, the pressure applied to the inner side of the shell is gradually increased using an air regulator. Once the applied air pressure reaches the desired value, the electromagnets are disabled in an asymmetric fashion using an Arduino microcontroller and relay (Figure 5.16).

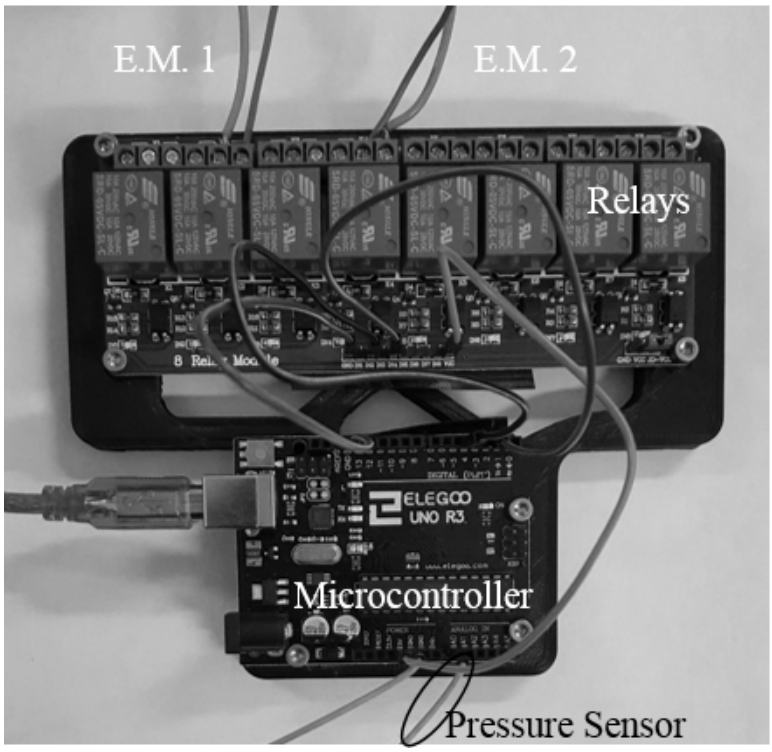

Figure 5.16: Arduino System to Control Electromagnets

5.3.3 Icing Tunnel Results

During icing tunnel tests, only static and dynamic asymmetric inflation techniques were used. This is because the Abaqus models showed that the dynamic asymmetric technique is the best of the three methods. Also, from the both the flat plate testing and modeling, the dynamic asymmetric inflation technique always requires less pressure. The static inflation technique is used to demonstrate the benefit of the impulsive aspect of the de-icing system. The required pressure for a given leading edge ice thickness for the static and dynamic asymmetric inflation techniques is shown in Figure 5.17.

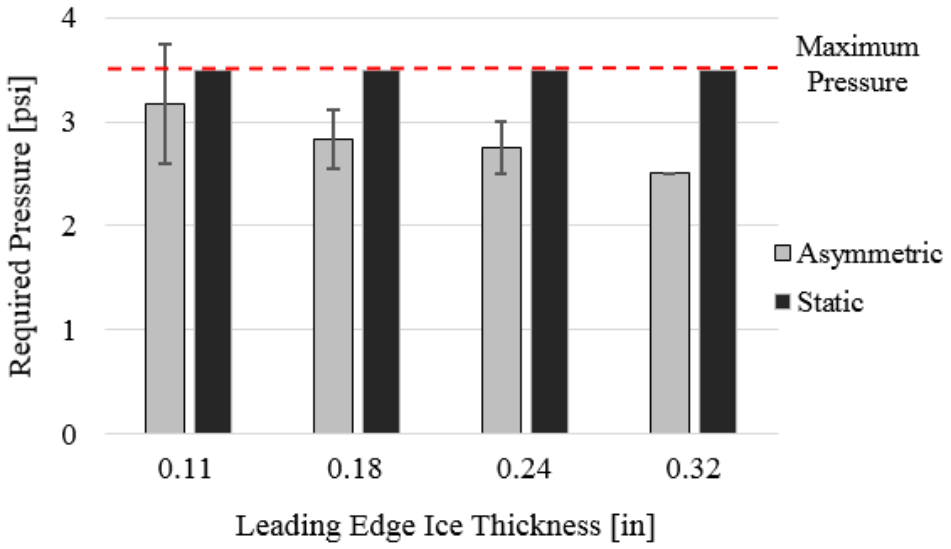

Figure 5.17: Experimental Results

For all leading edge ice thicknesses, the dynamic asymmetric inflation technique out performs the static technique. As the leading edge ice thickness increases, the required pressure to delaminate decreases which was seen in the flat plate testing too. Also, the static inflation case never successfully delaminated the accreted ice. The static inflation technique always reached the maximum allowable pressure. Once the applied pressure reaches this identified limit, the neoprene seal along the edges being to fail. For thin ice shapes (0.11-in & 0.18-in), the static inflation case was able to crack the ice, but delamination did not occur (Figure 5.18).

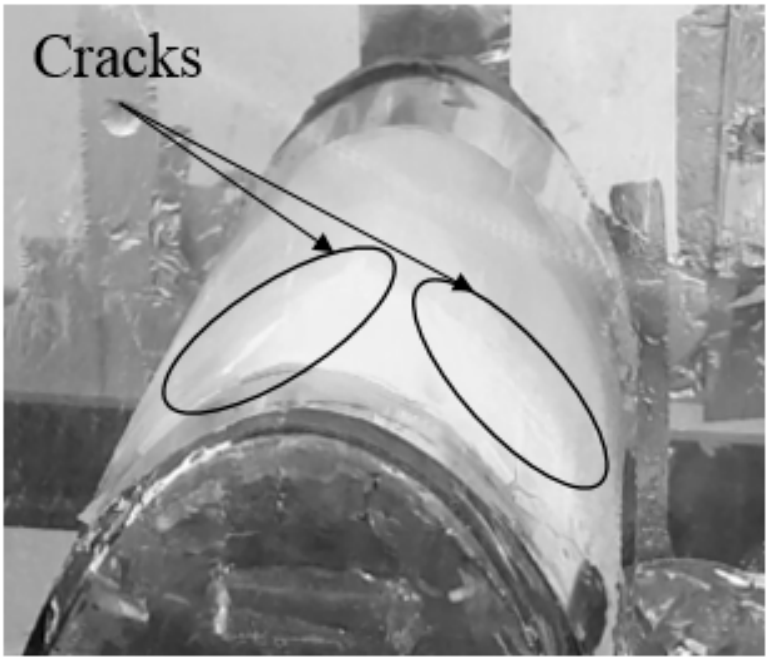

Figure 5.18: Cracks Resulting from Static Inflation

Also of note, at thin ice thicknesses, when using the dynamic asymmetric inflation technique the ice fractured. At larger ice thicknesses, the ice did not fracture but still delaminated from the airfoil. The before and after images of the dynamic asymmetric case for case 1, which is thin ice, is shown in Figure 5.19.

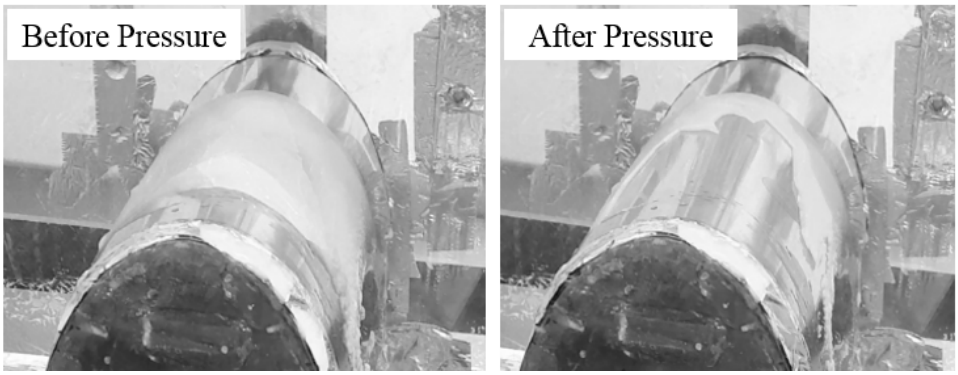

Figure 5.19: Ice Before and After Applied Pressure - Case 1

For a greater leading edge ice thickness such as case 4, the ice no longer fractures,

but does still delaminate (Figure 5.20). Only ice farther from the leading edge fractures and is carried away by the airflow.

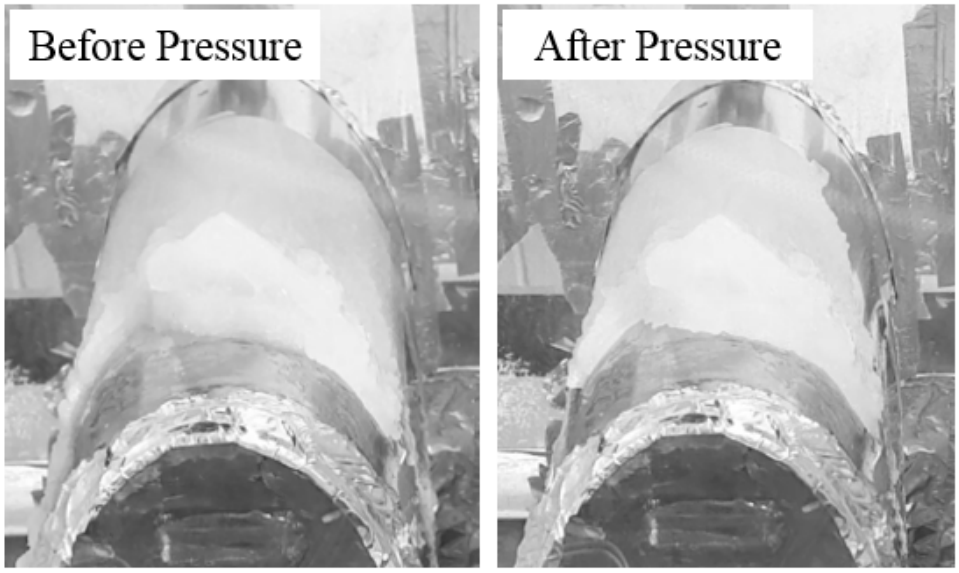

Figure 5.20: Ice Before and After Applied Pressure - Case 4

The ice from case 4 (Figure 5.20), while not fracturing like cases 1, 2, and 3, had a clean delamination which can be shown in Figure 5.21.

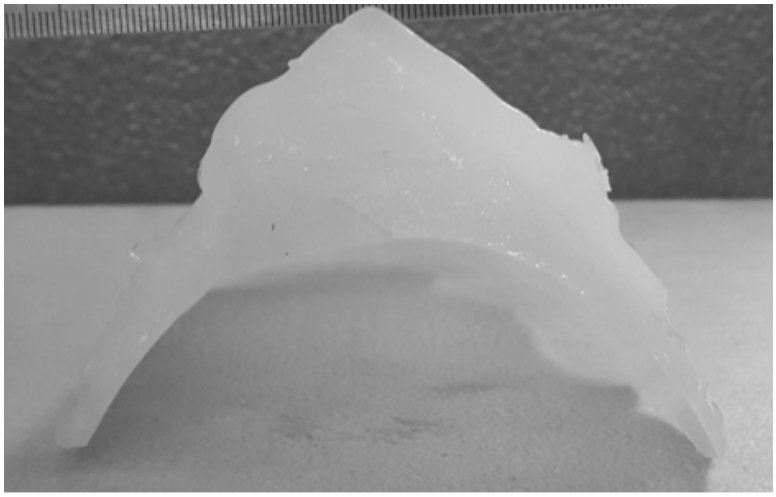

Figure 5.21: Case 4 Ice after Applied Pressure

This observation leads to a critical ice thickness such that once pressure is applied

the ice will either fracture or stay intact while still delaminating. The critical ice thickness is thus between ice thicknesses achieved in cases 3 and 4. The critical ice thickness overlaid with the dynamic asymmetric icing tunnel results is shown in Figure 5.22.

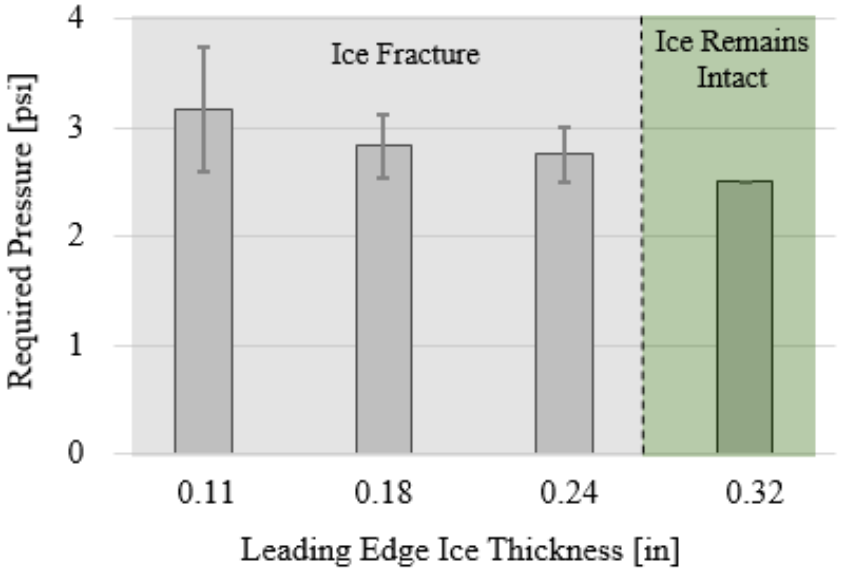

Figure 5.22: Dynamic Asymmetric Inflation Critical Ice Thickness

5.4 Abaqus and Experimetnal Delamination Comparison

Using the method described in Section 5.3.1, delamination results from Abaqus are found. In all cases, the accreted ice does not 100% delaminate, the criteria for a complete delamination. Instead, a small amount of ice remains bonded around the leading edge. The nodal separation predicted by Abaqus for case 4 is shown in Figure 5.23.

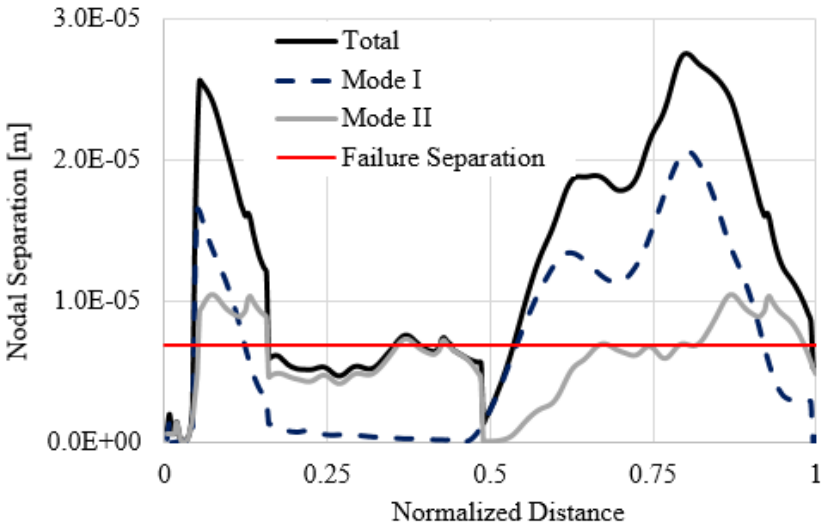

Figure 5.23: Nodal Separation Case 4

As stated, the ice does not 100% delaminate from the airfoil. Also, the electromagnet at 85% the normalized distance, which released first, yields a larger range of nodal separation compared to the electromagnet at 15%. All four cases yield similar results in that some portion of the ice remains bonded after the applied pressure and electromagnet release. A corrected model can be implemented to capture effects seen during testing that the model does not account for.

5.4.1 Corrected FEA Model

Since the FEA model does not account effects seen during experimental testing, a correction to the model is justified. These such effects could include: asymmetric drag, unsteady vibrations, nonuniform icing, too much ice remaining after the ice removal process, etc.. One of the effects which is quantifiable is asymmetric drag. When ice accretes to the airfoil, no symmetry axes exists as seen in the ice shape for case 4 (Figure 5.24). Due this asymmetry drag is greater on one side of the ice

than the other producing additional shearing forces.

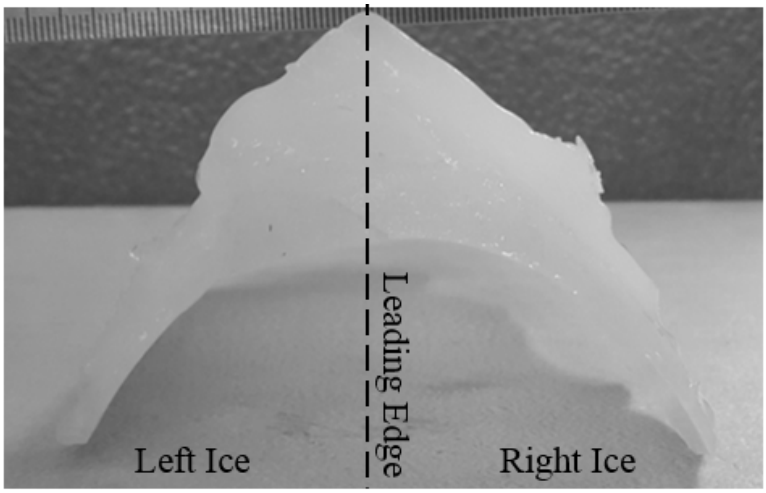

Figure 5.24: Case 4 Ice - No Symmetry along Leading Edge

The ice shape on one side of the airfoil can be mirrored and thus the two differing sides of accreted ice can be compared. The 2D drag coefficients for a clean NACA 0024 airfoil, mirrored left ice, and mirrored right ice are shown in Figure 5.25.

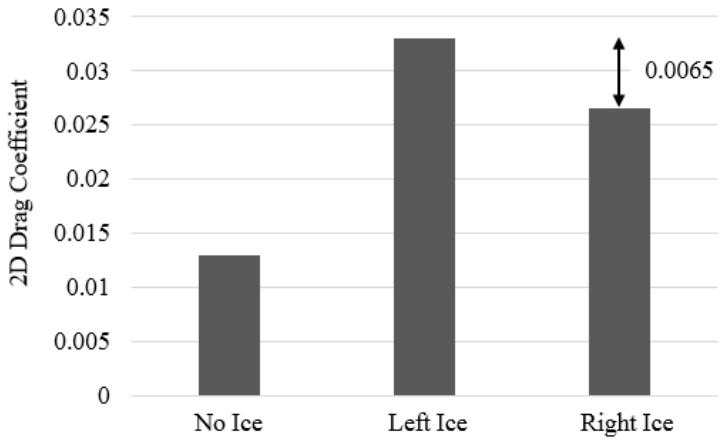

Figure 5.25: 2D Drag Coefficient Comparison - Case 4 Ice

Thus, the resulting drag coefficients and associated drag can be visualized in Figure 5.27. Due to the greater 2D drag coefficient on the left side of the ice, there exists

a shear imbalance which can be modeled in the FEA model.

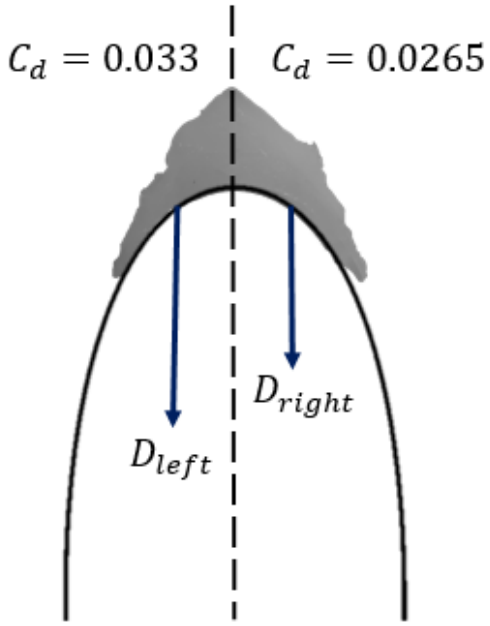

Figure 5.26: Differing Ice 2D Drag Coefficient with Associated Drag - Case 4 Ice

During the static and dynamic steps in the FEA model, an additional drag force equal to $\frac{1}{2}\rho AV^2(C_{D_{left}} - C_{D_{right}})$ can be added to the left portion of the ice which will assist in delamination due to additional shear forces. ρ in this case is the air density at -10°C. The described drag force in the FEA model is shown as a point force in Figure 5.27.

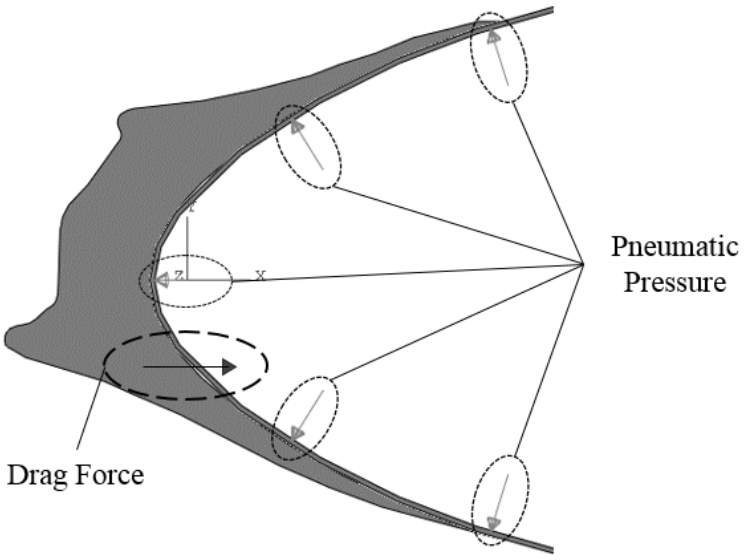

Figure 5.27: Location of Additional Drag Force in FEA Model

Using the corrected model accounting for asymmetric drag, the percent debond line for case 4 is approximately 96% from 83%. The nodal separation using the corrected FEA model for case 4 is shown in Figure 5.28. The remaining 4% that remains attached to the leading edge can be contributed to other experimental factors such as vibrations, uneven icing cloud, ice bonded to the stainless steel shell beyond the influence of the electromagnets.

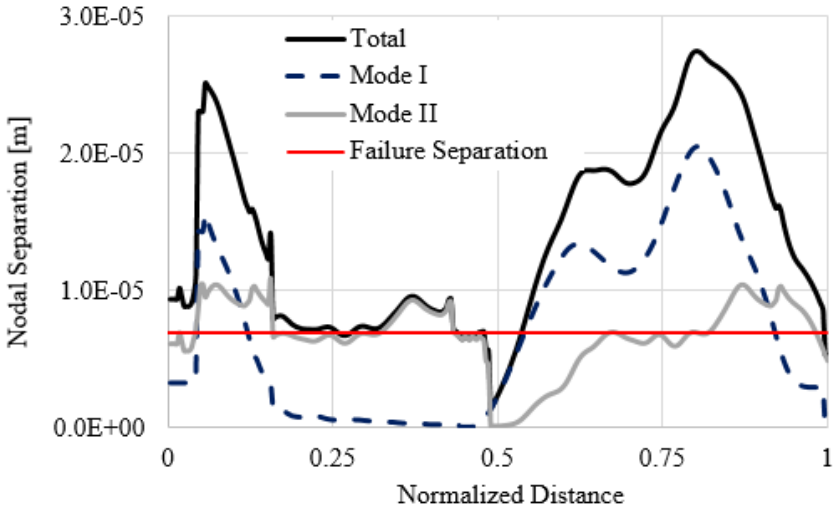

Figure 5.28: Nodal Separation using Asymmetric Drag FEA Model Correction - Case 4

With the asymmetric drag correction, the experimental and predicted required pressure for the dynamic asymmetric inflation case can be compared (Figure 5.29).

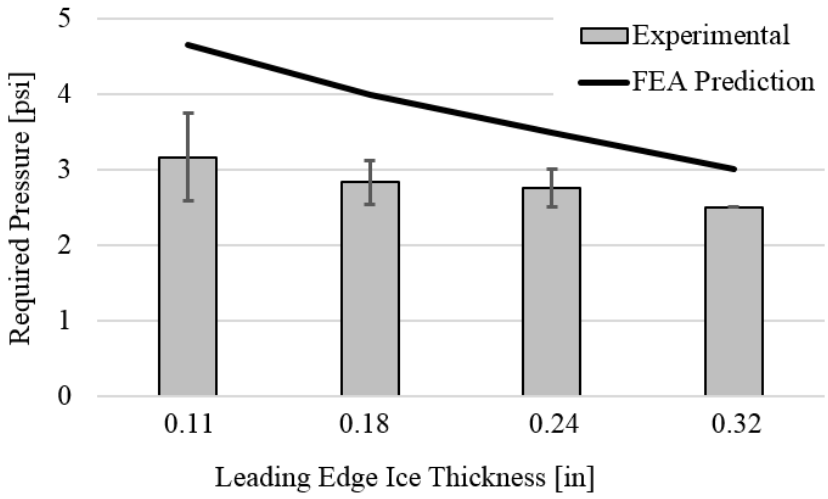

Figure 5.29: Asymmetric Drag FEA Model Correction and Experimental Required Pressure Comparison - Dynamic Asymmetric Inflation

The model and experimental results follow the same trend that thinner leading edge ice thickness requires a greater pressure to delaminate. The percent difference

between the experimental and corrected Abaqus model for case 4, the thickest leading edge ice thickness, is approximately 18%. As the leading edge ice thickness decreases, the percent difference increases. This is due to the ice fracturing during experiments for cases 1, 2, and 3. The FEM model does not incorporate material cohesive failure, but rather the ice remaining whole and delaminating from the airfoil. When the ice does remain whole such as case 4 (0.32-in leading edge ice thickness), the corrected FEM model prediction and experimental results are better aligned. Averaged over the four comparison cases the percent difference is approximately 28%.

Chapter 6
Conclusions

6.1 Conclusion

This research effort modeled a novel hybrid impulsive-pneumatic de-icing system was modeled in Abaqus FEA and verified in experimental testing. Two FEA models were developed and then fabricated for experimental testing: a flat plate model and NACA 0024 airfoil model. The impulsive aspects were implemented by constraining and releasing two sections of the plate/airfoil adding additional inertia effects helping to delaminate accreted ice. In both the flat plate and airfoil testing, the added impulsive effects were seen to be much more effective than simple static inflation cases by requiring less pressure to delaminate ice. A novel approach to model the cohesive behavior was taken. Both static and dynamic behavior of the de-icing system were used to analyze the de-icing capability. In previous literature, only static behavior was considered.

6.1.1 Flat Plate Model

The ice and stainless steel cohesive behavior was first modeled in Abaqus FEA using experimentally determined cohesive properties. This model was used to demonstrate the benefit of the added impulsive behavior. A bench-top flat plate model was then fabricated to verify the FEA model. Freezer ice was attached to the flat plate and was delaminated using the three inflation techniques. A cohesive surface modulus for 410 stainless steel was experimentally determined. From the flat plate FEA model and bench-top testing, the following conclusions are made:

- The dynamic inflation techniques, for all ice thicknesses, required less pressure than the symmetric inflation case. On average, the asymmetric release required 15% less pressure than the symmetric release case. Also, the dynamic asymmetric case proved to be more effective at delaminating ice than the dynamic asymmetric case for all ice thicknesses. For the dynamic asymmetric inflation technique, 0.3-in ice was able to be delaminated with as little as 0.39 psi.

- A cohesive surface modulus, used to model the cohesive behavior, was experimentally determined for the 410 stainless steel. The new value is $1.17\text{x}10^{12} N/m^3$, a 17% increase from the experimentally determiend Aluminum cohesive surface modulus. The new value of the cohesive surface modulus was then used in the airfoil FEA model.

6.1.2 Airfoil Model

Using the newly determined cohesive surface modulus, the impulsive-pneumatic de-icing technique was implemented onto a NACA 0024 airfoil in Abaqus. Compared to the flat plate modeling, similar results were seen such that the dynamic inflation techniques outperformed the static inflation technique. Again, the FEA model showed that with the same applied pressure the asymmetric inflation technique yielded 15% more nodal separation than the symmetrical inflation technique. An experimental model of the NACA 0024 de-icing system was then fabricated for testing in the AERTS Icing Tunnel. Since the experimental model was tested in the icing tunnel, dynamic pressure was added to the FEA model. From the FEA model and experimental results, the following conclusions are made:

- For all ice thicknesses, both the FEA model and experimental results show that the dynamic inflation technique outperforms the static inflation technique.
- During experiments, the static inflation technique was never able to delaminate the accreted ice on the airfoil. For thinest leading edge ice thickness (case 1), cracks did form but the ice did not delaminate. For all cases, the dynamic asymmetric inflation case was able to delamiante the accreted ice. For cases 1, 2, and 3, since the ice was relatively thin, the ice fractured. In case 4, the thickest leading edge ice, did not fracture, but still delaminated from the airfoil.
- When implementing asymmetric drag on the ice, the FEA model is able to predict when ice delamination will occur. For cases when the ice did not fracture, the percent difference between the FEA model and experimental

results is approximately 18%.

- For thin leading edge ice thicknesses, ice fractured during experiments which likely accounts for the differences between FEA model predictions and experimental results. The FEA model does not account for material cohesive failure (ice fracturing).

6.2 Recommendations for Future Work

6.2.1 Abaqus Modeling

6.2.1.1 Cohesive Parameters

The Abaqus model was constructed using stiffness factors for only -10°C which were experimentally determined by Ref. [11]. These stiffness factor values are also only valid for aluminum materials. A more encompassing Abaqus model could be constructed if the stiffness factors were experimentally determined for additional materials and wider range of temperatures. Not only is the material important, the surface composition has to be characterized in terms of roughness to calculate the most accurate stiffness factor.

6.2.1.2 Incorporation of 3D Effects

Another area of improvement with respect to the Abaqus model is the dimensionality. In this research, the model was completely 2D and does not incorporate the boundaries of the airfoil. A 2D model was used for simplicity and to conserve computational resources. If more computing power were to be acquired, a 3D model

could be used to produce more representative results.

Along the boundaries of the airfoil, there will be less deformation than in the center of the airfoil section. Thus, the de-icing capability will be reduced along these areas. A 3D FEA model would have the capabilities to determine the effects around the edges of the airfoil.

6.2.1.3 Material Cohesive Failure

The Abaqus model presented in this research only has the ability to capture delamination between the ice and the shell interface. In reality, there may be fracturing of the ice. Only a small portion of the flat plate tests resulted in ice fracture, but a more significant portion of the airfoil tests resulted in the ice fracturing, especially at the thin leading edge ice thicknesses. If the Abaqus model was modified to account for the ice fracturing, the experimental results and the Abaqus model predictions would become better aligned. More fundamental research on the material properties of ice would have to be conducted to be able to predict the fracturing behavior of ice. The ice fracturing properties would have to be determined at varying impact ice conditions to compile a comprehensive model. As the temperature, testing speed, LWC, and MVD change, the impact ice fracture properties would too change.

6.2.2 Impulsive-Pneumatic Airfoil System Design

Since the dynamic release inflation technique was shown have advantages over a static inflation technique, the airfoil design could be further advanced. The sizing of the needed electromagnets could be better optimized to save weight and power.

The current iteration could only hold a pressure up to 3.5 psi which could also be improved to see static delamination occur. Aerodynamic studies could be performed to demonstrate the effects on drag caused by the inflatable stainless steel shell.

Additional studies could be conducted which implement an electrothermal parting strip. In the modeling, the ice along the leading edge stay bonded to the stainless steel shell. Adding a low power electrothermal parting strip could solve this issue. Abaqus modeling could then incorporate NASA's LEWICE software which could generate adjusted ice shapes based on the power provided to the parting strip.

Lastly, the airfoil de-icing system should be evaluated at a wider range of icing tunnel testing conditions. Testing conducted during this thesis was limited to -10°C due to the cohesive properties. The speed and MVD were also held constant. Rather than comparing the experimental results to the FEA model, the limits and capabilities of the physical system should be evaluated.

Bibliography

[1] Samuel T. Buschhorn, Seth S. Kessler, Noa Lachmann, Jennifer Gavin, Greg Thomas, and Brian L. Wardle. Electrothermal Icing protection of Aerosurfaces Using Conductive Polymer Nanocomposites. *54th AIAA/ASME/ASCE/AHS/ASC Structures, Structural Dynamics, and Materials Conference*, pages 1–8, 2013.

[2] Matthew Drury. *Design and Testing of an Improved Centrifugally Powered Pneumatic De-icing System for Helicopter Rotor Blades.* Masters, The Pennsylvania State University, 2016.

[3] Kim Lynge Sorensen and Tor Arne Johansen. Flight test results for autonomous icing protection solution for small unmanned aircraft. *2017 International Conference on Unmanned Aircraft Systems, ICUAS 2017*, pages 971–980, 2017.

[4] Charles a. Martin and James C. Putt. Advanced pneumatic impulse ice protection system (PIIP) for aircraft. *Journal of Aircraft*, 29(4):714–716, 1992.

[5] Ilhan Tuncoz. *Design and Analysis of a Hybrid Trailing Edge Control Surface of a Fully Morphing Unmanned Aerial Vehicle Wing.* PhD thesis, Middle East Technical University, 2015.

[6] W Geer and M Scott. The Prevention of the Ice Hazard on Airplanes. Technical report, Washington D.C., 1930.

[7] Jin Hu. Deicer Boots having Differenet Elastomer Fibers, 2016.

[8] John Pepin. US Army Tests Icing on Helicopters at Marquette Airport, 2016.

[9] E a Schuchard, J W Melody, Tamer Basar, W R Perkins, and P Voulgaris. Detection and Classification of Aircraft Icing Using Neural Networks. *38th AIAA Aerospace Sciences Meeting & Exhibit*, (c), 2000.

[10] Yiqiang Han, Jose Luis Palacios, and Edward C. Smith. An Experimental Correlation between Rotor Test and Wind Tunnel Ice Shapes on NACA 0012 Airfoils. *SAE Technical Paper 2011-38-0092*, (June 2011), 2011.

[11] Matthew J Bailey. *Modeling and Experimental Testing of a Centrifugally Powered Pneumatic De-Icing System for Rotor Blades.* Masters, The Pennsylvania State University, 2014.

[12] M Riahi. The Experimental/Numerical Study to Predict Mechanical Behaviour at the Ice/Aluminium Interface. *Elsevier Science*, 65:191–202, 2011.

[13] Phiilip Krammer and Scholz Dieter. Estimation of Electrical Power Required for De-icing Systems. Technical report, Hamburg University of Applied Sciences, 2009.

[14] Galdemir Botura, Dave Sweet, and David Flosdorf. Development and Demonstration of Low Power Electrothermal De-icing System. *43rd AIAA Aerospace Sciences Meeting and Exhibit*, (January):1–15, 2005.

[15] D Sweet. Giving Ice the boot: Understanding Pneumatic De-icing. Technical report, UTC Aerospace Systems Tech. Bulletin 101, 2015.

[16] Stefan Jung, Marko Dorrestijn, Dominik Raps, Arindam Das, and Constantine M Megaridis. Supporting Information Are superhydrophobic surfaces best for icephobicity ? pages 1–12.

[17] Piotr Tourkine, Marie Le Merrer, and David Qu. Delayed Freezing on Water Repellent Materials. 25(14):7214–7216, 2009.

[18] S A Kulinich, S Farhadi, K Nose, and X W Du. Superhydrophobic Surfaces : Are They Really Ice-Repellent ? 27(25):25–29, 2011.

[19] Dynamic Article Links. Below the freezing point retard ice / frost formation. pages 3993–4000, 2011.

[20] Markus Susoff, Konstantin Siegmann, Cornelia Pfaffenroth, and Martina Hirayama. Applied Surface Science Evaluation of icephobic coatings — Screening of different coatings and influence of roughness. *Applied Surface Science*, 282:870–879, 2013.

[21] B Wright. *User Manual for the NASA Code Ice Accretion Code LEWICE.* Number August 2002. NASA Glenn, Cleveland, Ohio, 2018.

[22] New Generation De-Ice Systems: Hybrid Thermo Electric Ice Protection System. Technical report, Laminar Deice.

[23] Lyndsey Blair. AMERICAN EAGLE FLIGHT 4184. (April), 2016.

[24] Yiqiang Han and Jose Palacios. Analytical and Experimental Determination of Airfoil Performance Degradation Due to Ice Accretion. *4th AIAA Atmospheric and Space Environments Conference*, (June):1–25, 2012.

[25] M. B. Bragg, a. P. Broeren, and L. a. Blumenthal. Iced-airfoil aerodynamics. *Progress in Aerospace Sciences*, 41(5):323–362, 2005.

[26] Air Command TP 9353 E Weather Manual. Technical report, Ontario, 1987.

[27] With Ancillaries. Code of Federal Regulations Title 14 Parts 1 to 59. Technical report, Office of the Federal Register National Archives and Records Administration, 2004.

[28] Supercooling and Freezing of Water. *Journal of Research of the National Bureau of Standards*, 20, 1938.

[29] Bernard L Messingert. Equilibrium Temperature of an Unheated Icing Surface as a Function of AirSpeed. *Journal of the Aeronautical Sciences*, 20(1):29–42, 1953.

[30] Cameron Tropea and Elmar Bonaccurso. Physics of aircraft icing : A predictive challenge. *Int. Symp. on Turbulence, Heat and Mass Transfer*, 8(September), 2015.

[31] R Gent, N Dart, and J Cansdale. Aircraft Icing. *The Royal Society*, 2000.

[32] *Air Command TP 9553 E Weather Manual*. Ottawa, Ontario, Canada, 1987.

[33] Edward Brouwers. *The Experimental Investigation of a Rotor Icing Model with Shedding*. Masters, The Pennsylvania State University, 2010.

[34] E.W.a Brouwers, A.A.a Peterson, J.L.b Palacios, and L.R.c Centolanza. Ice adhesion strength measurements for rotor blade leading edge materials. *Annual Forum Proceedings - AHS International*, 4:3011–3023, 2011.

[35] Jared T Soltis and Douglas Wolfe. *Design and Testing of an Erosion Resistant Ultrasonic De-Icing System for Rotorcraft Blades*. PhD thesis, The Pennsylvania State Unicersity, 2013.

[36] Grant Schneeberger and Jose Palacios. Superhydrophobic Materials are NOT Suitable for Passive Ice Protection of Aircraft. 2017.

[37] Yuanyi Wang, Jian Xue, Qingjun Wang, Qingmin Chen, and Jianfu Ding. Veri fi cation of Icephobic/Anti-icing Properties of a Superhydrophobic Surface. 2013.

[38] D De Pauw and A Dolatabadi. Effect of Superhydrophobic Coating on the Anti-Icing and Deicing of an Airfoil. 54(2), 2017.

[39] Wolfgang M Sigmund and Shu-Hau Hsu. *Cassie–Baxter Model*, pages 310–311. Springer Berlin Heidelberg, Berlin, Heidelberg, 2016.

[40] Robert F Ide and D W Sheldon. 2006 Icing Cloud calibration of the NASA Glenn Icing Research Tunnel. *39th Aerospace Sciences Meeting & Exhibit*, (May):19, 2008.

[41] Technical Data Climate Wind Tunnel. Technical report, Rail Tec Arsenal - Large Climatic Wind Tunnel, Vienna.

[42] S. Chintamani and D. Belter. Design features and flow qualities of the Boeing research aerodynamic icing tunnel. *32nd Aerospace Sciences Meeting and Exhibit*, 1994.

[43] Edward Herman. Goodrich Icing Wind Tunnel Overview, Improvements and Capabilities. *44th AIAA Aerospace Sciences Meeting and Exhibit*, (January), 2006.

[44] K. Al-Khalil and L. Salamon. Development of the Cox Icing Research Facility. *36th Aerospace Sciences meeting and Exhibit*, (AIAA 98-0097), 1998.

[45] Eward Rocco. *Super-Cooled Large Droplet Experimental Reproduction, Ice Shape Modeling, and Scaling Law Assessment*. Masters, The Pennsylvania State University, 2017.

[46] William Olsen. Survey of Aircraft Icing Simulation Test Facilities in North America. Technical report, NASA Technical Memorandum, 1981.

[47] Stefan van 't Hoff, Jasper van der Vorst, Robert J. Flemming, and David Parkins. Icing Certification of Korean Utility Helicopter KUH-1: Artificial Icing Flight Test. *9th AIAA Atmospheric and Space Environments Conference*, (June):1–9, 2017.

[48] Craig Whitlock. When Drones Fall from the Sky, June 2014.

[49] Unmanned Aerial vehicle Reliability Study. Technical report, Department of Defense, 2003.

[50] Jeremiah Gertler. U.S. Unmanned Aerial Systems. Technical report, Congressional Research Service, 2012.

[51] Baofeng Cheng, Yiqiang Han, Kenneth S Brentner, Jose Palacios, Philip J Morris, David Hanson, and Michael Kinzel. Surface roughness effect on rotor broadband noise. *International Journal of Aeroacoustics*, 17(4-5):438–466, 2018.

[52] Stainless Steel Grade Datasheets. Technical report, Atlas Steels Technical Department, 2013.

[53] Tom Irvine. Damping Properties of Materials Revision C. Technical report, 2004.

[54] Erland Schulson and Paul Duval. Creep and Failure of Ice. Technical report, Cambridge University Press, 2009.

[55] Simulia. Abaqus Theory Guide, 2014.

[56] E J Barbero. *Finite Element Analysis of Composite Materials using Abaqus*. CRC Press/Taylor & Francis Group, Boca Raton, FL, 2013.

[57] Stresses: Beams in Bending. Technical report, Massachusetts Institue of Technology, 2018.

[58] A Turon. An Engineering Solution for solving Mesh Size Effects in the Simulation of Delamination with Cohesive Zone Models. *Elsevier Science*, 2005.

[59] Yanfei Gao and Allan Bower. A simple technique for avoiding convergence problems in finite element simulations of crack nucleation and. *Modelling and Simulation in Materials Science and Engineering*, 12(453-463), 2004.

[60] Majid Shahzad, Ali Kamran, Muhammad Zeeshan Siddiqui, Muhammad Farhan, Advance Materials, and Islamabad Highway. Mechanical Characterization and FE Modelling of a Hyperelastic Material. 18(5):918–924, 2015.

[61] Taylor D Knuth. *Ice Adhesion Strength Modeling Based on Surface Morphology Variations*. PhD thesis, The Pennsylvania State University, 2015.